

SYNTHESIS AND PROPERTIES OF COMPLEXES FEATURING IMIDAZOLE-N OR
PYRROLE-N DONORS: (I) NON-HEME IRON COMPLEXES WITH IRON-IMIDAZOLE
BONDS (II) COBALT-NITROSYLS WITH COBALT-PYRROLIDE BONDS.

by

KOUSTUBH SHISHIR DUBE

(Under the Direction of Todd C. Harrop)

ABSTRACT

Iron-imidazole ligation is ubiquitous in non-heme enzymes especially those involved in oxidative stress response. In chapter 1, we have demonstrated that N4 ligands with these donors are not straightforward in regards to coordination chemistry and afford eight-coordinate systems depending on geometrical constraints imposed by the ligand. These molecules are structurally robust and, like biological non-heme Fe-Im systems, exhibit reversible electrochemistry. Synthetic modifications rendered these systems to coordinate in the expected fashion and have allowed us to construct a variety of Fe(II)-N4-L systems that replicate structural and spectroscopic features of metalloenzymes such as superoxide reductase (SOR).

The coordination chemistry of nitric oxide (NO) is very rich and much of its chemistry is related to metal coordination. In chapter 2, we report the synthesis/characterization of {CoNO}⁸ and {CoNO}⁹ systems. The structure, spectroscopy, and reactivity of these CoNO compounds demonstrate that they could be useful in NO or HNO delivery.

INDEX WORDS: iron, cobalt, imidazole, pyrrole, nitrosyls, nitric oxide, superoxide, high coordination number, NO-transfer, synthetic models

SYNTHESIS AND PROPERTIES OF COMPLEXES FEATURING IMIDAZOLE-N OR
PYRROLE-N DONORS: (I) NON-HEME IRON COMPLEXES WITH IRON-IMIDAZOLE
BONDS (II) COBALT-NITROSYLS WITH COBALT-PYRROLIDE BONDS.

by

KOUSTUBH SHISHIR DUBE

B.Sc., University of Pune, India, 2007

A Thesis Submitted to the Graduate Faculty of The University of Georgia in Partial Fulfillment
of the Requirements for the Degree

MASTER OF SCIENCE

ATHENS, GEORGIA

2011

© 2011

Koustubh Shishir Dube

All Rights Reserved

SYNTHESIS AND PROPERTIES OF COMPLEXES FEATURING IMIDAZOLE-N OR
PYRROLE-N DONORS: (I) NON-HEME IRON COMPLEXES WITH IRON-IMIDAZOLE
BONDS (II) COBALT-NITROSYLS WITH COBALT-PYRROLIDE BONDS.

by

KOUSTUBH SHISHIR DUBE

Major Professor: Todd C. Harrop

Committee: Michael K. Johnson
Robert. A. Scott

Electronic Version Approved:

Maureen Grasso
Dean of the Graduate School
The University of Georgia
August 2011

ACKNOWLEDGEMENTS

I owe my deepest gratitude to the Department of Chemistry at The University of Georgia for providing me with a platform to further my academic career and experience. I would like to thank Dr. Todd Harrop for his expert advice academically and personally, without which this body of work would not have been possible. I would also like to thank my lab colleagues, Dr. Ashis Patra, Eric, Vivian, Wren and Brian for their support during my stay at UGA. I thank Dr. Johnson for his support and his lab group for help with EPR measurements. I would also like to appreciate Dr. Wylie, Dr. Phillips and Dr. Wei for their help with NMR, Mass-Spec and X-ray crystallography respectively. I am thankful to Dr. Evert Duin for help with simulating the EPR spectrum of $\{\text{CoNO}\}^9$ complexes. Lastly I am grateful for all the support from my friends and family.

TABLE OF CONTENTS

	Page
ACKNOWLEDGEMENTS.....	iv
LIST OF TABLES	vi
LIST OF FIGURES	vii
CHAPTER	
1 Iron(II) Imidazole Complexes: Structure and Reactivity.....	1
1.1 Introduction.....	1
1.2 Results and Discussion	5
1.3 Reactivity	17
1.4 Conclusions.....	23
1.5 Experimental Details	24
References	33
2 Cobalt Nitrosyl Complexes: Structure and Reactivity.....	36
2.1 Introduction and Intent of Research.....	36
2.2 Results and Discussion	42
2.3 Conclusion	59
2.4 Experimental Details	60
References	70

APPENDIX

A	Structure and Properties of an eight-coordinate Mn(II) complex that demonstrates a high water relaxivity	73
---	--	----

LIST OF TABLES

	Page
Table 1.1: Selected amino acid residues that occur as ligands in metalloproteins	2
Table 1.2: Selected bond distances (Å) and bond angles (deg) of 1	7
Table 1.3: Selected bond distances (Å) and bond angles (deg) of 2	9
Table 1.4: Selected bond distances (Å) and bond angles (deg) of 4	13
Table 1.5: Selected bond distances (Å) and bond angles (deg) of 5	16
Table 1.6: X-ray parameters for 4 and 5	32
Table 2.1: Selected structural parameters of {CoNO} ⁸ complexes from figure 2.3	41
Table 2.2: Selected bond distances (Å) and bond angles (deg) of 1	46
Table 2.3: Selected bond distances (Å) and bond angles (deg) of 2	48
Table 2.4: X-ray parameters for 1 and 5	69
Table 3.1: Summary of crystal data and intensity collection and structure refinement parameters for [Mn(L _{N4}) ₂](ClO ₄) ₂ •MeCN (1 •MeCN)	94
Table 3.2: Selected bond distances (Å) and bond angles (deg) for [Mn(L _{N4}) ₂](ClO ₄) ₂ •MeCN (1 •MeCN)	95

LIST OF FIGURES

	Page
Figure 1.1: The active site of Fe(II)-SOR (left) and the proposed catalytic cycle (right).....	4
Figure 1.2: ORTEP view of $[\text{Fe}(\text{L}_{\text{N4}})(\text{MeCN})_2](\text{BF}_4)_2$ (1) showing 30% probability thermal ellipsoids for all non hydrogen atoms.....	7
Figure 1.3: ORTEP view of (2 •DMF) showing 30% probability thermal ellipsoids for all non hydrogen atoms.	8
Figure 1.4: Mössbauer spectrum of $[\text{Fe}(\text{L}_{\text{N4}})_2](\text{BF}_4)_2$ (2).....	10
Figure 1.5: ORTEP view of all non hydrogen atoms of the cationic portion 4 at 30% thermal ellipsoid probability.	13
Figure 1.6: UV-vis spectrum of 4 in MeCN at 298 K, inset: cyclic voltammogram of 4	14
Figure 1.7: ORTEP view of the cation of $[\text{Fe}(\text{LN}_4^{\text{Pr}})(\text{DMAP})_2](\text{BF}_4)_2$ (5) at 30% probability for all non hydrogen atoms.....	16
Figure 1.8: Solid-state FTIR spectrum of 6 , inset: CV of 6 (2 mM) in MeCN	19
Figure 1.9: ESI-MS of 6	19
Figure 1.10: UV-vis spectrum of 6 in MeCN at 298 K (black trace) and immediately upon exposure to air (red trace); inset: UV-vis spectral decay of the oxidized species monitored over 6 h at 5 min intervals.....	20
Figure 1.11: UV-vis spectra of 4 + H_2O_2 •urea (1.5 mol-equiv) recorded for 4.5 min at 9 s intervals in MeOH at 195 K.....	22

Figure 1.12: UV-vis spectra of 4 + <i>m</i> CPBA (0.5 equiv) recorded for 7.5 min at 15 s intervals in MeCN at 238 K.	23
Figure 1.13: FTIR of LN_4^{Pr} (solid, ATR-diamond).....	26
Figure 1.14: ^1H NMR of ligand LN_4^{Pr} in CDCl_3 (0.05% v/v TMS) at 298 K	27
Figure 1.15: FTIR spectrum of complex 4 (KBr Matrix).....	28
Figure 1.16: FTIR spectrum of 5 (solid, ATR-diamond).....	29
Figure 1.17: UV-vis spectrum of 5 in MeCN at 298 K in the presence of excess DMAP.	29
Figure 2.1: MO diagram for the valence shell of NO	38
Figure 2.2: $\{\text{CoNO}\}^8$ complexes, $[\text{Co}(\text{LN}_4^{\text{Pr}})(\text{NO})]$ (1) (left) and $[\text{Co}(\text{LN}_4^{\text{Ph}})(\text{NO})]$ (2) (right), utilized in this work	40
Figure 2.3: Selected examples of structurally characterized $\{\text{CoNO}\}^8$ cobalt nitrosyls	41
Figure 2.4: ORTEP diagram of 1 at 30% thermal ellipsoids (left, side-view; right, top-view)	45
Figure 2.5: ORTEP diagrams of two independent molecules of 2 in the asymmetric unit (top-view looking above Co-N-O vector) at 30% thermal ellipsoids showing the two perspectives of the Co-NO vector	47
Figure 2.6: ORTEP diagram of 2 (side-view) at 30% thermal ellipsoids	47
Figure 2.7: FTIR spectrum of $[\text{Co}(\text{LN}_4^{\text{Pr}})(\text{NO})]$ (1) in a KBr matrix. Inset: NO stretching frequency region comparing 1 (red trace) and 1 - ^{15}NO (black trace)	50
Figure 2.8: FTIR spectrum of $[\text{Co}(\text{LN}_4^{\text{Ph}})(\text{NO})]$ (2) in a KBr matrix. Inset: NO stretching frequency region comparing 2 (red trace) and 2 - ^{15}NO (black trace)	50
Figure 2.9: ^1H NMR spectrum of 1 in $\text{THF-}d_8$ at 298 K.....	51
Figure 2.10: ^1H NMR spectrum of 2 in $\text{THF-}d_8$ at 298 K.....	52

Figure 2.11: ^{15}N NMR spectrum of (1 - ^{15}NO) in THF- d_8 at 298 K (CH_3NO_2 used as external standard).....	52
Figure 2.12: CVs and DPV of 2 mM MeCN solutions of 1 (top) and 2 (bottom).....	54
Figure 2.13: FTIR spectra of (1 ^{red}) (left) and (2 ^{red}) (right) in a KBr matrix.....	56
Figure 2.14: X-band EPR spectrum of 1 ^{red} (left) and 2 ^{red} (right) in MeCN/Toluene (1:1) at 20 K	57
Figure 2.15: Simulation (red trace) of the X-band EPR spectrum of 2 ^{red} (black trace).....	57
Figure 2.16: UV-vis spectral monitoring of the reaction of a 5 μM THF solution of $[\text{Fe}(\text{TPP})\text{Cl}]$ with 1 ^{red} (1:1.2) in THF at 298 K.....	59
Figure 2.17: FTIR spectrum of $(\text{LN}_4^{\text{pr}})$ (ATR-diamond, solid).....	61
Figure 2.18: ^1H NMR spectrum of LN_4^{pr} in CDCl_3 (0.05% v/v TMS) at 298 K.....	61
Figure 2.19: FTIR spectrum of LN_4^{ph} (ATR-diamond, solid)	62
Figure 2.20: ^1H NMR spectrum of LN_4^{ph} in CDCl_3 (0.05% v/v TMS) at 298 K	63
Figure 2.21: UV-vis spectrum of a 66.0 μM solution of 1 in MeCN at 298 K	65
Figure 2.22: UV-vis spectrum of a 42 μM solution of 2 in MeCN at 298 K	67
Figure 3.1: ORTEP view of the cation of 1	77
Figure 3.2: UV-vis spectral monitoring of 1 (0.013 mM) in PIPES buffer (pH 7.3) under aerobic conditions at 298 K.....	80
Figure 3.3: UV-vis spectral monitoring of complex 1 (0.013 mM) in phosphate buffer (pH = 7.27) at 298 K.....	88
Figure 3.4: UV-vis spectral monitoring of complex 1 (0.013 mM) in PIPES buffer (pH = 7.31) at 298 K	89

Figure 3.5: UV-vis spectral monitoring of complex 1 (0.013 mM) in CHES buffer (pH = 9.04) at 298 K	90
Figure 3.6: UV-vis spectral monitoring of complex 1 (0.013 mM) in MES buffer (pH = 6.24) at 298 K	91
Figure 3.7: ORTEP diagram of (1 •MeCN) at 50% thermal probability	96
Figure 3.8: (Left) A simplified view showing the coordination trapezoids (as defined by Lippard) ⁹ of the coordination sphere around Mn(II) in 1 ; (Right) The two intersecting planes of the L _{N4} ligand in 1 ; angle made by the two planes is 87.09°.	96
Figure 3.9: X-band EPR spectrum of [Mn(L _{N4}) ₂](ClO ₄) ₂ (1) in a 1:1 MeCN:toluene glass.....	98
Figure 3.10: Low-resolution ESI-MS of a 0.133 mM solution of [Mn(L _{N4}) ₂](ClO ₄) ₂ (1) in positive ion mode in pH 7.28 PIPES buffer.....	99
Figure 3.11: (Top) Low-resolution ESI-MS(+) of the CH ₂ Cl ₂ extract from a 0.133 mM solution of (1) in pH 7.28 PIPES buffer after 2 h. (Bottom) qualitative UV-vis spectrum of the CH ₂ Cl ₂ extract in MeCN at 298 K, which resembles the UV-vis of 1	100
Figure 3.12: Cyclic voltammogram of a 2.70 mM MeCN solution of [Mn(L _{N4}) ₂](ClO ₄) ₂ (1) ...	101
Figure 3.13: Representative plots for calculation of T1 relaxivity measurements for one sample run.....	102
Figure 3.14: Data and workup of one representative experiment to obtain the relaxivity (<i>R</i> ₁) value for complex 1 (CD ₃ OD/H ₂ O (5:1), 60 MHz, 298 K).	103

CHAPTER 1

IRON (II) IMIDAZOLE COMPLEXES: STRUCTURE AND REACTIVITY

1.1 Introduction



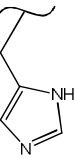
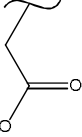
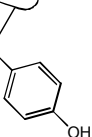

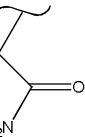
Bioinorganic chemistry can be loosely defined as the study of metal containing proteins (metalloproteins) and their analogs. Such proteins can be classified according to their function or the type of metal they incorporate. It has been predicted that over 50% of all proteins could be classified under the broad class of metalloproteins.¹ Metalloproteins are not just at the core of the metabolism of living beings, but also contribute in shaping up the atmosphere by recycling of elements during the biogeochemical cycles. For example, elements such as carbon and nitrogen undergo a variety of oxidation and reduction processes with the help of metalloproteins in their geochemical transformations.²

Most metalloproteins contain first row transition metals such as Fe, Co, Ni, Mn, Cu and Zn.² Proteins utilize specific amino acid residues in order to bind to the metal (Table 1.1). The binding of specific residues to the metal center, provides specific tuning mechanisms of the structural and/or redox properties of the metal center in the metalloprotein. One such amino acid residue that is essential in binding metals in a variety of metalloenzymes is Histidine (His).

His is able to bind to metals through the imidazole N ϵ or N δ , the overall pK_a values for His is 6.0.² For example, His is ligated to Cu in multicopper oxidases, which brings about the four electron reduction of dioxygen to form water.³ His-bound metals can also act as ligands in redox-inactive metalloproteins where the metal center serves a structural or hydrolytic role as the Zn(II) ion in the zinc finger motifs, which are commonly bound by two His and two Cys residues.⁴

The overall goal of this research is to synthesize small-molecule analogs of the active center of the enzyme superoxide reductase (SOR). SOR is a non-heme iron enzyme, which contains an active Fe(II) ion coordinated by four histidines and a cysteine in its active site (*vide infra*).⁵

Table 1.1. Selected amino acid residues that occur as ligands in metalloproteins.

Amino Acid	Residue Structure	Role in Metalloproteins*
Cys		Cysteine often coordinates through thiolate sulfur. Involved in coordination with Cu, Zn, Fe and Ni. For example, iron-sulfur proteins.
Met		Methionine can coordinate through neutral thioether sulfur. Involved in coordination with Cu in blue copper proteins, which serve as electron transfer agents.
His		Histidine can ligate through its Nδ1 or Nε2 nitrogens (or both). His ligation is found in proteins with Fe, Cu, Ni and Zinc active sites. For example, Cu-Zn superoxide dismutase (SOD).
Asp		Aspartate can bind to metals in a monodentate fashion through its terminal carboxylate oxygen or act as a bidentate ligand. For example, Asp is bound to Fe (III) in ferritin.
Tyr		Tyrosine binds through its deprotonated form to metals such as Fe(III) e.g. purple acid phosphatases.
Ser		Serine binds through its hydroxyl group. Serine is ligated to K ⁺ in dialkyl decarboxylase.
Asn		Asparagine binds through its carbonyl oxygen to metals such as Mn(II) in phosphatase.

*see reference 2 for a detailed discussion on metal ligating amino acid residues.

Superoxide and role of superoxide reductase (SOR):

Superoxide is the one-electron reduced radical anion species ($O_2^{\cdot-}$) of molecular oxygen that is produced as a byproduct of aerobic respiration.⁶ Superoxide has a bond distance of 1.28 Å⁷, which lies between the double bond in O_2 (1.21 Å) and the single bond in peroxide (1.49 Å).⁸

The reduction potential of O_2 is -0.16 V (pH 7, vs. NHE).⁷ Reactive oxygen species (ROS), such as superoxide, are produced during the routine metabolic activities of the body such as respiration.^{9,10,11} One such source of $O_2^{\bullet-}$ is the mitochondrial electron transport chain. The $O_2^{\bullet-}$ thus produced can lead to radical reaction pathways that ultimately are harmful to the organism.¹² Free radicals such as $O_2^{\bullet-}$ react with proteins, lipids, and nucleic acids in the cell. These interactions can cause a structural defect in the bio-substrates that eventually leads to their inactivity, which in some cases cause cell death.¹³ An increase in oxidative stress has also been related to the development of diabetes; neurodegenerative diseases such as Parkinson's and Alzheimer's are also linked by cell degeneration due to oxidative damage.¹⁴ Thus, there is a necessity to develop synthetic molecules that interact with radicals such as $O_2^{\bullet-}$ to gain insights into its chemical degradation. This knowledge then can be utilized to gain a fundamental understanding of and requirements for converting $O_2^{\bullet-}$ into non-harmful by-products. Indeed, the interaction of $O_2^{\bullet-}$ with a variety of inorganic and organic molecules has been reported. For example, $O_2^{\bullet-}$ acts as a one-electron reductant to transition-metal complexes such as Fe(III)(TPP)Cl and Mn(III)EDTA.^{15,16} Additionally, interactions of $O_2^{\bullet-}$ with substrates that have readily transferable H-atoms such as dihydrophenazines, reduced flavins, hydrazines and hydroxyl amine have been known.⁶

Superoxide dismutase (SOD) is one such enzyme that destroys $O_2^{\bullet-}$ in aerobic organisms^{17,18} via a disproportionation reaction where the end products are $O_2(g)$ and H_2O_2 . Since this mechanism would lead to production of O_2 , it is not an ideal regulatory path for anaerobes and micro-aerophiles that occasionally encounter oxidative stress. In order to avoid oxidative stress, these organisms employ enzymes known as superoxide reductases (SOR) that reduce superoxide to hydrogen peroxide (Eq. 1), basically half of the SOD-catalyzed reaction.¹⁹



The active site of SOR consists of a square-pyramidal Fe(II) center coordinated by the nitrogen of four equatorial histidine residues and one axially bound cysteinate residue trans to the vacant (substrate accessible) site. In the oxidized form of the enzyme, the Fe(III) center is six-coordinate via ligation of a glutamate-O ligand at the open axial site trans to the cysteinate moiety.²⁰ The glutamate residue shifts a distance of 7.1 Å upon the reduction of Fe(III) to Fe(II) and is presumably present to avoid any oxygen-related chemistry with the Fe(III) enzyme. The presence of a lysine residue near the active site (6 to 12 Å) is proposed to help direct the superoxide anion to the active site via coulombic forces.

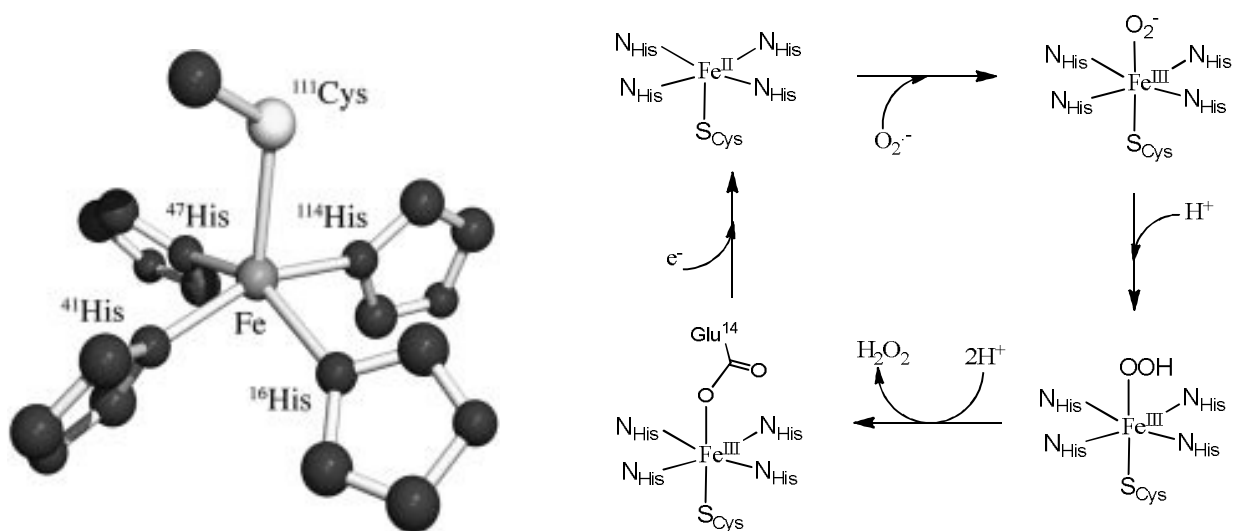


Figure 1.1. The active site of Fe(II)-SOR²¹ (left) and the proposed catalytic cycle (right).

Superoxide reacts with the reduced Fe(II) state of SOR via a proposed inner-sphere mechanism. In the first step, O₂^{•-} binds to the open site, trans to the cysteinate residue generating an Fe(III)-OOH intermediate via one-electron reduction from the Fe(II) center (Figure 1.1). Support for this inner-sphere mechanism has come from the binding of other small anionic molecules such as N₃⁻, NO, and CN⁻.²² The high-spin Fe(III)-OOH intermediate has been characterized by UV-vis where it displays a transition in the visible region at ~600 nm (~3500

$\text{M}^{-1} \text{cm}^{-1}$) assigned as peroxo-to-Fe(III).²³ Then through a protonation step (source of which is still debated), H_2O_2 is formed and released from the Fe(III) center. After the release of H_2O_2 , the Fe(III) center is coordinated by glutamate, which is proposed to protect the Fe center from being attacked by another superoxide molecule and potential $\text{O}_2(\text{g})$ formation.

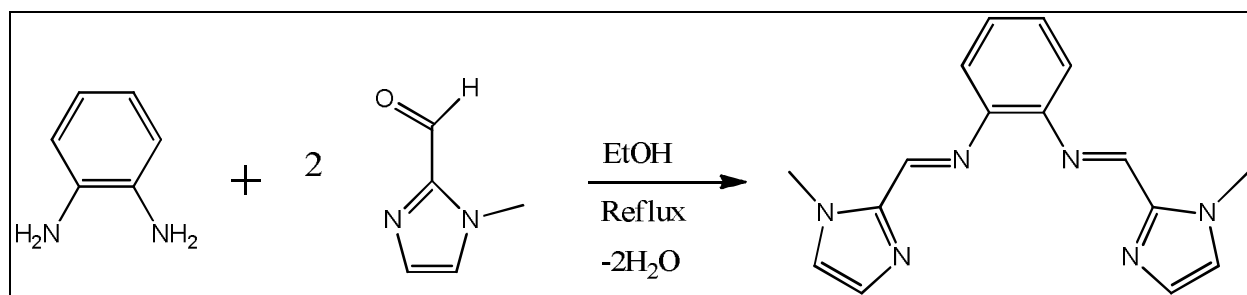
It is the goal of this research to synthesize appropriate ligand constructs that could support Fe(II/III) as potential small-molecule synthetic analogues of SOR. To accomplish this goal the synthesis of a series of planar N_4 ligand containing imidazole-type and neutral N-donors is required. For this purpose, we have designed and synthesized a series of non-macrocyclic yet rigid and planar ligand frames incorporating imidazole- and imine-N donors as primary coordination sphere mimics of the basal plane coordination exhibited in SOR. The synthesis, spectroscopic/redox properties, and reactivity of these ligands and their corresponding Fe(II) complexes are discussed in this chapter.

1.2 Results and Discussion:

1.2.1 First generation N_4 Ligands ($\text{L}_{\text{N}4}$)

To model the N_4 planar coordination sphere, we synthesized a Schiff base (imine functionality) ligand with a phenylene linker by following the synthetic route described in Scheme 1.1. The synthesis was one step and is high yielding (~80 %). The desired ligand was analyzed by ^1H and ^{13}C NMR, FTIR, and LRMS-ESI. The corresponding Fe complexes $[\text{Fe}(\text{L}_{\text{N}4})(\text{MeCN})_2](\text{BF}_4)_2$ (**1**) and $[\text{Fe}(\text{L}_{\text{N}4})_2](\text{BF}_4)_2$ (**2**) (eight coordinate = 8C) were synthesized by reacting the appropriate mole-equivalents of ligand (ligand-to-Fe ration was 1:1 for **1** and 1:2 for **2**) with $[\text{Fe}(\text{H}_2\text{O})_6](\text{BF}_4)_2$. It was our plan to utilize the FeN_4 complexes such as **1** to form FeN_4SR complexes as SOR models; the isolation of 8C **2** was unexpected. Additionally, in the

case of reacting 1:1 ligand-to-Fe, it was observed by ESI-MS that the reaction consisted of a mixture of both **1** and **2**.



Scheme 1.1. Synthetic route of the N₄ Schiff-base ligand L_{N4}.

The X-ray structure of complex **1** clearly indicated that L_{N4} was binding in a planar fashion to the Fe(II) center with two vacant sites trans to each other (Figure 1.2). These axial sites are occupied by two coordinated MeCN solvent molecules. The bite angle comprised of the two imine-N donors of L_{N4} is calculated to be ~40°. Given the ionic radius of Fe(II) (0.92 Å) and the bite angle of the ligand it was later determined that this ligand was predisposed to form 8C complexes when bound to Fe(II).²⁴ Even though we were able to crystallize the mono-ligand species **1**, the ESI-MS showed a mixture of 1:1 and 1:2, metal-to-ligand species present. It was also observed that introducing anionic ligands such as Cl⁻ or N₃⁻ shifted the equilibrium of the mono-ligated to bis-ligated complex species through a yet undefined mechanism, indicating that 8C complex **2** is thermodynamically stable.

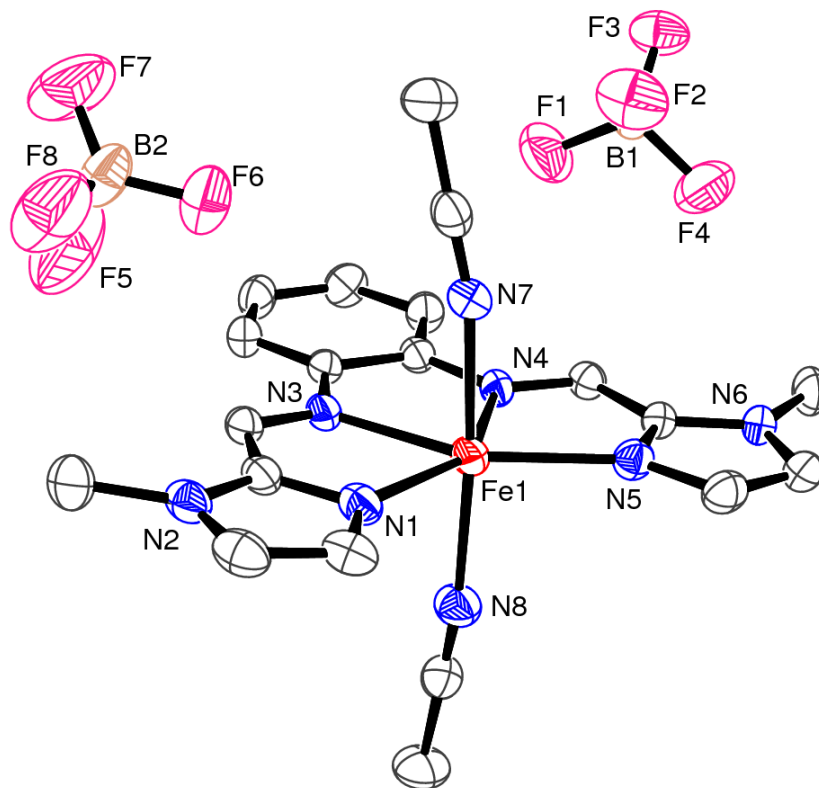


Figure 1.2. ORTEP view of $[\text{Fe}(\text{L}_{\text{N}4})(\text{MeCN})_2](\text{BF}_4)_2$ (**1**) showing 30% probability thermal ellipsoids for all non hydrogen atoms.

Table 1.2. Selected bond distances (Å) and bond angles (deg) of **1**.

Fe1-N1	1.998(2)	N3-Fe1-N5	176.43(9)
Fe1-N3	1.968(2)	N3-Fe1-N4	95.27(10)
Fe1-N4	1.967(2)	N3-Fe1-N8	90.20(10)
Fe1-N5	1.992(2)	N3-Fe1-N7	88.73(10)
Fe1-N7	1.937(3)	N4-Fe1-N5	81.44(10)
Fe1-N8	1.948(2)	N4-Fe1-N7	89.56(10)
N1-Fe1-N3	81.63(10)	N4-Fe1-N8	91.25(10)
N1-Fe1-N4	176.88(10)	N5-Fe1-N7	89.87(10)
N1-Fe1-N5	101.68(9)	N5-Fe1-N8	91.24(10)
N1-Fe1-N7	90.66(10)	N7-Fe1-N8	178.71(10)
N1-Fe1-N8	88.48(10)		

The 8C Fe(II) complex $[\text{Fe}(\text{L}_{\text{N}4})_2](\text{BF}_4)_2$ (**2**) is stable in solution and does not break down in the presence of a variety of anions like Cl^- , NO_2^- , and SCN^- . This inherent stability is not seen in other 8C complexes such as $[\text{Fe}(\text{TPA})_2]^+$, which break down in donor solvents.²⁵ The rigidity

of the LN_4 ligand and the bite angle of the imine donor nitrogens coupled with the ideal ionic radius of the central metal ion contributes to the formation of these 8C i.e. size-matched binding.²⁶

The X-ray structure of **2** confirmed the 8C nature of the complex (Figure 1.3). The geometry around the Fe(II) center is a distorted dodecahedral as defined by Lippard.²⁷ The two planar N_4 ligands wrap around the Fe perpendicular to each other with an inter-planar angle of 88.5° . The average $\text{Fe-N}_{\text{imine}}$ bond lengths are $2.432(2) \text{ \AA}$, while the average $\text{Fe-N}_{\text{imidazole}}$ distances are $2.253(2) \text{ \AA}$. These distances are similar to other known 8C Fe complexes with neutral N donors such as found in the diaza-pyridinophane complex $[\text{Fe}(\text{L-N}_4\text{-H}_2)_2]^{2+}$ where the average Fe-N_{py} distance is 2.298 \AA and average $\text{Fe-N}_{\text{amine}}$ distance is 2.382 \AA .²⁸

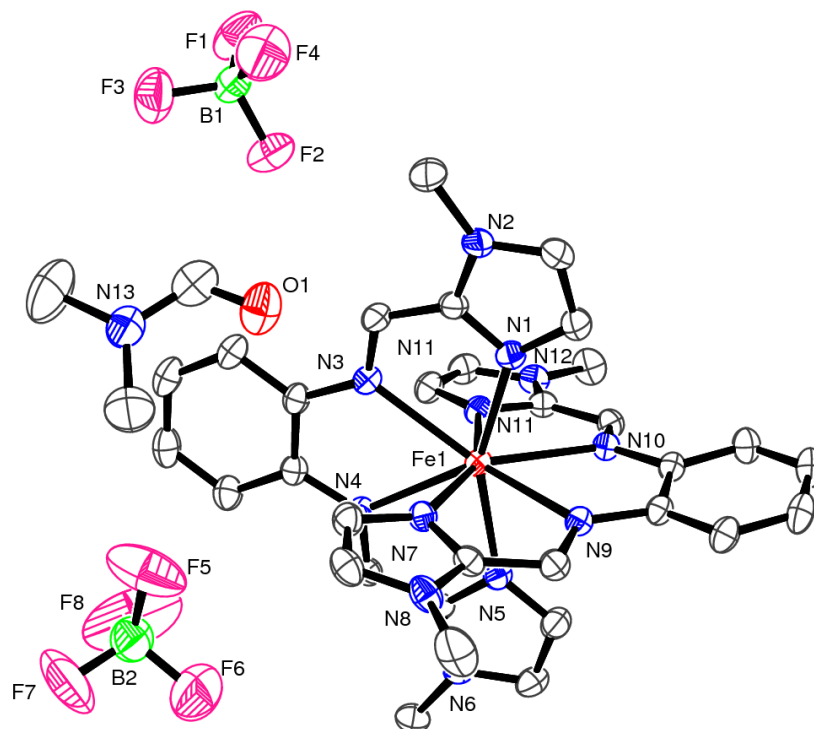


Figure 1.3. ORTEP view of (**2**•DMF) showing 30% probability thermal ellipsoids for all non hydrogen atoms.

Table 1.3. Selected bond distances (Å) and bond angles (deg) for **2**.

Fe(1)-N(1)	2.259(2)	N(3)-Fe(1)-N(9)	137.40 (8)
Fe(1)-N(3)	2.425(2)	N(3)-Fe(1)-N(10)	135.25(8)
Fe(1)-N(4)	2.456(2)	N(3)-Fe(1)-N(11)	80.52(8)
Fe(1)-N(5)	2.257(2)	N(4)-Fe(1)-N(5)	69.40(8)
Fe(1)-N(7)	2.250(2)	N(4)-Fe(1)-N(7)	79.87(8)
Fe(1)-N(9)	2.449(2)	N(4)-Fe(1)-N(9)	133.10(8)
Fe(1)-N(10)	2.400(2)	N(4)-Fe(1)-N(10)	136.22(8)
Fe(1)-N(11)	2.246(2)	N(4)-Fe(1)-N(11)	78.15(8)
N(1)-Fe(1)-N(3)	70.04(8)	N(5)-Fe(1)-N(7)	93.69(9)
N(1)-Fe(1)-N(4)	134.44(8)	N(5)-Fe(1)-N(9)	78.12(8)
N(1)-Fe(1)-N(5)	156.07(9)	N(5)-Fe(1)-N(10)	80.13(8)
N(1)-Fe(1)-N(7)	89.71(9)	N(5)-Fe(1)-N(11)	89.17(9)
N(1)-Fe(1)-N(9)	81.00(8)	N(7)-Fe(1)-N(9)	69.22(8)
N(1)-Fe(1)-N(10)	80.55(8)	N(7)-Fe(1)-N(10)	134.17(8)
N(1)-Fe(1)-N(11)	97.57(9)	N(7)-Fe(1)-N(11)	155.23(9)
N(1)-Fe(1)-N(11)	97.57(9)	N(9)-Fe(1)-N(10)	65.05(8)
N(3)-Fe(1)-N(4)	64.49(8)	N(9)-Fe(1)-N(11)	135.23
N(3)-Fe(1)-N(5)	133.86(9)	N(10)-Fe(1)-N(11)	70.55(8)
N(3)-Fe(1)-N(7)	79.81(8)		

The UV-vis spectrum of **2** in MeCN at 298 K exhibits broad visible bands at ~550 and ~650 nm which are d-d in origin ($\epsilon < 1000 \text{ M}^{-1} \text{ cm}^{-1}$). Complex **2** was redox-active and exhibits its Fe(II/III) redox couple at -0.430 V in MeCN vs. Ag/AgCl.²⁴ This reversible CV was indicative that formation of the corresponding 8C Fe(III) complex could also be realized. Indeed, when complex **2** was oxidized with a strong oxidant like ceric ammonium nitrate (CAN), the Fe(III) complex $[\text{Fe}(\text{LN}_4)_2](\text{NO}_3)_3$ (**3**) was formed in good yield. Crystallographic analysis of **3** proved that the 8C is retained in the Fe(III) state. As expected, the Fe-L distances in **3** are shorter than in **2** with avg. $\text{Fe-N}_{\text{imine}} = 2.353(2) \text{ \AA}$ and $\text{Fe-N}_{\text{imidazole}} = 2.183(2) \text{ \AA}$.

Complex **2** was further characterized by Mössbauer spectroscopy (Figure 1.4). Complex **2** demonstrated a large quadrupole splitting (ΔE_Q) of 3.85(2) mm/s and isomer shift (δ) of 1.56(6) mm/s at 4.2 K.^{28,29} This result is consistent with a high-spin Fe(II) metal center. This fact is further corroborated by the solution magnetic susceptibility of $4.94 \mu_B$ in MeCN.

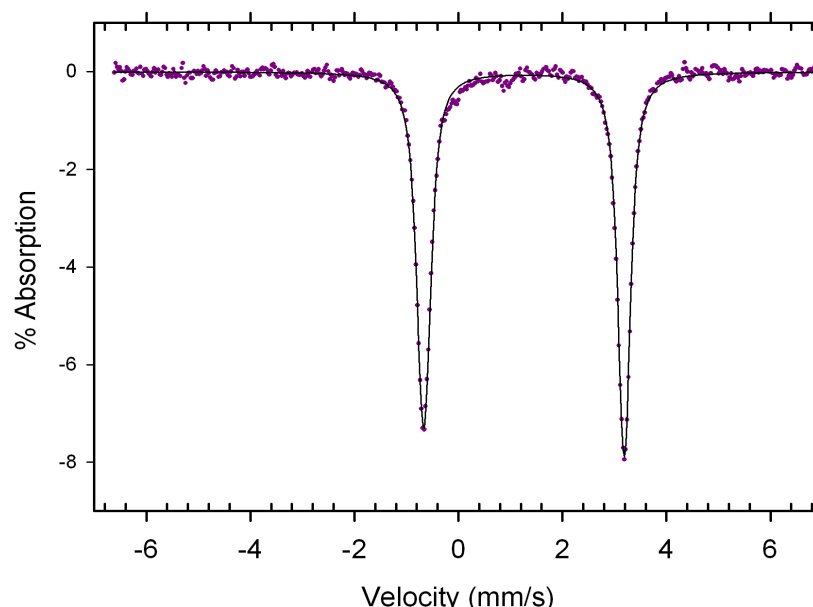


Figure 1.4. Mössbauer spectrum of $[\text{Fe}(\text{L}_{\text{N}4})_2](\text{BF}_4)_2$ (**2**). Data was collected on a powder sample at 4.2 K. The solid line shown is a least-square fit to the experimental data points of a simulated spectrum of 100% high-spin Fe(II) species with $\Delta E_{\text{Q}} = 3.85$ mm/s and $\delta = 1.56$ mm/s.

To gain more insight into the electronic structure of **2** DFT calculations were performed. Indeed, DFT calculations of **2** were able to reproduce the experimental structure with a high degree of accuracy.²⁰ The PW91/TZP functionals used for these calculations gave the best results while other functionals, such as OLYP and B3LYP, grossly overestimated the Fe-N distances. The high-spin nature of the complex was also reproduced by these calculations. The high-spin nature of the complex indicates that the five d-orbitals are of similar energy with comparable anti-bonding interactions with ligand lone pairs. The electronic configuration of the Fe(II) center in **2** may be described as $d_{xy}^2 d_{xz}^1 d_{yz}^1 d_{z^2}^1 d_{x^2-y^2}^1$, where lobes of d_{xy} point between the imidazole nitrogen atoms.

Thus, the development of ligand ($\text{L}_{\text{N}4}$) with the phenylene linker gave rise to unprecedented 8C complexes, which precludes their use as viable SOR models. The complexes

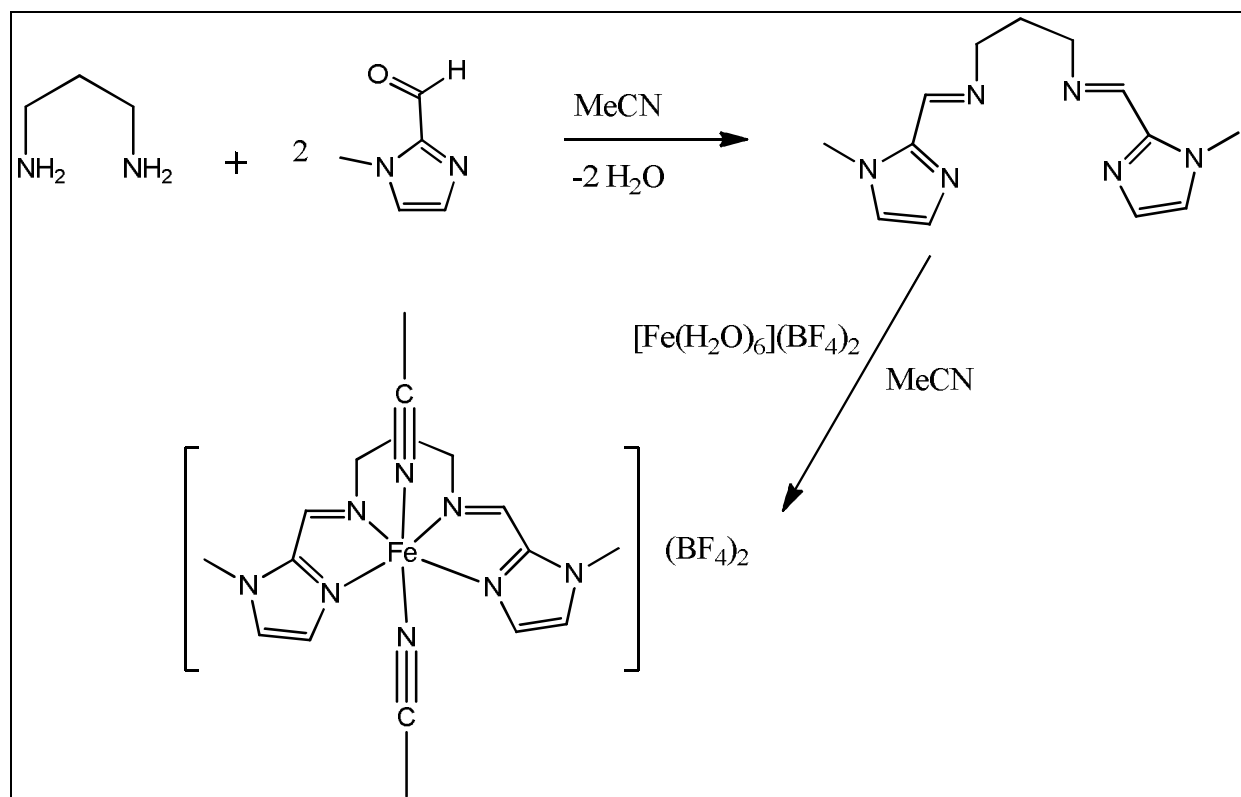
described above provide insight into the possibility of coordination chemistry with imidazole donors being part of higher coordinate complexes and corresponding redox activity.

1.2.2 Second Generation N4 Ligands (L_{N4}^{Pr})

After understanding that the ligand based on phenylene linker for the two imine-donors compels the Fe center into an 8C geometry, the next logical step was finding a donor set that would not induce such a geometry around the metal center. For this purpose, we introduced a propane linker in between the two imidazole-N donors to impart considerable flexibility in the ligand and in doing so inducing a smaller bite angle to chelate the central metal ion.

Synthesis and Spectroscopic Properties

The synthesis of this ligand was accomplished according to Scheme 1.2. The ligand is formed as a frothy residue in high yields (> 80%) and sufficiently characterized by 1H , ^{13}C NMR and FTIR. The Fe(II) complex with this ligand was synthesized by reacting the ligand with $[Fe(H_2O)_6](BF_4)_2$ anaerobically in a 1:1 ratio in MeCN to form the red crystalline complex, $[Fe(L_{N4}^{Pr})(MeCN)_2](BF_4)_2$ in high yield (80%) (Scheme 1.2).



Scheme 1.2. Synthesis of the Fe(II) complex $[\text{Fe}(\text{L}_{\text{N}4}^{\text{pr}})\text{MeCN}_2](\text{BF}_4)_2$ (**4**).

Complex **4** was crystallized by diffusion of Et_2O into MeCN at $-25\text{ }^\circ\text{C}$. X-ray crystallographic analysis of **4** clearly indicated that the ligand wraps around the Fe(II) center in a planar fashion (Figure 1.5). The geometry about the Fe(II) center in **4** is distorted octahedral with $\text{L}_{\text{N}4}^{\text{pr}}$ occupying the equatorial positions and two MeCN ligands in the axial sites. The Fe-N distances are short: $\text{Fe-N}_{\text{imine}}(\text{avg}) = 1.987(2)\text{ \AA}$; $\text{Fe-N}_{\text{imidazole}}(\text{avg}) = 1.995(2)\text{ \AA}$. These values are somewhat indicative of a low-spin Fe(II) center such as in $(\text{HBPz}_3)_2\text{Fe}$ where the average Fe(II)-N distances are $1.973(7)\text{ \AA}$.³⁰ However, this observation does not match with other magnetic and spectroscopic properties of **4** (*vide infra*).

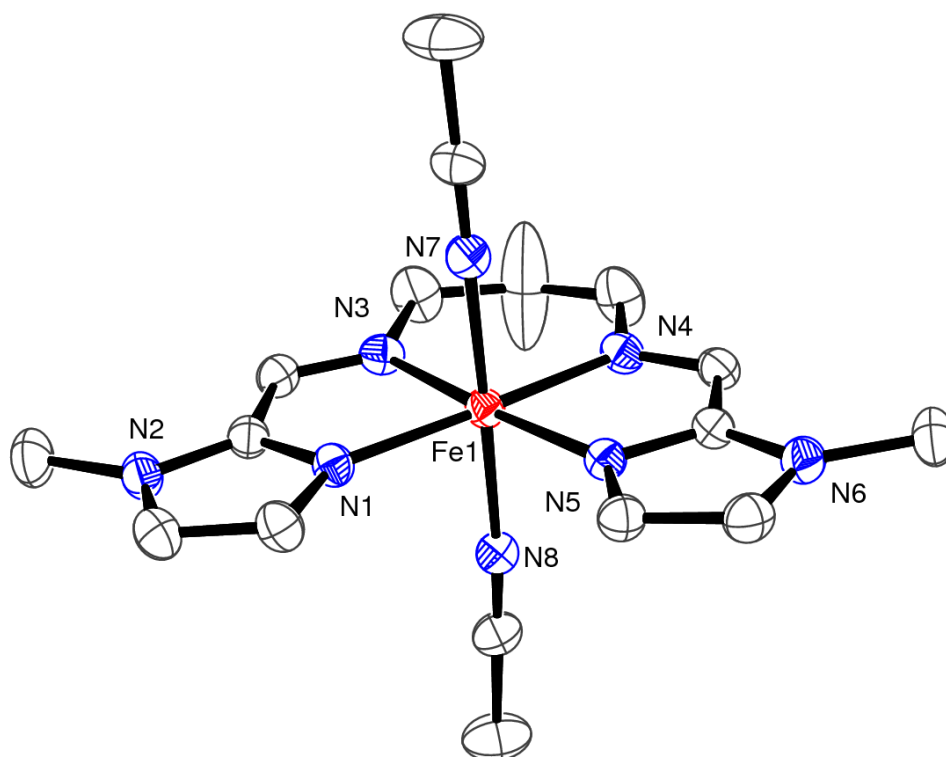


Figure 1.5. ORTEP view of all non hydrogen atoms of the cationic portion **4** at 30% thermal ellipsoid probability.

Table 1.4. Selected bond distances (Å) and angles (deg) for **4**.

Fe1- N1	1.998(2)	N3-Fe1-N5	176.43(9)
Fe1-N3	1.968(2)	N3-Fe1-N4	95.27(10)
Fe1-N4	1.967(2)	N3-Fe1-N8	90.20(10)
Fe1-N5	1.992(2)	N3-Fe1-N7	88.73(10)
Fe1-N7	1.937(3)	N4-Fe1-N5	81.44(10)
Fe1-N8	1.948(2)	N4-Fe1-N7	89.56(10)
N1-Fe1-N3	81.63(10)	N4-Fe1-N8	91.25(10)
N1-Fe1-N4	176.88(10)	N5-Fe1-N7	89.87(10)
N1-Fe1-N5	101.68(9)	N5-Fe1-N8	91.24(10)
N1-Fe1-N7	90.66(10)	N7-Fe1-N8	178.71(10)
N1-Fe1-N8	88.48(10)		

The FTIR spectrum of **4** shows an intense band at 1027 cm^{-1} present due to B-F stretching vibrations of the BF_4 counter-anion. Solid-state magnetic susceptibility measurements of **4** afforded a value of $4.08\ \mu_{\text{B}}$. This result shows that **4** is high-spin in the solid-state although

with unusually low Fe-L distances. To confirm that there is no temperature dependence on the spin-state of this complex, a variable temperature ^1H NMR study was done. In this experiment ^1H NMR spectra were recorded at increasing temperatures at 5 °C intervals from -40 °C to 25 °C. If complex **4** exhibits a spin-state temperature dependence, the low-spin d^6 system would be diamagnetic and thus be ^1H NMR active. The analysis of the spectra indicated that there was no change in the ^1H NMR profiles over this temperature range. This result proves that complex **4** is indeed paramagnetic (high-spin) at least till -40 °C.

The UV-vis spectrum of **4** in MeCN at 298 K displays absorption bands at 290 nm ($\epsilon = 19,300 \text{ M}^{-1} \text{ cm}^{-1}$), most probably due to MLCT transitions. Another band at 478 nm ($\epsilon = 5,000 \text{ M}^{-1} \text{ cm}^{-1}$) also arise from CT transitions (Figure 1.6). Electrochemical analysis of complex **4** in MeCN at RT shows quasi-reversible $E_{1/2}$ at 0.59 V with an irreversible reduction (E_{red}) peak at -1.72 V versus the ferrocene/ferrocenium (Fc/Fc^+) couple (Figure 1.6).

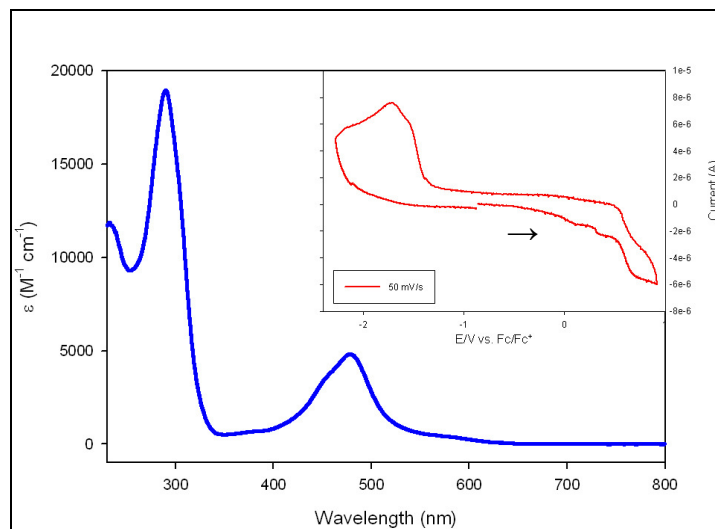


Figure 1.6. UV-vis spectrum of **4** in MeCN at 298 K, inset: cyclic voltammogram of **4** in MeCN (0.1 M $n\text{Bu}_4\text{NPF}_6$ supporting electrolyte, glassy carbon working electrode, Pt-wire counter electrode, RT).

To test the possibility of exchanging other axial ligands at the Fe(II) center in **4**, and ultimately realizing SOR-type complexes, we recorded the changes in the UV-vis spectrum of **4**

in MeCN in presence of excess (4 mol-equiv) of 4-dimethylaminopyridine (DMAP). Upon adding the excess DMAP to **4** the band at 478 nm blue-shifts to 610 nm indicating a change in the electronic nature of **4** and presumably formation of $[\text{Fe}(\text{L}_{\text{N4}}^{\text{Pr}})(\text{DMAP})_2](\text{BF}_4)_2$ (**5**). When this complex was isolated and introduced to donor solvents (in the absence of excess DMAP) such as MeCN, it was observed that the complex would loose the DMAP and the axial sites would be occupied by MeCN as indicated by the red-shift of the 610 nm band back to 478 nm consistent with formation of **4**. We were able to structurally characterize this complex by growing crystals by diffusing Et_2O into a MeCN solution of this complex at $-25\text{ }^\circ\text{C}$ in the presence of excess DMAP (Figure 1.7). The X-ray structure analysis proved our hypothesis that this complex is consistent with complex **5** where two DMAP ligands occupy the axial sites without little change in coordination of the $\text{L}_{\text{N4}}^{\text{Pr}}$ planar ligand. The metric parameters for this complex are similar to complex **4** and are depicted in Figure 1.7 and Table 1.5.

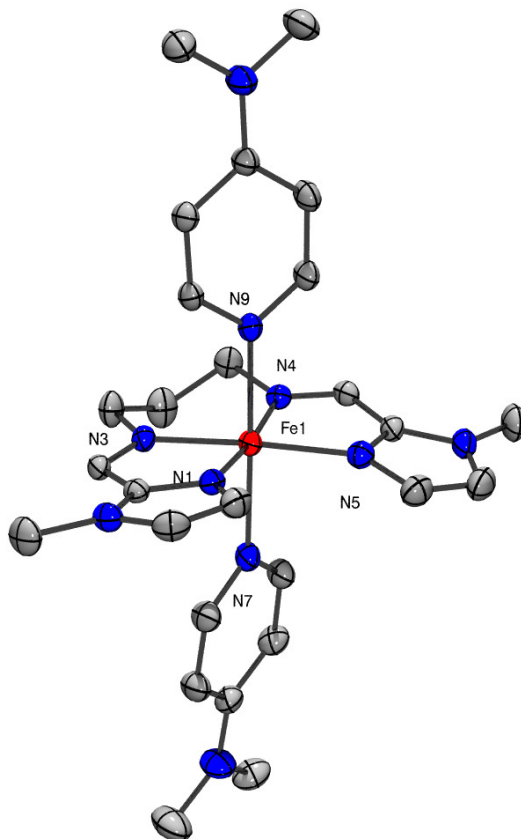


Figure 1.7. ORTEP view of the cation of $[\text{Fe}(\text{LN}_4^{\text{Pr}})(\text{DMAP})_2](\text{BF}_4)_2$ (**5**) at 30% probability for all non hydrogen atoms.

Table 1.5. Selected bond distances (Å) and angles (deg) for **5**.

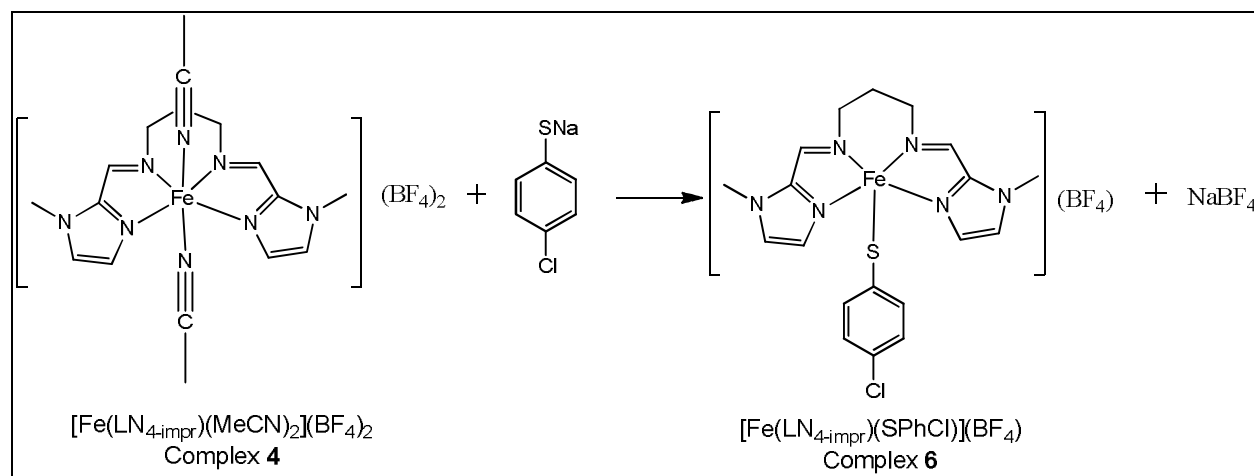
Fe1- N1	1.992(3)	N3-Fe1-N5	172.81(12)
Fe1-N3	1.971(3)	N3-Fe1-N4	95.16(12)
Fe1-N4	1.963(3)	N3-Fe1-N9	91.99(11)
Fe1-N5	2.003(3)	N3-Fe1-N7	86.80(12)
Fe1-N7	2.109(3)	N4-Fe1-N5	80.63(12)
Fe1-N9	2.087(3)	N4-Fe1-N7	93.21(12)
N1-Fe1-N3	81.07(12)	N4-Fe1-N9	87.37(11)
N1-Fe1-N4	173.66(11)	N5-Fe1-N7	87.62(12)
N1-Fe1-N5	103.63(12)	N5-Fe1-N9	93.62(12)
N1-Fe1-N7	91.67(12)	N7-Fe1-N9	178.70(11)
N1-Fe1-N9	87.67(11)		

1.3 Reactivity

The reactivity of **4** was explored to gain insight into the chemistry of molecules with Fe- $N_{\text{imidazole}}$ bonds in the primary coordination sphere especially in relation to SOR-type chemistry. The main focus of the reactivity studies was to explore the O_2 -activation and ROS-detoxification properties of **4** as this is one of the main functions that non-heme metalloenzymes perform in biology.

1.3.1 Reactivity with para-chlorobenzenethiolate

In efforts to synthesize an Fe(II)- N_4S complex as a structural and potentially functional analogue of SOR we reacted **4** with thiolate ligands (para-chlorobenzenethiolate was chosen for this study due to its stability in handling and MS marker). As stated earlier, the X-ray structure of **4** indicated that the non-macrocyclic ligand LN_4^{Pr} wrapped around the Fe(II) ion in a planar fashion (Figure 1.5). and is high-spin in nature. These are all properties consistent with the non-heme active Fe(II) in SOR. The synthesis was performed by reacting one equivalent of the sodium salt of para-chlorobenzenethiolate (formed by reacting the thiol with one-equiv of NaH in MeCN) with complex **4** in MeCN (Scheme 1.3) to form $[Fe(LN_4^{\text{Pr}})(S\text{-}p\text{-ClPh})]BF_4$ (**6**). The product is formed instantly as indicated by the color change of the reaction from red to maroon. Workup involved removing the formed $NaBF_4$ byproduct by dissolution in CH_2Cl_2 where **6** appears soluble and $NaBF_4$ is filtered off.



Scheme 1.3. Synthetic scheme for complex **6**.

The UV-vis spectrum of **6** in MeCN at 298 K shows multiple peaks centered around 370 nm ($\epsilon = 2,923 \text{ M}^{-1} \text{ cm}^{-1}$), 447 nm ($\epsilon = 2,083 \text{ M}^{-1} \text{ cm}^{-1}$) and 577 nm ($\epsilon = 1034 \text{ M}^{-1} \text{ cm}^{-1}$). These results are consistent with synthetic analogs of SOR, such as exogenous thiol-bound Fe(II) complexes of a pyridyl-appended diazacyclooctane ligand, reported by Halfen and coworkers.³¹ These complexes show overlapping transitions at 300 and 425 nm. Since these peaks are not seen in the precursor complex **4**, it is safe to assume some or all of these bands are some sort of manifestations of CT transitions involving the thiolate and Fe(II).

The FTIR spectrum of **6** matched well with the precursor, indicating that the ligand was indeed intact and a presumably part of the coordination sphere. Another significant peak was that from the BF_4^- counter-anion that showed its characteristic vibrational frequency at 1027 cm^{-1} . There were additional peaks from the exogenous thiolate at 814 cm^{-1} and 1486 cm^{-1} , which are attributed to the Aryl-Cl stretching vibrations (Figure 1.8). Electrochemical analysis of **6** in MeCN (0.1 M $^n\text{Bt}_4\text{NPF}_6$) yielded a irreversible reduction around -1.10 V along with a quasi reversible Fe(II/III) couple at 0.37 V (vs. Ag/AgCl). The reduction can be associated with irreversible reduction of ligand or a change in coordination sphere upon oxidation to the Fe(III) species. Perhaps the most convincing evidence for the formation of this complex comes from

ESI-MS. The MS clearly shows the formation of complex **6** with the expected isotopic distribution (Figure 1.9).

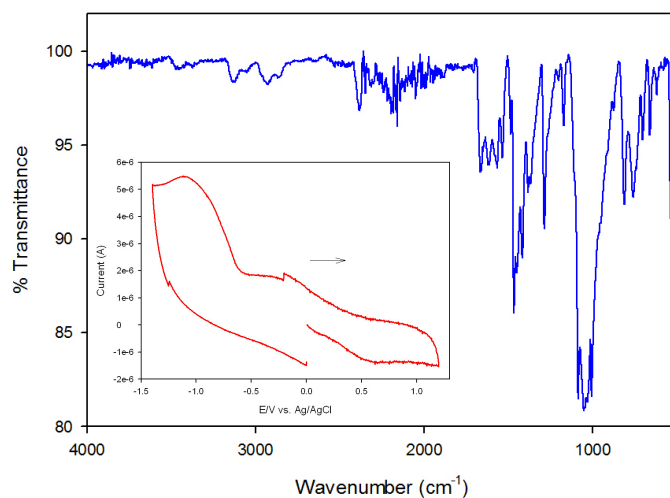


Figure 1.8. Solid-state FTIR spectrum of **6**, inset: CV of **6** (2 mM) in MeCN (0.1 M ⁿBu₄NPF₆ supporting electrolyte, glassy carbon working electrode, Pt-wire counter electrode, RT); arrow reveals direction of scan.

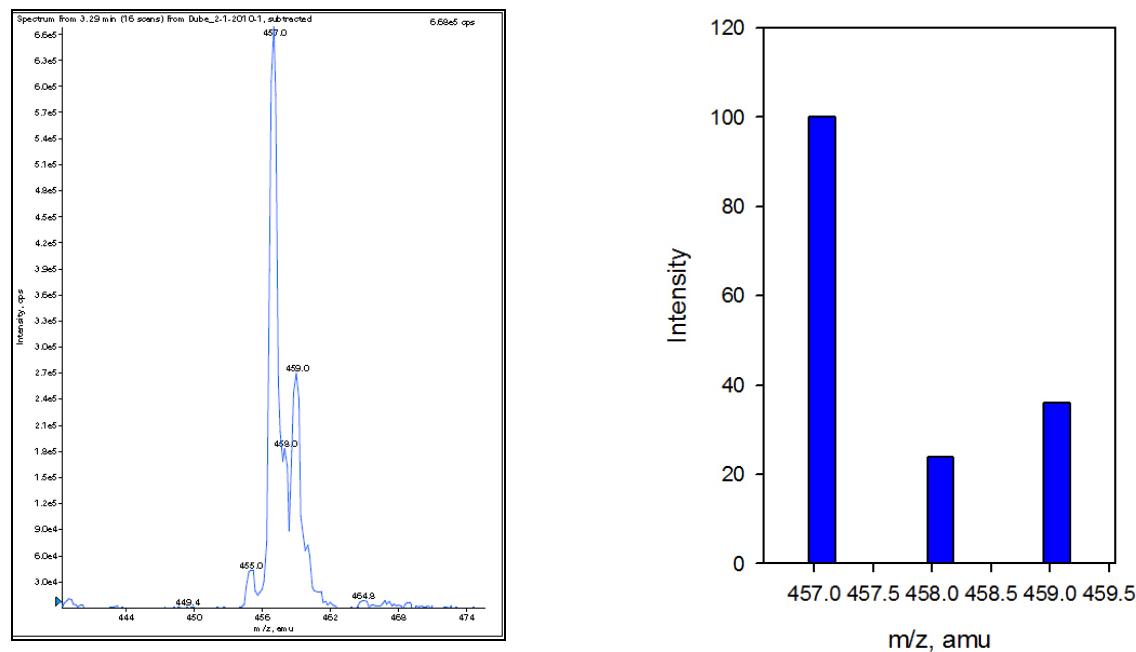


Figure 1.9. (left) ESI-MS of **6** showing peaks at $m/z = 457$ (100%), 458 (27.3%), 459 (40.2%); (right) expected ESI-MS distribution for [Fe(L_{N4}^{Pt})(S-*p*-ClPh)]⁺ $m/z = 457$ (100%), 458 (23.9 %), 459 (36.1 %).

Since complex **6** was well-poised for SOR-type chemistry, we wanted to explore its chemistry with dioxygen (O_2). The reaction of complex **6** when exposed to atmosphere was monitored by UV-vis at 298 K in MeCN. Upon exposure to air (or pure O_2), **6** rapidly reacts, as indicated by color change from maroon to dark green, to unidentified oxidized species. The UV-vis spectrum of this species shows a sudden rise in absorption at ~ 370 nm ($\epsilon = 9,944 \text{ M}^{-1} \text{ cm}^{-1}$), 441 nm ($\epsilon = 7,377 \text{ M}^{-1} \text{ cm}^{-1}$) (Figure 1.10). A visible band centered around 670 nm ($\epsilon = 1,538 \text{ M}^{-1} \text{ cm}^{-1}$) also shows prominence in the spectrum and may be attributed to a S-to-Fe(III) CT. These results are consistent with what is observed in oxidized state of recombinant SOR from *P. furiosus*.²⁷ The oxidized state of SOR displays a band at 660 nm that is assigned as $\text{CysS}^- \rightarrow \text{Fe}^{3+}$ CT while a band at 333 nm has been assigned as $\text{His} \rightarrow \text{Fe}^{3+}$ CT.²⁷ Thus, one possible results is the formation of $[\text{Fe(III)}(\text{L}_{\text{N4}}^{\text{pr}})(\text{S-}p\text{-ClPh})]^{2+}$ in the UV-vis experiment. ESI-MS studies on this species were inconclusive and further studies need to be performed.

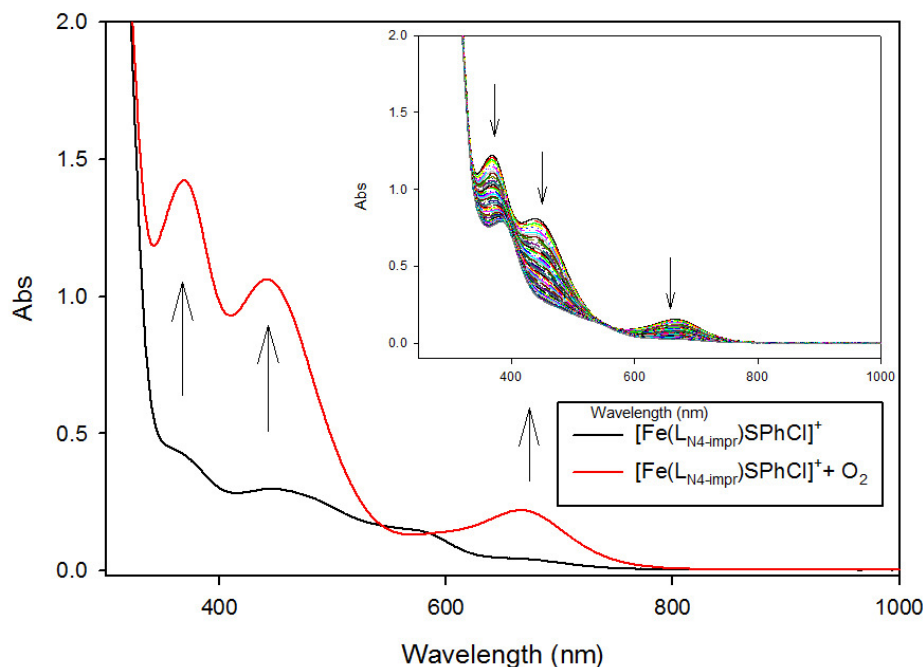


Figure 1.10. UV-vis spectrum of **6** in MeCN at 298 K (black trace) and immediately upon exposure to air (red trace); inset: UV-vis spectral decay of the oxidized species monitored over 6 h at 5 min intervals. Arrows show direction of change.

1.3.2 Reactivity of **4** with H₂O₂

A Fe(III) peroxide intermediate is proposed in the catalytic cycle of SOR.²³ This proposed intermediate shows absorbance centered at 600 nm in rubredoxin oxidoreductase protein, which is known as for its SOR activity.²³ The absorbance of this intermediate, centered at 600 nm, is understood to be due to a hydroperoxo-to-Fe(III) charge-transfer band. To test the possibility of forming the Fe(III) peroxide intermediate, we proposed that complex **4** should be able to form a similar intermediate when reacted with H₂O₂.

To test the possibility of forming a ferric-hydroperoxo species, we monitored the UV-vis spectrum of the reaction of **4** with 1.5 equivalents of H₂O₂•urea in MeOH at 195 K (acetone-dry ice bath). This intermediate can only be trapped at lower temperature because of its thermal instability. The reactivity is proposed to follow a two-step process, where in the first step 0.5 equiv of H₂O₂ converts the Fe(II) complex to an Fe(III)-OH complex. In the second step, one equivalent of H₂O₂ reacts with the Fe(III)-OH to form a ferric hydroperoxide complex that can be trapped at low-temperature and characterized by UV-vis spectroscopy.³² It was observed that upon introduction 1.5 mol-equiv of H₂O₂•urea resulted in a steady rise in a band at 535 nm and the reaction was complete within 4 min after which there was no further change in the spectrum for 1 hour at 195 K. Similar observations were made for a series of pentadentate N₅ ligands such as N₄Py, where the [(N₄Py)Fe^{III}OOH] intermediate complex displayed a λ_{max} at 548 nm, which was assigned as hydroperoxo-to-Fe(III) CT band. Thus, preliminary UV-vis studies of the reaction of **4** with H₂O₂•urea indicate the possible formation of a ferric-hydroperoxo species. Specific spectroscopic techniques such as resonance Raman spectroscopy and EPR will enable us to better understand the electronic nature of the proposed Fe(III)-OOH species formed in the reaction of complex **4** with H₂O₂•urea.

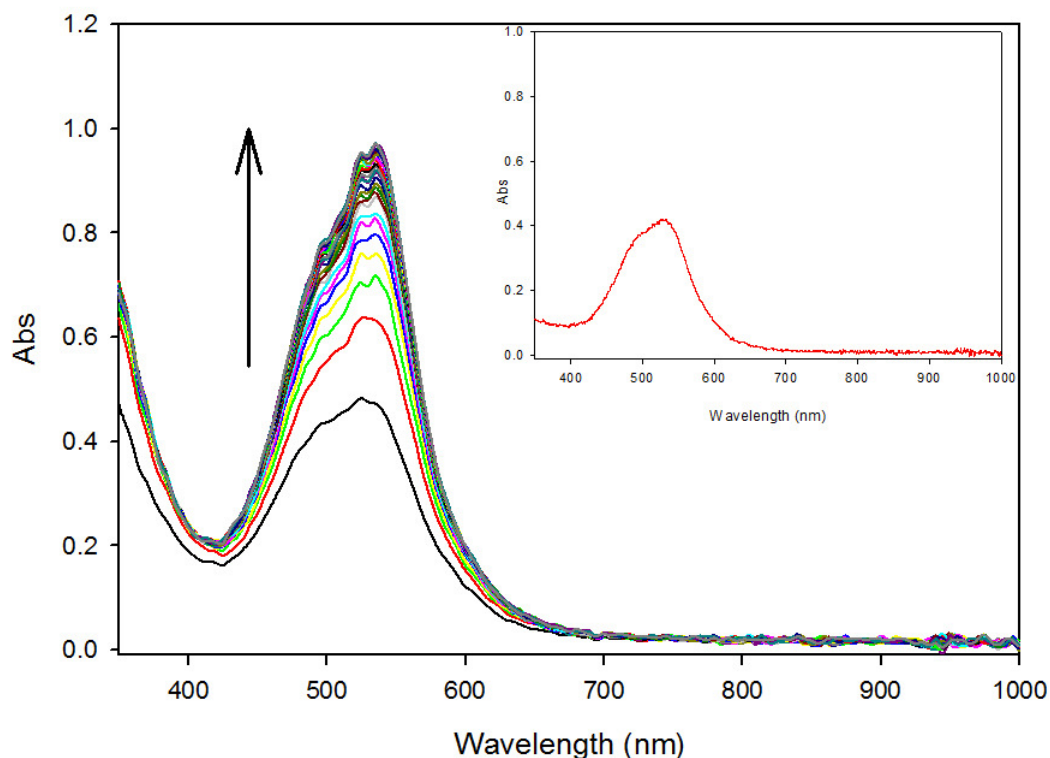


Figure 1.11. UV-vis spectra of **4** (283 μM) + $\text{H}_2\text{O}_2\cdot\text{urea}$ (432 μM , 1.5 mol-equiv) recorded for 4.5 min at 9 s intervals in MeOH at 195 K. Inset: UV-vis spectrum of **4** in MeOH at 195 K. Arrow indicates direction of change.

1.3.2 Reactivity of **4** with *m*CPBA

To test another pathway towards forming the Fe(III)-OOH species, we reacted 0.5 mol-equiv of a peroxyacid such as *m*-chloroperoxybenzoic acid (*m*CPBA) with **4**. This reaction was monitored by UV-vis at 238 K in MeCN. It was observed that the λ_{max} at 480 nm decays while a new peak is observed at 370 nm with an isosbestic point at 417 nm indicating a clean A-to-B conversion (Figure 1.12). The band at 370 nm has not been assigned as of yet but indicates the difference between $\text{H}_2\text{O}_2\cdot\text{urea}$ and *m*CPBA as reagents for Fe(III)-OOH formation.

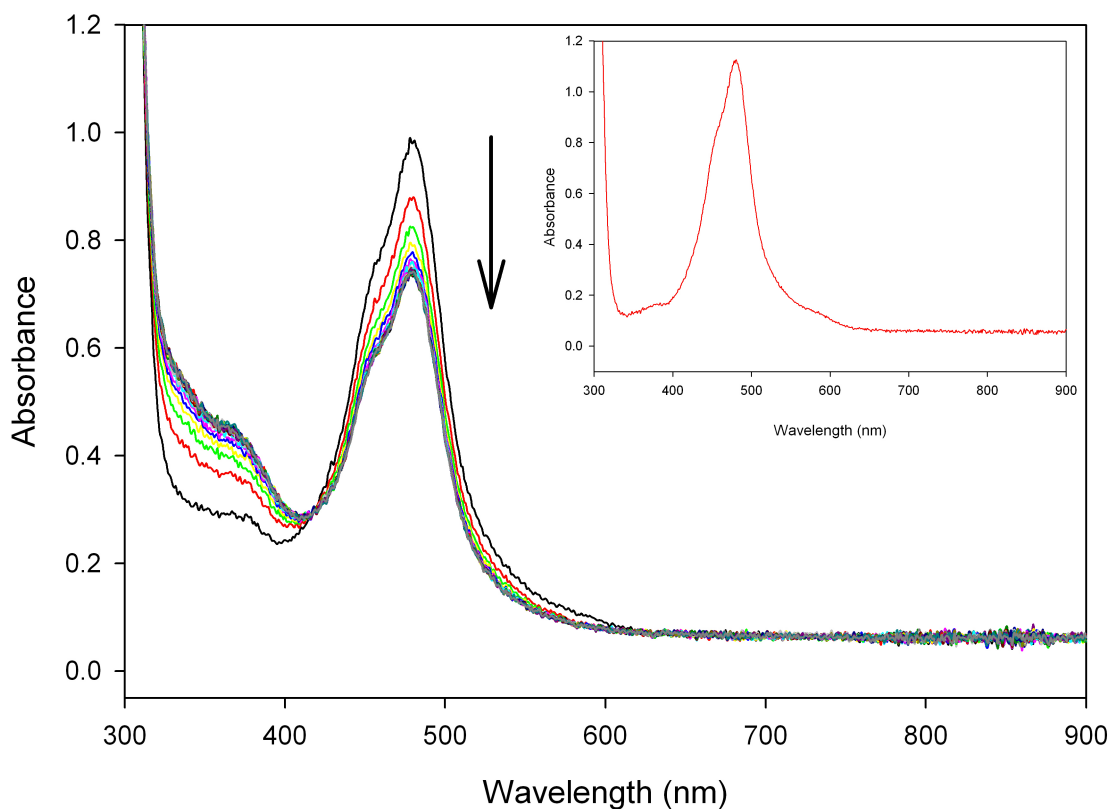


Figure 1.12. UV-vis spectra of **4** (146 μM) + *m*CPBA (73 μM , 0.5 equiv) recorded for 7.5 min at 15 s intervals in MeCN at 238 K. Inset: UV-vis spectrum of **4** in MeCN at 238 K. Arrow indicates direction of change.

1.4 Conclusions

In conclusion, we were able to synthesize a reactive Fe(II) center bound by a planar N_4 ligand with imidazole-N donors that appear able to bind external exogenous ligands such as thiolates to form SOR model compounds. These findings are significant in the prospects of synthetic bioinorganic chemistry, since they could establish the structure and properties of the first Fe(II)-SOR models containing the actual biological donor set. Preliminary studies with oxidants such as H_2O_2 indicate that constructs such as **4** may possibly form an Fe(III)-OOH species, a proposed intermediate in the SOR catalyzed pathway. Additionally, we were able to isolate and structurally characterize unprecedented 8C complexes like **2** with certain ligands.

This complex is redox active and this property can be further exploited as redox indicators and sensors. Other modified 8C complexes have been prepared in our lab and further investigations on their properties are underway.³³

1.5 Experimental Details

1.5.1 General Information. All reagents were purchased from commercial suppliers and used as received unless otherwise noted. Acetonitrile (MeCN), methylene chloride (CH₂Cl₂), tetrahydrofuran (THF), diethyl ether (Et₂O) and pentane were purified by passage through activated alumina columns using an MBraun MB-SPS solvent purification system and stored over 4 Å molecular sieves under a dinitrogen (N₂) atmosphere before use. DMF was purified with a VAC Solvent Purifier containing 4 Å molecular sieves and stored under similar conditions. MeOH and EtOH were purified by distilling over Mg(OR)₂ (R = Me for MeOH, Et for EtOH). All reactions were performed under an inert atmosphere of N₂ using standard Schlenk techniques or in an MBraun Labmaster glovebox under an atmosphere of purified N₂.

1.5.2 Physical Methods. FTIR spectra were collected on a ThermoNicolet 6700 spectrophotometer running the OMNIC software. All samples were run as solids via an ATR diamond transmission window or in a KBr matrix. X-band (9.59 GHz) electron paramagnetic resonance (EPR) spectra were obtained on a Bruker ESP 300E EPR spectrometer controlled with a Bruker microwave bridge at 4.3 K. The EPR spectrometer was equipped with a continuous-flow liquid He cryostat and a temperature controller (ESR 9) made by Oxford Instruments, Inc. Electronic absorption spectra were run at variable temperature using a Cary-50 UV-vis spectrophotometer containing a Quantum Northwest TC 125 temperature control unit, low temperature measurements were measured with the help of a dip-probe apparatus. The UV-vis

samples were prepared anaerobically in gas-tight Teflon-lined screw cap quartz cells with an optical pathlength of 1 cm. Cyclic voltammetry (CV) measurements were performed with a PAR Model 273A potentiostat using a Ag/Ag⁺ (0.01 M AgNO₃/0.1 M ⁿBu₄NPF₆ in CH₃CN) or Ag/AgCl reference electrode, Pt-wire counter electrode and a Glassy Carbon working electrode. Measurements were performed at ambient temperature using 0.1 M ⁿBu₄NPF₆ as the supporting electrolyte. NMR spectra were recorded in the listed deuterated solvent on a 400 MHz Bruker BZH 400/52 or Varian Unity Inova 500 MHz NMR spectrometer at 298 K with chemical shifts referenced to TMS or residual protio signal of the deuterated solvent. Magnetic susceptibility measurements were performed in solution at 298 K using the Evans method on a Varian Unity Inova 500 MHz NMR spectrometer. ESI-MS data were collected on a Perkin Elmer Sciex API I Plus quadrupole mass spectrometer. Elemental microanalysis for C, H, and N was performed at QTI-Intertek in Whitehouse, NJ using a Perkin-Elmer 2400 CHN analyzer. For Mössbauer studies, polycrystalline samples dispersed in high purity boron nitride powder were measured in the temperature range 4.2 K ≤ T ≤ 300 K. A conventional transmission geometry Mössbauer spectrometer was used equipped with a constant acceleration Mössbauer Drive by WebResearch and a Lakeshore-332 Temperature Controller. The source was ⁵⁷Co/Rh maintained at RT. Velocity calibration was performed using a 6 μm-thick iron foil enriched in ⁵⁷Fe. Isomer shifts (δ) are reported with respect to metallic iron at room temperature (RT). Least-square fits were obtained using the Mössbauer fitting software WMOSS (WEBResearch, Medina, MN).

1.5.1 Synthesis of L_{N4}^{Pr}. A batch of 0.357 g (3.24 mmol) of 1-methyl-2-imidazole carboxaldehyde was dissolved in 3-4 mL of dry MeCN. Accordingly, the required amount (0.136 mL, 1.62 mmol) of propane diamine was then dissolved in 1-2 mL of dry MeCN. The solution of diamine was then added to the aldehyde in a flask. There was no color change observed on

addition and the reaction mixture was heated with a water bath at about 50 °C for 18 -20 h. There was no color change after the reaction was stopped. The solvent was then removed by rotovap and the oily residue was subject to high vacuum for 5-10 min to yield a frothy yellow product. Yield = 0.4075 g (97%). ^1H NMR (400 MHz, CDCl_3 , δ from TMS): 2.043 (p, 2H, $-\text{CH}_2-\text{CH}_2-\text{CH}_2-$), 3.69 (t, 4H, $-\text{CH}_2-\text{CH}_2-\text{CH}_2-$), 3.99 (s, 6H, $-\text{CH}_3$), 6.93 (s, 2H, aromatic), 7.10 (s, 2H, aromatic), 8.34 (s, 2H, $-\text{CH}=\text{N}-$). ^{13}C NMR (100.6 MHz, CDCl_3 , δ from TMS): 153.65 ($\text{CH}=\text{N}$), 143.2 (Ar-C), 129.3 (Ar-C), 124.94 (Ar-C), 59.64 (HCH), 35.5(HCH), 32.5 (HCH). FTIR (ATR-diamond, solid), ν_{max} (cm^{-1}): 3379 (br), 3104 (m), 2925 (m), 2838 (m), 1646 (s), 1517 (w), 1474 (s), 1435 (s), 1411 (m), 1366 (m), 1285 (s), 1226 (w), 1147 (m), 1113 (m), 1083 (m), 1021 (m), 965 (w), 919 (m), 752 (m), 707 (m), 688 (m).

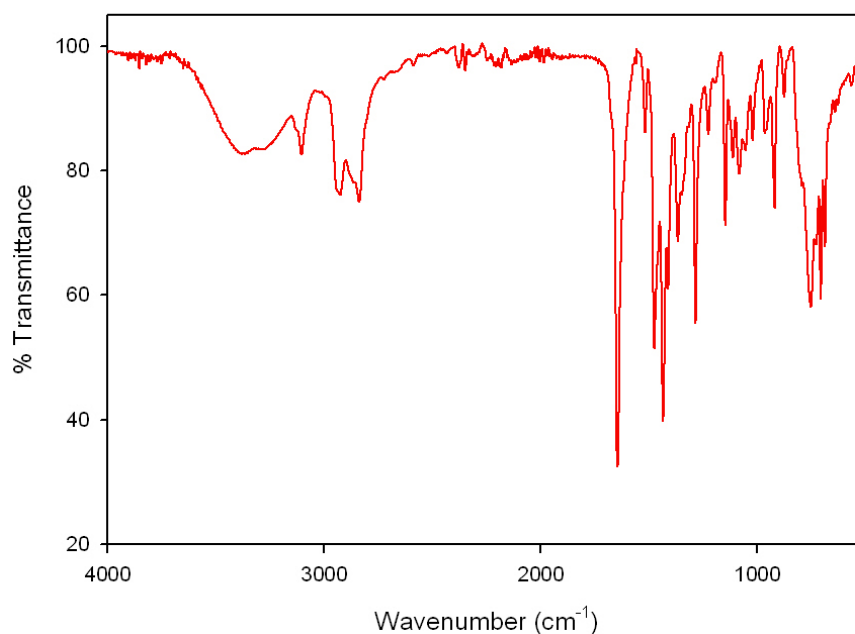


Figure 1.13. FTIR of $\text{L}_{\text{N}4}^{\text{Pr}}$ (solid, ATR-diamond).

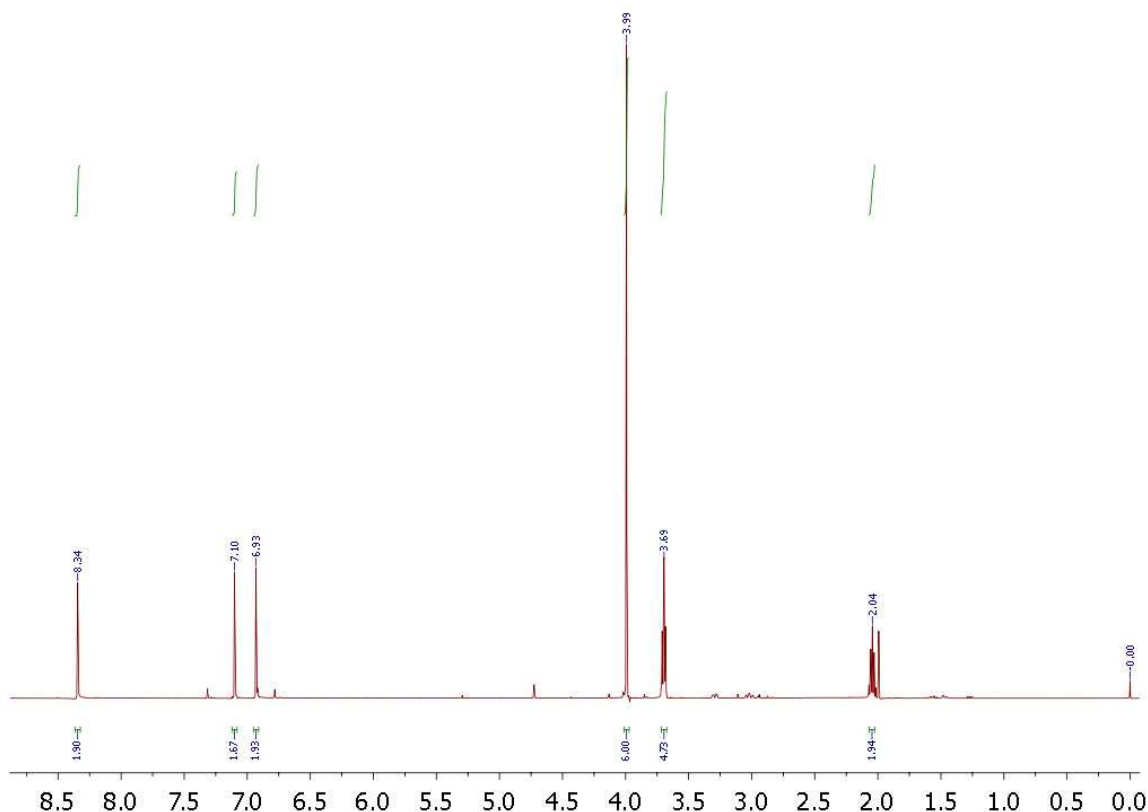


Figure 1.14. ^1H NMR of ligand $\text{L}_{\text{N}4}^{\text{Pr}}$ in CDCl_3 (0.05% v/v TMS) at 298 K.

1.5.2. Synthesis of $[\text{Fe}(\text{L}_{\text{N}4}^{\text{Pr}})(\text{MeCN})_2](\text{BF}_4)_2$ (4). A batch of 0.4475 g (1.732 mmol) of ligand was dissolved in 2-3 mL of MeCN to form a slightly pale colored solution. In another vial 0.5826 g (1.734 mmol) of $[\text{Fe}(\text{H}_2\text{O})_6](\text{BF}_4)_2$ was also dissolved in MeCN. The dissolved iron salt solution was added to the ligand solution with constant stirring. On addition, the solution color turned dark red and was stirred for 30 min. On addition of Et_2O and storing at $-20\text{ }^\circ\text{C}$, a residue is observed at the bottom of the vial. This residue was filtered and dried on high vacuum. Red flocculent material was recovered. Yield: 0.7040 g (1.235 mmol, 70%). FTIR (KBr matrix), ν_{max} (cm^{-1}): 3539 (br), 3153 (br), 2358 (w), 1624 (s), 1582 (m), 1537 (m), 1492 (s), 1454 (s), 1421 (s), 1371 (w), 1291 (s), 1027 (s), 764 (m), 709 (w), 666 (w). UV-vis (MeCN, 298 K), λ_{max} , nm (ϵ , $\text{M}^{-1}\text{cm}^{-1}$): 290 (19,332); 478 (4963). $E_{1/2}$ (quasi) = 0.59 V, E_{red} = -1.72 V (vs. Fc/Fc^+ , MeCN, RT).

Anal. Calcd for $C_{17}H_{24}N_8B_2F_8Fe$: C, 35.83; H, 4.24; N, 19.66. Found: C, 31.35; H, 4.40; N, 16.90. Reported analysis is low for both C and N, which may indicate loss of one or more MeCN axial ligands.

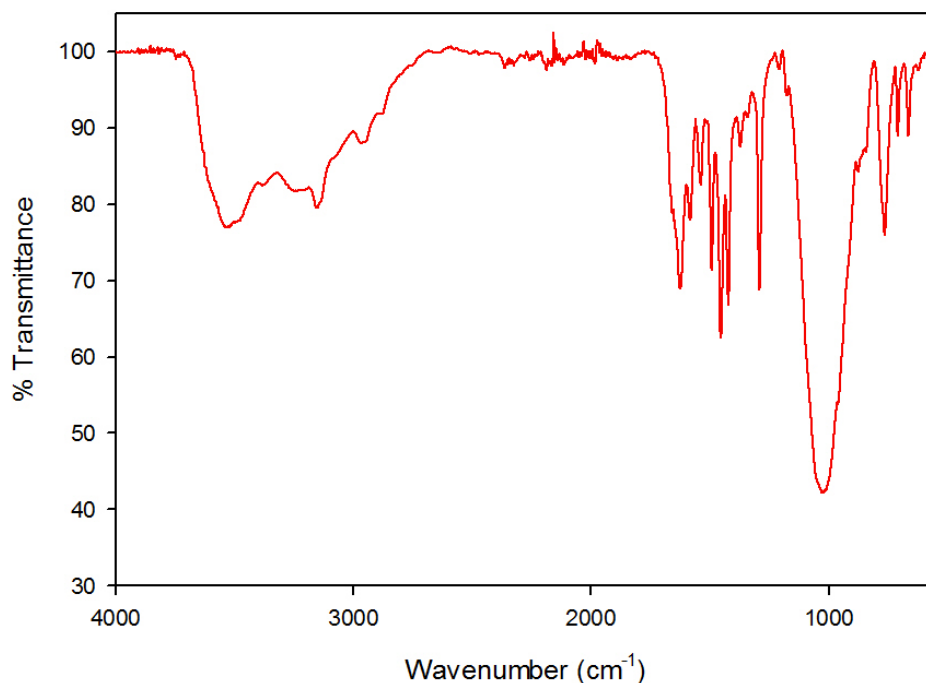


Figure 1.15. FTIR spectrum of complex **4** (KBr Matrix).

1.5.3. Synthesis of $[Fe(L_{N4}^{pr})(DMAP)_2](BF_4)_2$ (5**).** To a batch of 0.0655 g (0.115 mmol) of complex **4** in 2 mL MeCN was added a 3 mL MeCN solution of 0.0590 g (0.484 mmol) of 4-dimethylaminopyridine (DMAP). On addition the color of the solution changed from dark-red to dark-blue instantly. The reaction mixture was stirred for 30 min at RT. The solvent from this reaction mixture was then removed by vacuum yielding a dark-blue residue. This residue was filtered and washed with Et_2O to afford 0.0510 g (0.070 mmol, 60%) of a dark-blue powdered residue. X-ray quality crystals of **5** were grown by diffusing Et_2O into an MeCN solution of **5** at $-30\text{ }^{\circ}C$ in the presence of excess DMAP. FTIR (ATR-diamond, solid), ν_{max} (cm^{-1}): 3157 (w), 2928 (w), 1613 (s), 1575 (m), 1533 (s), 1481 (w), 1446 (m), 1422 (m), 1390 (m), 1349 (w), 1287

(m), 1263 (w), 1232 (m), 1183 (w), 1089 (m), 1031 (s, BF_4), 951 (m), 900 (m), 803 (m), 771 (m), 729 (w), 717 (w), 664 (w). UV-vis (MeCN, 298 K), λ_{max} , nm (qualitative): 610.

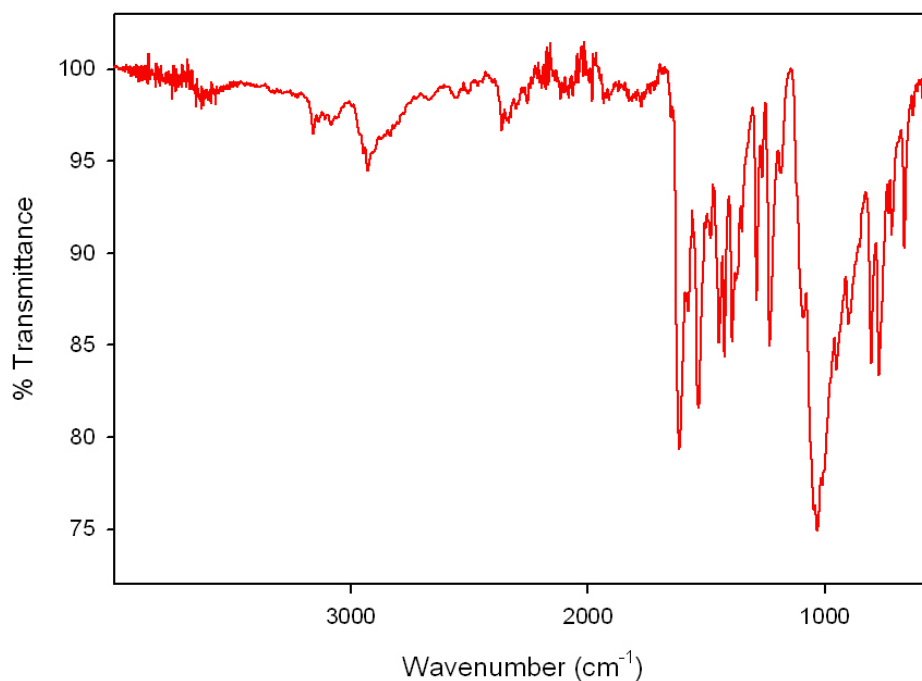


Fig 1.16. FTIR spectrum of **5** (solid, ATR-diamond).

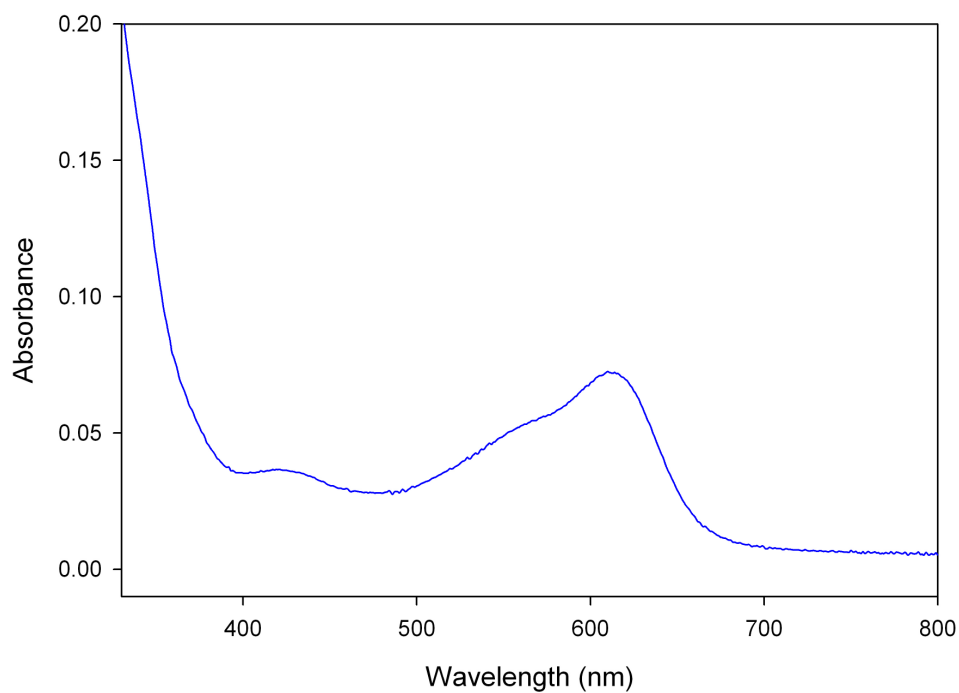


Fig 1.17. UV-vis spectrum of **5** in MeCN at 298 K in the presence of excess DMAP.

1.5.4. Synthesis of [Fe(L_{N4}^{Pr})(S-*p*-ClPh)]BF₄ (6). To a batch of 0.1069 g (0.7392 mmol) of para-chlorobenzenethiol in 4 mL of MeCN was added a 2 mL solution of 0.0177 g (0.7392 mmol) of NaH in MeCN. On addition of NaH, effervescence of H₂(g) is seen in the solution. This solution is further stirred for 10 min until the evolution of H₂(g) ceases. This 6 mL solution is then added to 0.3806 g (0.6679 mmol) of complex **4** in 6 mL of MeCN. On addition, the color of the reaction mixture changes from dark-red to maroon. The reaction mixture was stirred for 40 min after which the solvent was removed via vacuum. To the resultant residue, 5 mL of CH₂Cl₂ was added and stirred for 15 min. The insoluble NaBF₄ was filtered by frit and the filtrate solvent was removed by vacuum to afford a dark-red residue. Yield: 0.2541 g (0.4666 mmol, 70%). FTIR (ATR-diamond, solid), ν_{max} (cm⁻¹): 2384 (w), 1666 (m), 1614 (m), 1567 (m), 1537 (m), 1487 (w), 1468 (s), 1452 (s), 1417 (s), 1385 (m), 1287 (m), 1172 (w), 1087 (s), 1027 (s, BF₄), 1007 (s), 813 (m), 760 (m), 705 (w), 662 (w), 538 (m). $E_{1/2}$ = 0.37 V, E_{red} = -1.10 V (vs. Ag/AgCl, MeCN, RT). LRMS-ESI (m/z): [M - BF₄]⁺ calcd for C₁₉H₂₂ClFeN₆S, 457.07; found, 457.0.

1.5.4. Reactivity of **4 with H₂O₂•urea.** The reaction of **4** with H₂O₂•urea was monitored by UV-vis spectroscopy under anaerobic conditions in MeOH at 195 K (acetone-dry ice bath). A 420 μ L of a 5 mM stock solution of **4** (283 μ M) was added to 7 mL of MeOH in a schlenk tube fitted with a dip-probe assembly. To this solution was added a 220 μ L of a 15 mM stock solution of H₂O₂•urea (432 μ M) was added via syringe. The reaction was monitored by UV-vis for 60 min.

1.5.5. Reactivity of **4 with *m*CPBA.** The reaction of **4** with *m*CPBA was monitored by UV-vis spectroscopy under anaerobic conditions in MeCN at 238 K (MeCN-dry ice bath). A 210 μ L of a 5 mM stock solution of **4** (146 μ M) was added to 7 mL of MeCN in a schlenk tube fitted

with a dip-probe assembly. To this solution was added 105 μL of a 5 mM stock solution of *m*CPBA (73 μM) via syringe. The reaction was monitored by UV-vis spectroscopy for 60 min.

Table 1.6: X-ray parameters for **4** and **5**.

Parameters	4	5
Formula	C ₁₇ H ₂₄ N ₈ B ₂ F ₈ Fe	C ₂₇ H ₄₂ N ₁₀ B ₂ F ₈ Fe
Formula weight	570.15	732.11
Crystal system	Monoclinic	Monoclinic
Space group	<i>P12₁/n1</i>	<i>P12₁/n1</i>
Crystal color, habit	red rectangle	blue rectangle
<i>a</i> , Å	11.052(5)	11.853(5)
<i>b</i> , Å	21.752(5)	18.488(5)
<i>c</i> , Å	11.470(5)	15.470(5)
α , deg	90.000(5)	90.000(5)
β , deg	97.947(5)	101.897(5)
γ , deg	90.000(5)	90.000(5)
<i>V</i> , Å ³	2730.9(18)	3317(2)
<i>Z</i>	4	4
ρ_{calcd} , g/cm ⁻³	1.508	2.072
<i>T</i> , K	293(2)	293(2)
abs coeff, μ (Mo K α), mm ⁻¹	0.634	0.572
θ limits, deg	2.02-28.28	2.43-23.30
total no. of data	37196	43983
no. of unique data	9981	7920
no. of parameters	352	432
GOF on F ²	1.032	1.007
R_1 , ^[a] %	7.49	10.01
wR_2 , ^[b] %	18.71	17.11
max, min peaks, e/Å ³	0.986, -0.876	1.080, -1.002

$$^a R_1 = \Sigma | | F_o | - | F_d | | / \Sigma | F_o | ; ^b wR_2 = \{ \Sigma [w(F_o^2 - F_c^2)^2] / \Sigma [w(F_o^2)^2] \}^{1/2}.$$

References

1. Thompson, A. J.; Gray, H. B. *Curr. Opin. Chem. Biol.* **1998**, 2, 155.
2. Bertini, I.; Gray, H. B.; Stiefel, E. D.; Valentine, J. S., *Biological Inorganic Chemistry Structure and Reactivity*, **2007**, University Science Books, Sausalito, CA.
3. Solomon E. I., *Acc. Chem. Res.* **2007**, 40, 445.
4. Vallee, B. L.; Falchuk, K. H. *Physiol. Rev.* **1993**, 73, 79.
5. Jenney, F. E.; Verhagen, M.; Cui, X. Y.; Adams, M. W. W. *Science* **1999**, 286, 306.
6. Sawyer, D. T.; Valentine, J. S. *Acc. Chem. Res.* **1981**, 14, 393.
7. Carter, G. F.; Margrave, J. L.; Templeton, D. H. *Acta Cryst.* **1952**, 5, 851.
8. Abrahams, S.C.; Collin, R. L.; Lipscomb, W. N. *Acta. Cryst.* **1951**, 4, 15.
9. Castilla, P.; Davalos, A.; Teruel, J. L.; Cerrato, F.; Fernandez-Lucas, M.; Merino, J. L.; Sanchez-Martin, C. C.; Ortuno, J.; Lasuncion, M. A. *Am. J. Clin. Nutr.* **2008**, 87, 1053.
10. Messner, K. R.; Imlay, J. A. *Jour. Biol. Chem.* **1999**, 274, 10119.
11. Massey, V.; Strickland, S.; Mayhew, S. G.; Howell, L. G.; Engel, P. C.; Matthews, R. G.; Schuman, M.; Sullivan, P. A. *Biochem. Biophys. Res. Comm.* **1969**, 36, 891.
12. Imlay, J. A. *Jour. Biol. Inorg. Chem.* **2002**, 7, 659.
13. Imlay, J. A. *Annu. Rev. Microbiol.* **2003**, 57, 395.
14. Valentine, J. S.; Wertz, D. L.; Lyons, T. J.; Liou, L. L.; Goto, J. J.; Gralla, E. B. *Curr. Opin. Chem. Biol.* **1998**, 2, 253.
15. McCandlish, E.; Miksztal, A. R.; Nappa, M.; Sprenger, A. Q.; Valentine, J. S.; Stong, J. D.; Spiro, T. G. *J. Am. Chem. Soc.* **1980**, 102, 4268.
16. Stein, J.; Fackler, J. P.; McClune, G. J.; Fee, J. A.; Chan, L. T. *Inorg. Chem.* **1979**, 18, 3511

17. Fielden, E. M.; Roberts, P. B.; Bray, R. C.; Lowe, D. J.; Mautner, G. N.; Rotilio, G.; Calabres, L. *Biochem. J.* **1974**, *139*, 49.
18. McCord, J. M.; Keele, B. B.; Fridovic, I. *Proc. Natl. Acad. Sci. U.S.A.* **1971**, *68*, 1024.
19. Kurtz, D. M. *Acc. Chem. Res.* **2004**, *37*, 902-908.
20. Yeh, A. P.; Hu, Y. L.; Jenney, F. E.; Adams, M. W. W.; Rees, D. C. *Biochemistry* **2000**, *39*, 2499.
21. Brines, L. M.; Kovacs, J. A. *Eur. J. Inorg. Chem.* **2007**, 29.
22. Clay, M. D.; Jenney, F. E.; Hagedoorn, P. L.; George, G. N.; Adams, M. W. W.; Johnson, M. K. *J. Am. Chem. Soc.* **2002**, *124*, 788.
23. Coulter, E. D.; Emerson, J. P.; Kurtz, D. M.; Cabelli, D. E. *J. Am. Chem. Soc.* **2000**, *122*, 11555.
24. Patra, A. K.; Dube, K. S.; Papaefthymiou, G. C.; Conradie, J.; Ghosh, A.; Harrop, T. C. *Inorg. Chem.* **2010**, *49*, 2032.
25. Diebold, A.; Hagen, K. S. *Inorg. Chem.* **1998**, *37*, 215.
26. Williams, N. J.; Dean, N. E.; VanDerveer, D. G.; Luckay, R. C.; Hancock, R. D. *Inorg. Chem.* **2009**, *48*, 7853.
27. Lippard, S. J. *Prog. Inorg. Chem.* **1967**, *8*, 109.
28. Koch, W. O.; Barbieri, A.; Grodzicki, M.; Schünemann, V.; Trautwein, A. X.; Krüger, H.-J. *Angew. Chem., Int. Ed. Engl.* **1996**, *35*, 422.
29. Clearfield, A.; Singh, P.; Bernal, I. *J. Chem. Soc., Chem. Commun.* **1970**, 389.
30. Oliver, J. D.; Mullica, D. F.; Hutchinson, B. B.; Milligan, W. O. *Inorg. Chem.* **1980**, *19*, 165.
31. Halfen, J. A.; Moore, H. L.; Fox, D. C. *Inorg. Chem.* **2002**, *41*, 3935.

32. Roelfes, G.; Vrajmasu, V.; Chen, K.; Ho, R. Y. N.; Rohde, J. U.; Zondervan, C.; la Crois, R. M.; Schudde, E. P.; Lutz, M.; Spek, A. L.; Hage, R.; Feringa, B. L.; Munck, E.; Que, L. *Inorg. Chem.* **2003**, 42, 2639.
33. Dube, K. S.; Patra, A. K.; Sanders, B.C.; Cheatum, W. H.; Harrop, T. C., *unpublished results*.

CHAPTER 2

COBALT NITROSYL COMPLEXES: STRUCTURE AND REACTIVITY

2.1 Introduction and Intent of Research:

The importance of nitric oxide (NO) as a biological signaling molecule was noted in the early 1980's where NO was reported to induce vasorelaxation.¹ The formation and activity of NO in mammals occurs at heme iron centers such as nitric oxide synthase (NOS) and soluble guanylyl cyclase (sGC).² There is also considerable significance in the activity of the one-electron reduced form of NO termed nitroxyl (NO^- or HNO at physiological pH).³ For example, nitroxyl intermediates have been proposed in the biological denitrification processes in plants, bacteria, and fungi⁴ and play different physiological roles in mammals such as to increase myocardial contractility.⁵ Since metal-bound NO and its derivatives like HNO (together termed reactive nitrogen species or RNS) exhibit unique chemistry than free NO or HNO, an understanding of the fundamental structure, bonding, and reactivity is warranted to understand biological function. The long-term goal of this research is to understand the properties and activation of metal-bound NO and its derivatives at biologically relevant metal centers such as Fe, Co, and Mn. The overall objective of this research, which is a step toward attainment of the long-term goal, is to determine the factors required to generate Co-nitroxyl complexes as well as what makes them sufficient HNO donors for potential therapeutics. It is our central hypothesis that the redox-inert character of Co(III) will allow for the successful isolation and characterization of discrete and stable nitroxyl complexes i.e. $\{\text{CoNO}\}^8$ systems (*vide infra*).

Furthermore, one-electron reduction to the corresponding $\{\text{CoNO}\}^9$ state should render these molecules as kinetically competent NO^-/HNO donors to biological targets.

2.1.1 Nitric Oxide ($\text{NO}\bullet$) and Nitroxyl (HNO/NO^-):

NO is a gaseous diatom that is thermally unstable in the atmosphere. It is not only one of the by-products of combustions of fossil fuels, but also an important cell signaling molecule in mammalian physiology.⁶ These highlights of NO 's biological importance warrant a discussion of the properties of this inorganic molecule. Considering MO theory, the electronic configuration of the valence shell of NO is $(2s\sigma_1)^2, (2s\sigma_1^*)^2, (2p\pi)^4, (2p\sigma_2)^2, (2p\pi^*)^1$ (Figure 2.1). NO is thus a paramagnetic molecule with one unpaired electron and a bond order of 2.5. This bond order is reflected in the NO bond distance of 1.15 Å, which makes it between that of an N-O double (1.18 Å) and triple bond (1.06 Å). The unusual bond order and redox non-innocence of NO make IR spectroscopy a valuable tool in identifying redox congeners of NO e.g. free NO reveals a ν_{NO} stretching frequency at 1875 cm^{-1} while NO^+ and NO^- display ν_{NO} at 2377 cm^{-1} and 1470 cm^{-1} respectively.⁷ Additionally, EPR studies of NO have shown that 60% of the unpaired spin-density is on the nitrogen.⁸

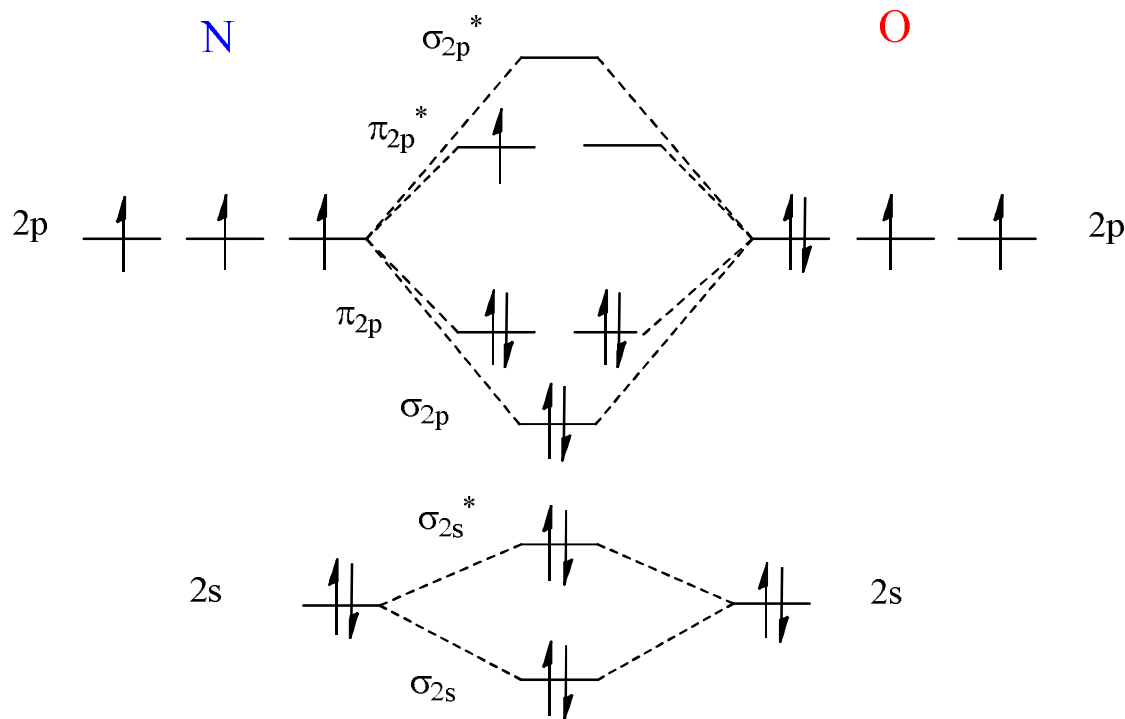


Figure 2.1. MO diagram for the valence shell of NO.

NO is redox-active and can interact with metals in the nitrosonium (NO^+) or nitroside/nitroxyl (NO^-/HNO) forms. The electron affinity of NO is low (0.024 eV)⁹ and when reduced to NO^- , the incoming electron is placed in a π^* antibonding orbital reducing the bond order to 2 and weakening the N-O bond, which results in an N-O distance of (1.26 Å).¹⁰ One can thus say that the N-O bond is activated in this case and is poised for further reactivity which can eventually cleave the bond or result in other reactivity.

Bonding of NO to metal centers can be envisioned in two ways. Considering the valence bond approach, one can assume that the bond formed between the metal and NO is due to donation (NO^+) or acceptance of one electron (NO^-) to the NO ligand from the metal along with a dative bond formed due to lone pair donation from N to metal. Thus, the two scenarios mentioned above involve a net donation of 3 electrons (in the case of NO^+) or 1 electron (in the case of NO^-). However, a better understanding of these systems is achieved through the MO

theory approach where in addition to the σ -donation from N to the metal orbital, there is significant amount of electron donation from d-orbitals to the π^* antibonding orbitals of NO (i.e. π -backbonding) resulting in a highly covalent and delocalized M-NO bond. Thus, attempts to classify metal nitrosyls being coordinated as NO^+ , NO^\bullet , or NO^- have lead to considerable heated debate.¹¹ A better system of defining the electronic nature of metal nitrosyl complexes was proposed by Enemark and Feltham in 1974 where the metal in the M-NO bonding unit is not assigned a formal oxidation state.¹² Instead, the total number of electrons in the metal d and NO π^* are counted in the M-NO unit as a whole e.g. $\{\text{MNO}\}^x$ where x is the M d and NO π^* summation. For instance, $\{\text{FeNO}\}^7$ nitrosyls can be considered as low-spin Fe(II) (d^6) coordinated to NO^\bullet ($1 \pi^*$).¹³ Such classification has lead to accurate predictions of metal nitrosyl bonding parameters in the literature¹⁴ and will be used throughout this chapter.

2.1.2 Chemistry Relevant to Cobalt-Nitrosyls:

Studies on iron-nitrosyl complexes have been performed in detail over a period of several decades, from coordination complexes like $[\text{Fe}_2(\mu\text{-I})_2(\text{NO})_4]$ ¹⁵ to bio-relevant heme-nitrosyls. Most of these complexes have been classified as $\{\text{FeNO}\}^6$ or $\{\text{FeNO}\}^7$ systems.¹⁴ However, reduced iron-nitrosyl complexes of the $\{\text{FeNO}\}^8$ form are underexplored¹⁶ despite their intermediacy of such systems in metalloenzymes like NOS and nitric oxide reductase (NOR) and the potential to use them as nitroxyl-donor platofrms.^{17,18} Mechanistic investigations of the enzyme NOR, an important enzyme in the global nitrogen cycle, revealed a reduced $\{\text{FeNO}\}^8$ complex as one of the reactive-intermediates.¹⁹ This intermediate is very reactive and difficult to investigate spectroscopically due to its inherent instability and reactivity.¹⁵ To investigate such

reduced nitrosyl species, isoelectronic analogues can be obtained by replacing Fe with Co, which has been done for porphyrin-based systems.²⁰ In this regard, we designed and synthesized two $\{\text{CoNO}\}^8$ complexes in a ligand platform inspired by hemes and similar to a series of $\{\text{FeNO}\}^8$ complexes synthesized in our lab.²¹ Indeed, these ligands are similar in donor type and electronic nature of the ligating nitrogens of the porphyrin macrocycle in heme, which is associated with NO chemical biology (Figure 2.2).²²

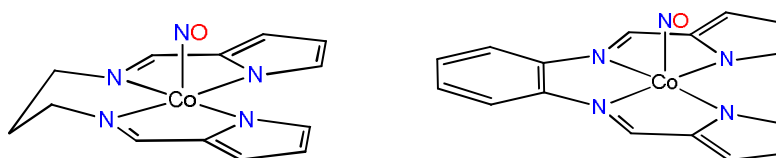


Figure 2.2. $\{\text{CoNO}\}^8$ complexes, $[\text{Co}(\text{LN}_4^{\text{Pr}})(\text{NO})]$ (**1**) (left) and $[\text{Co}(\text{LN}_4^{\text{Ph}})(\text{NO})]$ (**2**) (right), utilized in this work.

Cobalt nitrosyls have been reported in biology such as in cobalamin (vitamin B₁₂)²³ and are known to have an inhibitory effect on methyltransferase activity of methionine synthase.²⁴ Furthermore, biological cobalt-nitrosyls like nitrosyl-cobinamide are known NO releasing agents that show increase in blood flow in isolated mouse hearts that are $\geq 60\%$ more potent than organic NO donors such as nitroglycerine.²⁵ Hence, the potential of cobalt-nitrosyls as NO therapeutics warrant a better understanding of these systems in discrete synthetic complexes such as **1** and **2**.

Cobalt-nitrosyls, while reported in the literature,^{20,26,27} are not as abundant as the corresponding iron systems. Some examples, along with their structural and spectroscopic data, are displayed below in Figure 2.3 and Table 2.1. For the most part, Co-NO complexes are classified as $\{\text{CoNO}\}^8$ systems according to the Enemark-Feltham notation and are typically assigned as low-spin Co(III)-NO⁻ species. The majority of these Co-nitrosyls are diamagnetic ($S = 0$), display severely bent Co-N-O angles ($\sim 120^\circ$) consistent with sp^2 -hybridized nitrogen, and

demonstrate short N-O distances (1.15 Å) and longer M-N distance (1.833 Å) than corresponding {MNO}⁷ (~1.8 Å) complexes suggestive of the relative lability of the Co-N bond.^{14,20} The {CoNO}⁷ and {CoNO}⁹ systems are virtually nonexistent.²⁷ Furthermore, the reactivity of Co-NO compounds is underdeveloped – a gap in knowledge, which this work aims to fill.

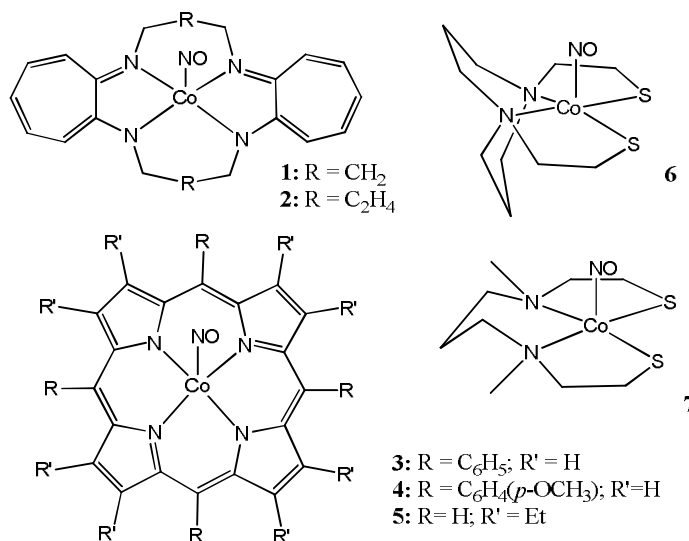


Figure 2.3. Selected examples of structurally characterized {CoNO}⁸ cobalt nitrosyls.

Table 2.1. Selected structural parameters of {CoNO}⁸ complexes from Figure 2.3.

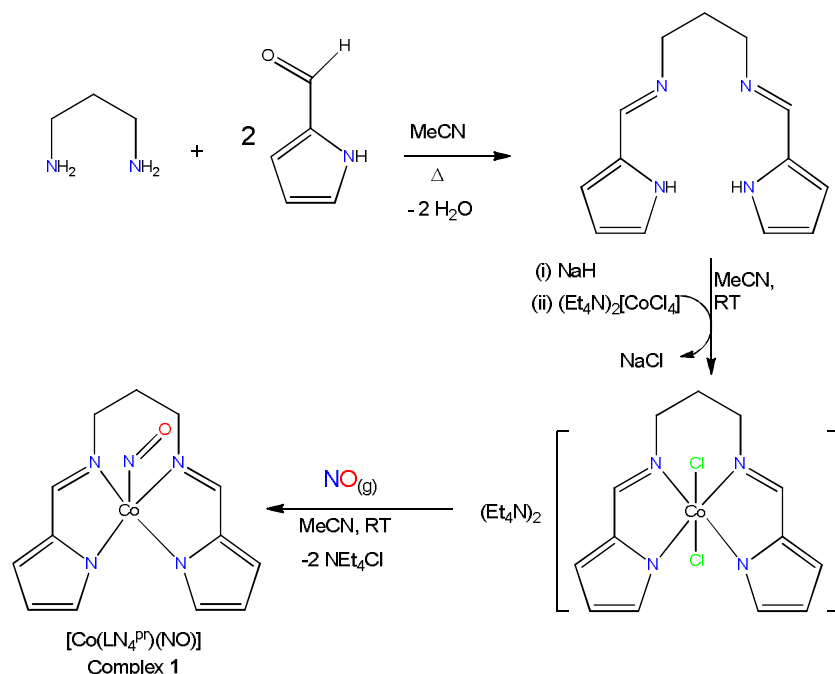
Compound	Co-N (Å)	N-O (Å)	Co-N-O (deg)	ν_{NO} (cm ⁻¹)	Ref
[Co(TC-3,3)(NO)] (1)	1.785(6)	1.137(7)	127.3(6)	1656	26
[Co(TC-4,4)(NO)] (2)	1.779(6)	1.151(9), 1.18(2) *	128.9(6), 134.9(9) *	1584	26
[Co(TPP)(NO)] (3)	1.833(53)	1.01(2)	135.2(8)	1689	20
[Co(T(<i>p</i> -OCH ₃)PP)(NO)] (4)	1.855(6)	1.159(8)	120.6(5)	1696	14
[Co(OEP)(NO)] (5)	1.8444(9)	1.1642(13)	122.70(8)	1677	14
[Co(bme-daco)(NO)] (6)	1.765(4)	1.173(7), 1.160(16)	129.6(8), 128.7(4)	1600	27
[Co(bme-pda)(NO)] (7)	1.7818(14)	1.164(10), 1.148(5)	130.1(3), 126.7(10)	1596	27

* bond distance/angle assigned due to disorder in X-ray structure.

2.2 Results and Discussion:

2.2.1 Synthesis:

The design of the ligand was based on the porphyrin cofactor found in biological heme proteins. These types of coordination units are often associated with the activation/transport/synthesis of small gaseous diatoms such as O_2 and NO .²⁸ The ligands utilized in this research, namely LN_4^{pr} and LN_4^{ph} (Scheme 2.1), are predisposed to form a planar N_4 coordination unit around the metal center, which replicates the structural and electronic properties featured by porphyrin ligands. In addition to their heme-like properties, the advantage of these ligand platforms is their relative ease of synthesis, which is only a one step Schiff-base condensation reaction between the appropriate diamine and the pyrrole aldehyde (Scheme 2.1). Overall, the synthesis affords high yields of the ligands (80-85%) with no need for purification (details below).



Scheme 2.1. Synthesis of the ligand, LN_4^{pr} , and the complex, $[Co(LN_4^{pr})(NO)]$ (1). The synthesis of LN_4^{ph} and the complex, $[Co(LN_4^{ph})(NO)]$ (2), follows a similar route with a different diamine.

(Ligands) The synthesis of the ligands (LN_4^{pr} , LN_4^{ph}) is achieved by reacting two equivalents of pyrrole-aldehyde with the appropriate diamine to afford the Schiff base ligands (1,3-propane diamine or 1,2-phenylenediamine are used for LN_4^{pr} and LN_4^{ph} , respectively). The reaction is carried out in MeCN at 40 °C in the presence of 4 Å molecular sieves. This temperature appears ideal for this particular condensation and performing the reaction with sieves removes the water by-product, thus driving the forward reaction. LN_4^{pr} and LN_4^{ph} were characterized by $^1\text{H}/^{13}\text{C}$ NMR and FTIR spectroscopies. A key feature in the IR spectrum of these ligands is the presence of a strong band between 1610-1630 cm^{-1} , which is representative of the imine C=N stretch.

(Co Complexes) The corresponding Co complexes with these ligands were prepared to study the interactions and chemical transformations of NO when bound to cobalt centers in a heme-like environment. The synthesis of the Co-NO complexes was achieved in two steps: (i) *in situ* formation of the Co(II) complex that we tentatively assign as $(\text{Et}_4\text{N})_2[\text{Co}(\text{LN}_4^{\text{R}})\text{Cl}_2]$ and (ii) displacement of the chloride ligands with NO(g) to afford the $\{\text{CoNO}\}^8$ nitrosyls, $[\text{Co}(\text{LN}_4^{\text{pr}})(\text{NO})]$ (**1**) and $[\text{Co}(\text{LN}_4^{\text{ph}})(\text{NO})]$ (**2**). To generate the Co(II)-Cl precursor complexes, the ligand is reacted with two equivalents of NaH to deprotonate the pyrrole-N; the deprotonated ligand is then reacted with one equivalent of $(\text{Et}_4\text{N})_2[\text{CoCl}_4]$ to generate the red-colored Co(II)-Cl complexes. Once reaction is complete (as noted by the intensity of the color ~ 30 min), nitrosylation is performed by purging Ascarite-purified NO(g) directly into the MeCN solution containing the Co(II)-Cl complex for ~1 min at RT. Immediate reaction is observed and indicated by the rapid color change from red to dark-red and the precipitation of microcrystalline $\{\text{CoNO}\}^8$ material in the reaction flask. Overall, the synthesis is straightforward with modest-to-good yields (~50-75%).

2.2.2 X-ray Structures:

In order to study the coordination geometry and nature of the Co-bound nitrosyl ligand in these complexes, X-ray crystallographic analysis is critical. Single crystals of **1** and **2** were obtained by diffusion of diethyl ether into THF solutions of the complexes. Despite the high interest in metal nitrosyl complexes, there are relatively few Co-NO complexes (Table 2.1) and **1** and **2** add to this exclusive class of structurally characterized Co-NO complexes. The parameters from **1** and **2** thus form a benchmark for future Co-NO synthetic complexes as well as those that may be traversed in biology.

The structure of complex **1** shows the coordination of the four N atoms from the LN₄^{Pr} frame to Co is near planar in nature forming two five-member and one six-member chelate ring with the metal (Figure 2.4). The coordination geometry about the Co center can best be described as a distorted square-pyramid with the nitrosyl in the axial position and a value τ of 0.27.²⁹ As expected, the Co-N_{imine} bonds are slightly longer (avg: 1.9389(11) Å) than the Co-N_{pyrrole} (avg: 1.9197(13) Å) with the Co-N(O) being the shortest (1.7890(11) Å) presumably due to sufficient π -backbonding (Table 2.2). The shorter distances from the pyrrole-N is consistent with the stronger ligand-field of this donor as a result of its anionic nature. The Co-N distances are comparable to Co-N distances in other {CoNO}⁸ nitrosyls. For example, [Co(TPP)(NO)] and [Co(OEP)(NO)] display Co-N_{TPP} and Co-N(O) distances of 1.98 and 1.83 Å,¹⁴ respectively (Table 2.1). The distances in **1** are more consistent; however, with the non-porphyrin {CoNO}⁸ species like the Co-tropocoronand-NO complexes that afford Co-N of ~1.90 Å and Co-N(O) of ~1.78 Å (Table 2.1).²⁶ All these distances are indicative of the low-spin nature of the Co center in **1** and other {CoNO}⁸ systems. Analogous to other {CoNO}⁸ complexes, the Co-N-O angle in **1** is severely bent (125.97(9) °) and consistent with sp² hybridization at the nitrosyl N.²⁰ This

angle is more bent than in the corresponding $\{\text{FeNO}\}^7$ analogue (avg Fe-N-O: $\sim 160^\circ$) of the same ligand, which further supports the relative reduced nature of the NO in this complex. The N-O distance in **1** (1.1551(15) Å) is also typical for the $\{\text{CoNO}\}^8$ formulism. A comparable example is that of $[\text{Co}(\text{T}(p\text{-OMe})\text{PP})(\text{NO})]$ and $[\text{Co}(\text{TC-3,3})(\text{NO})]$ which show N-O distances of 1.1598(8) and 1.137(7) Å, respectively (Table 2.1).^{14,26} Another notable feature in the structure of **1** was that no disorder was found in the NO group at 100 K, which is especially important since other $\{\text{CoNO}\}^8$ complexes show significant disorder in the NO group at room temperature (Table 2.1).^{26,27} The negative nature of the NO ligand could also be revealed in its tendency to point away from the pyrrole-N in **1** where it eclipses one of the imine-Ns. This observation has also been noted in another $\{\text{CoNO}\}^8$ species that we synthesized (*vide infra*).

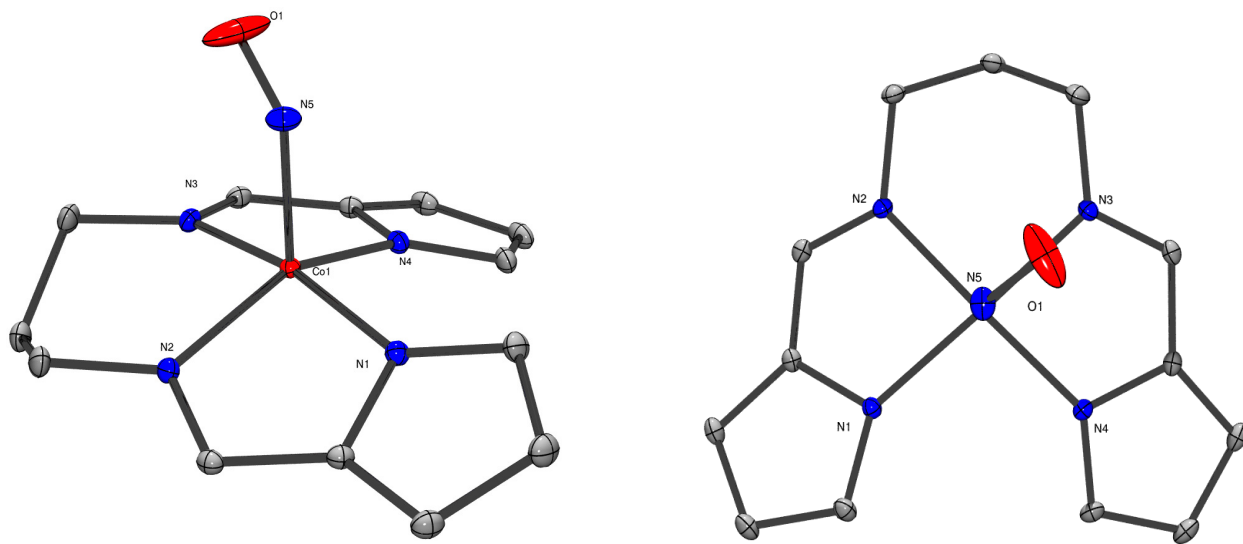


Figure 2.4. ORTEP diagram of **1** at 30% thermal ellipsoids (left, side-view; right, top-view). H atoms omitted for clarity.

Table 2.2. Selected bond distances (Å) and angles (deg) for **1**.

[Co(LN ₄ ^{prop})NO] (1)			
Co1-N1	1.9275(10)	N1-Co1-N4	96.61(4)
Co1-N2	1.9432(11)	N1-Co1-N5	96.49(5)
Co1-N3	1.9345(11)	N2-Co1-N3	92.49(4)
Co1-N4	1.9118(13)	N2-Co1-N4	152.26(4)
Co1-N5	1.7890(11)	N2-Co1-N5	103.70(5)
N5-O1	1.1551(15)	N3-Co1-N4	82.60(4)
O1-N5-Co1	125.98(9)	N3-Co1-N5	94.58(5)
N1-Co1-N2	82.99(4)	N4-Co1-N5	103.90(4)
N1-Co1-N3	168.75(4)		

The asymmetric unit of **2** contains four unique and symmetrically unrelated molecules. The four molecules in the asymmetric unit match well with each other in terms of bond angles and distances (Table 2.3). The only difference in these structures is the orientation of the Co-N-O vector (Figure 2.5). In two molecules, the NO vector lies between the N_{imine} and N_{pyrrole} donors (Figure 2.6), while the other two molecules have the NO vector pointing in between the two N_{imine}, again, qualitatively suggestive of the anionic nature of the NO in **2**. The structure of **2** is similar to **1**, but with a more ordered and essentially square-pyramidal coordination geometry ($\tau_{\text{avg}} = 0.001$) due to the extended aromatic π -system of the LN₄^{ph} ligand frame in **2** versus **1** (Table 2.1, 2.3). The average Co-N_{imine}, Co-N_{pyrrole}, and Co-N(O) distances are 1.894(4), 1.932(4), and 1.802(4) Å, respectively (Table 2.3). Most of these distances are shorter than in **1** and explained based on the location of the Co which sits perfectly in the LN₄^{ph} plane. In fact, the most significant difference in **1** versus **2** is the value of τ (0.27 and 0.001, respectively) and is almost analogous to the changes observed in the heme of hemoglobin undergoing the high-to-low spin transition upon binding O₂. The average N-O distance in **2** is 1.146(6) and the average

Co-N-O angle is 125.4° , which are comparable to other $\{\text{CoNO}\}^8$ derivatives (*vide-supra*) (Figures 2.5, 2.6; Table 2.1, 2.3).

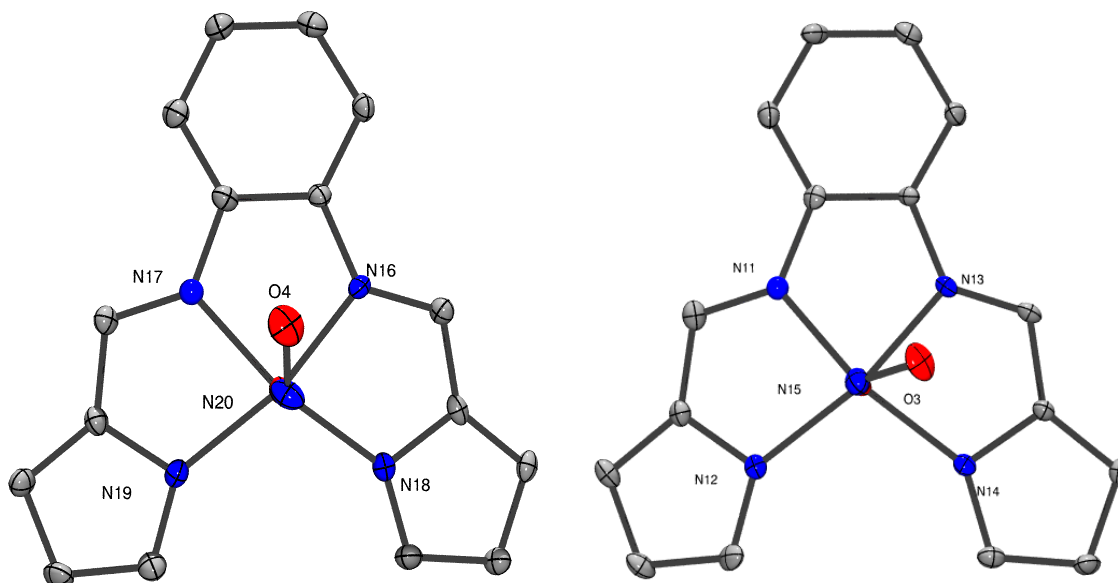


Figure 2.5. ORTEP diagrams of two independent molecules of **2** in the asymmetric unit (top-view looking above Co-N-O vector) at 30% thermal ellipsoids showing the two perspectives of the Co-NO vector. H atoms omitted for clarity.

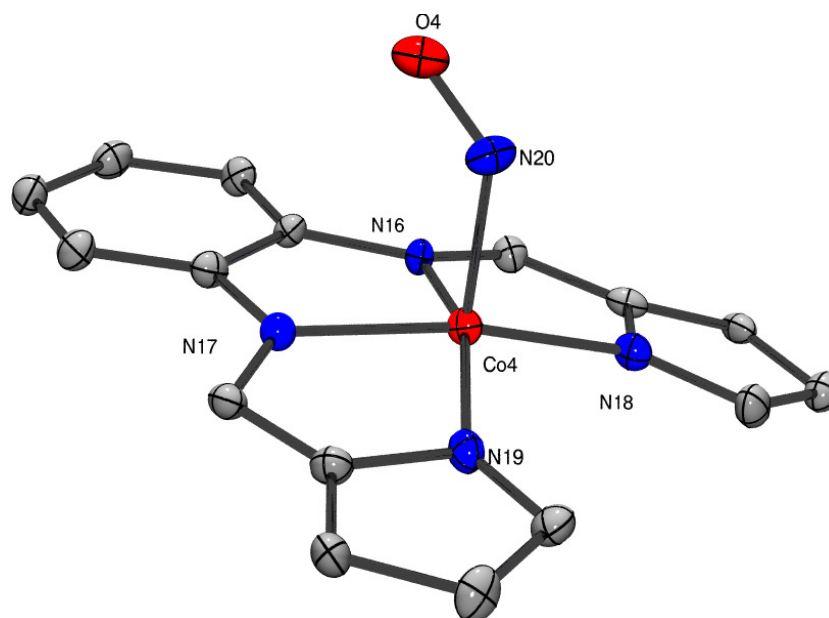


Figure 2.6. ORTEP diagram of **2** (side-view) at 30% thermal ellipsoids. H atoms omitted for clarity.

Table 2.3. Selected bond distances and angles for the four molecules in the asymmetric unit of **2**.

Parameter	1	2	3	4	Average
Co-N _{imine}	Co1-N1: 1.896(3)	Co2-N6: 1.887(4)	Co3-N11: 1.889(4)	Co4-N16: 1.885(4)	1.894(4)
	Co1-N2: 1.904(3)	Co2-N7: 1.903(4)	Co3-N13: 1.899(4)	Co4-N17: 1.888(4)	
Co-N _{pyrrole}	Co1-N3: 1.934(4)	Co2-N8: 1.930(4)	Co3-N12: 1.911(4)	Co4-N18: 1.924(4)	1.932(4)
	Co1-N4: 1.925(3)	Co2-N9: 1.932(4)	Co3-N14: 1.954(4)	Co4-N19: 1.944(5)	
Co-N(O)	Co1-N5: 1.787(3)	Co2-N10: 1.806(4)	Co3-N15: 1.807(4)	Co4-N20: 1.811(5)	1.802(4)
N-O	1.132(5)	1.164(5)	1.148(6)	1.143(6)	1.146(6)
Co-N-O	127.4(4)	124.5(3)	124.5(4)	125.2(4)	125.4(4)
τ	0.0045	0.01	0.014	0.0118	0.01

2.2.3 Characterization

IR spectroscopy is very useful for metal nitrosyl complexes as the NO stretching frequency (ν_{NO}) is in a defined spectral window (1600-2000 cm^{-1}) and with high intensity. The IR data clearly indicated the presence of the NO ligands in the complexes with strong ν_{NO} bands at 1645 and 1656 cm^{-1} (KBr pellet) for **1** and **2**, respectively (Figures 2.7-2.8). These values are consistent with ν_{NO} observed in other bent $\{\text{CoNO}\}^8$ nitrosyls such as $[\text{Co}(\text{TPP})(\text{NO})]$ ($\nu_{\text{NO}} = 1689 \text{ cm}^{-1}$)²⁰ and $[\text{Co}(\text{TC-3,3})(\text{NO})]$ ($\nu_{\text{NO}} = 1654 \text{ cm}^{-1}$) (Table 2.1).²⁶ The assignment of ν_{NO} was further confirmed by using $^{15}\text{NO}(\text{g})$ to form **1**- ^{15}NO and **2**- ^{15}NO with ν_{NO} of 1617 cm^{-1} ($\Delta\nu_{\text{NO}}$: 28 cm^{-1}) and 1629 cm^{-1} ($\Delta\nu_{\text{NO}}$: 27 cm^{-1}), respectively and consistent with the harmonic oscillator model. It is interesting to note that ν_{NO} in **1** lies in between the analogous $\{\text{FeNO}\}^7$ (1695 cm^{-1}) and $\{\text{FeNO}\}^8$ (1604 cm^{-1}) complexes with LN_4^{pr} .²¹ If one tentatively assigns the NO as NO^\bullet in $\{\text{FeNO}\}^7$ and NO^- in $\{\text{FeNO}\}^8$, then it may appear that the NO in **1** is a hybrid of the two. Additionally, it may be best to describe the oxidation states of the Co and NO in **1** as a resonance hybrid between low-spin $\text{Co}(\text{II})\text{-NO}^\bullet$ and low-spin $\text{Co}(\text{III})\text{-NO}^-$. However, the LN_4^{ph} system affords an $\{\text{FeNO}\}^8$ complex with ν_{NO} at 1654 cm^{-1} , which matches well with **2** (Figure 2.8) revealing that IR is probably not the best gauge of NO oxidation state in these systems.²¹

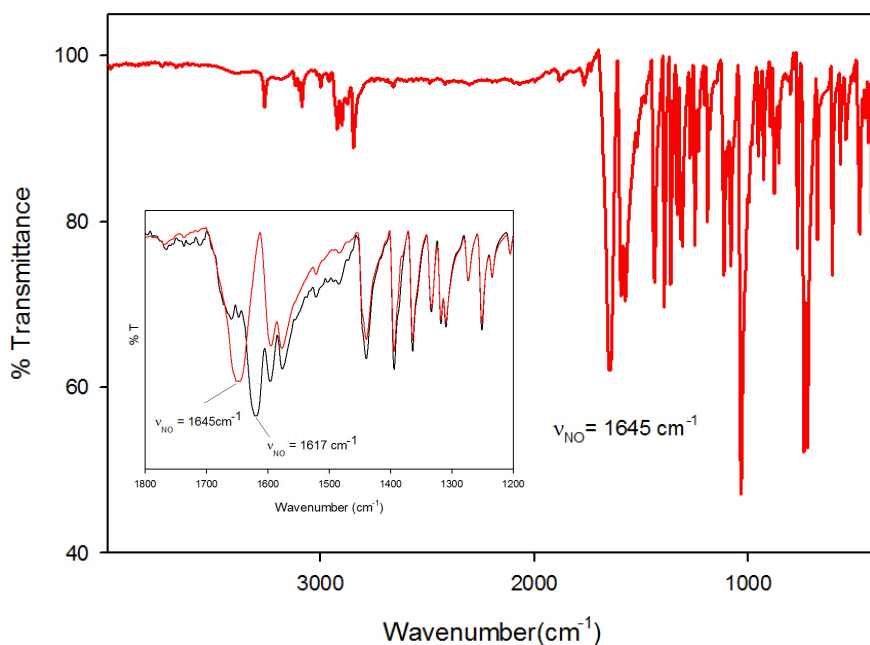


Figure 2.7. FTIR spectrum of $[\text{Co}(\text{LN}_4^{\text{Pr}})(\text{NO})]$ (**1**) in a KBr matrix. Inset: NO stretching frequency region comparing **1** (red trace) and **1**- ^{15}NO (black trace).

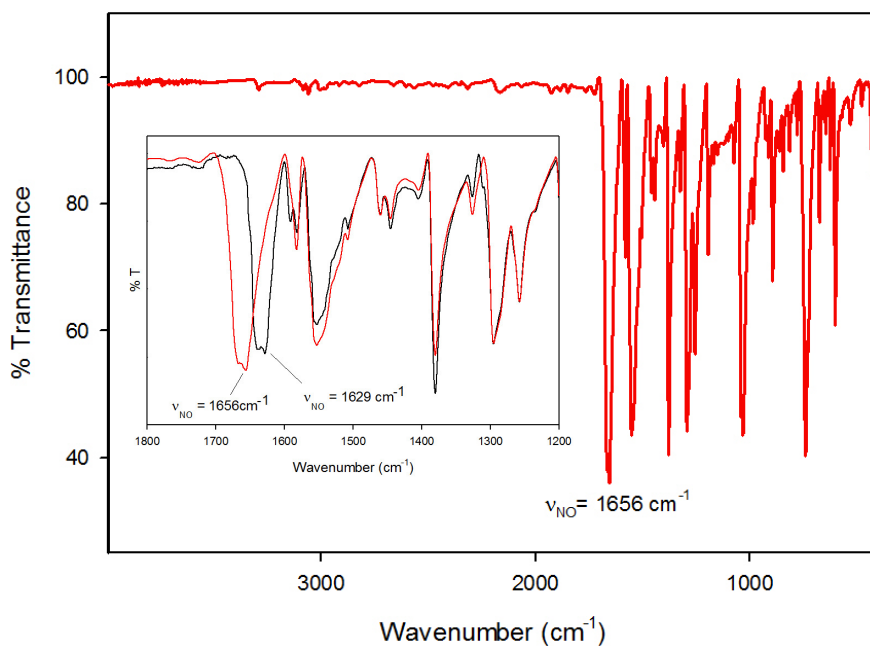


Figure 2.8. FTIR spectrum of $[\text{Co}(\text{LN}_4^{\text{Ph}})(\text{NO})]$ (**2**) in a KBr matrix. Inset: NO stretching frequency region comparing **2** (red trace) and **2**- ^{15}NO (black trace).

Complexes **1** and **2** are diamagnetic ($S = 0$), which is consistent with the $\{\text{CoNO}\}^8$ assignment regardless of Co or NO^- oxidation state (i.e. low-spin $\text{Co(III)} = d^6$ ($S = 0$) and NO is also $S = 0$; low-spin $\text{Co(II)} = d^7$ ($S = 1/2$) with an $S = 1/2$ NO^\bullet that are antiferromagnetically

coupled). The ^1H NMR spectra of **1** and **2** clearly indicate the diamagnetic nature of these $\{\text{CoNO}\}^8$ complexes (Figures 2.9, 2.10). This would confirm the anti-ferromagnetic coupling of unpaired electrons from the Co d and NO π^* orbitals if the Co(II)-NO assignment is correct. All ligand protons are clearly resolved with the expected multiplicities. Slight broadening and splitting of the $-\text{CH}_2-$ propyl linker in **1** is indicative of the slow dynamic nature of the sp^3 hybridized carbons on the ligand frame making them resolved on the NMR timescale. Such splitting is not observed with the phenyl linker in the ^1H NMR of **2**, confirming the symmetry maintenance and rigidity of the ligand frame, which is evident from its structure and τ value. The ^{15}N NMR of **1**- ^{15}NO displays a ^{15}N shift at 821 ppm in $\text{THF-}d_8$ versus CH_3NO_2 (Figure 2.11), indicative of the severely bent Co-N-O bond in **1**. Other bent cobalt nitrosyls like $[\text{Co}(^{15}\text{NO})(\text{benacen})]$ ($\delta = 724.7$ ppm in CD_2Cl_2 ; Co-N-O = 122.9°) also exhibit large downfield shifted ^{15}N resonances.²¹

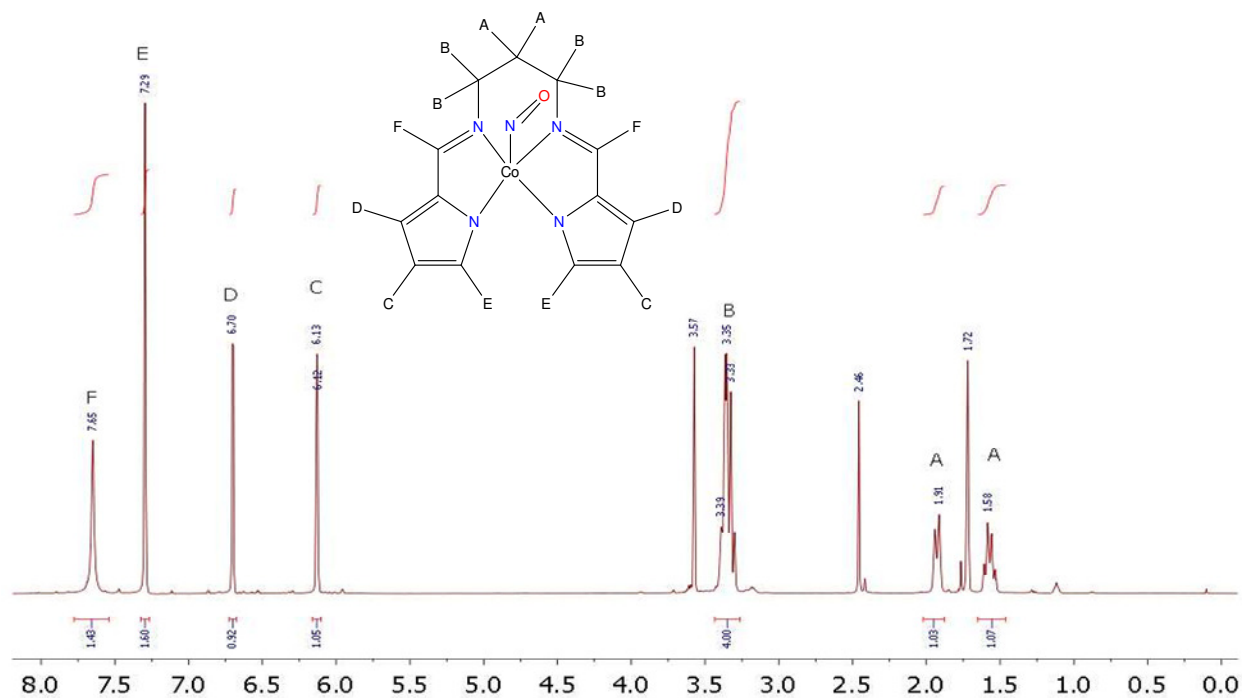


Figure 2.9. ^1H NMR spectrum of **1** in $\text{THF-}d_8$ at 298 K. The peak at 1.72 and 3.57 ppm is from residual protio solvent and the peak at 2.46 ppm is from trace H_2O .

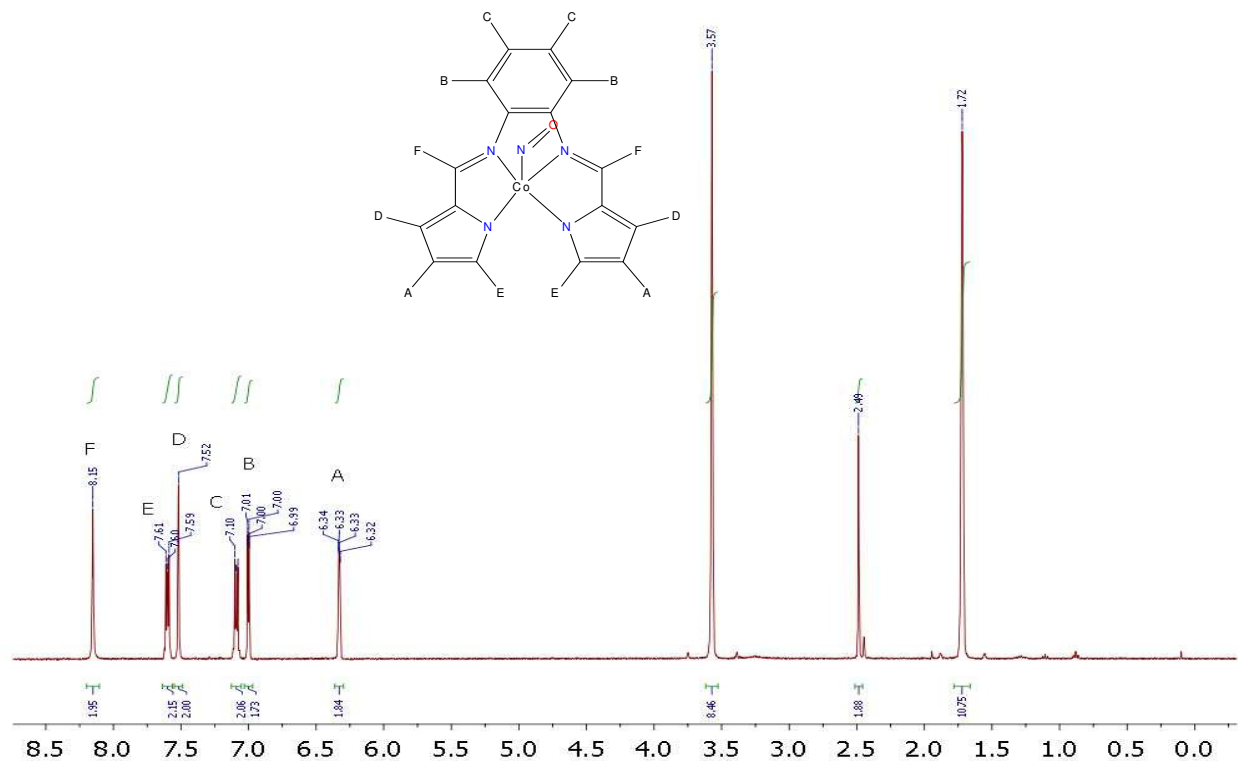


Figure 2.10. ^1H NMR spectrum of **2** in $\text{THF-}d_8$ at 298 K. The peak at 1.72 and 3.57 ppm is from residual protio solvent and the peak at 2.49 ppm is from trace H_2O .

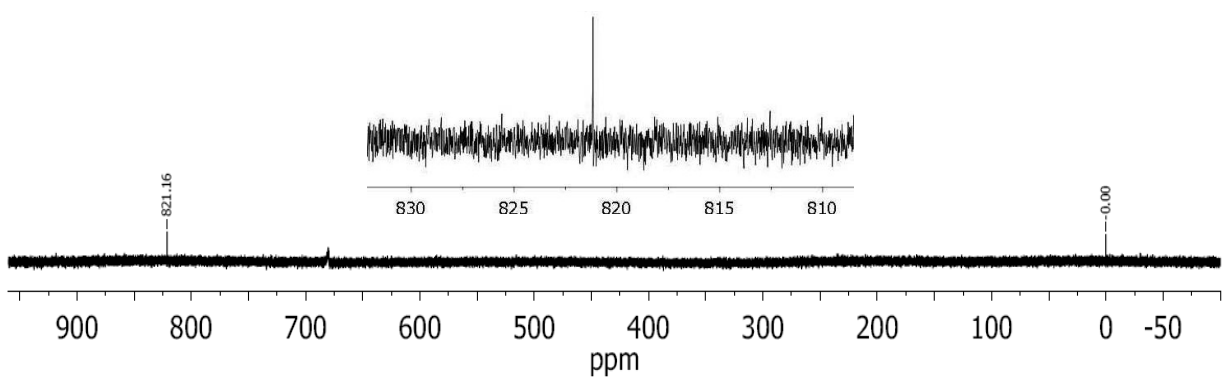


Figure 2.11. ^{15}N NMR spectrum of $(1\text{-}^{15}\text{NO})$ in $\text{THF-}d_8$ at 298 K (CH_3NO_2 used as external standard). Inset: expansion of the $^{15}\text{N} = 821$ ppm peak of the NO ligand.

Cyclic voltammetry (CV) and differential pulse voltammetry (DPV) were performed to assess the possible redox states that could be obtained with these systems. The electrochemistry was performed in MeCN at ambient temperature at a glassy carbon working electrode. Both **1** and **2** display a reversible redox event that we assign as the $\{\text{CoNO}\}^8/\{\text{CoNO}\}^9$ couple at $E_{1/2} = -1.40$ V and -1.34 V, respectively (versus Fc/Fc^+) (Figure 2.12). The CV of **2** also displays another species having a midpoint potential of -1.65 V that clearly shows up in the DPV (Figure 2.12). This peak could correspond to the $\{\text{CoNO}\}^9/\{\text{CoNO}\}^{10}$ couple although we have no other evidence for this assignment at present. These $E_{1/2}$ values are similar to the corresponding $\{\text{FeNO}\}^7/\{\text{FeNO}\}^8$ couple in the Fe analogs indicating the similarity in energies of the frontier MOs of the M-NO unit as a whole, even though electronically different by one electron. The reversible nature of the CV indicates that the $\{\text{CoNO}\}^9$ should be stable and isolable with these ligand frames. This electrochemical reduction has been observed in other cobalt nitrosyls,^{27,30} but no attempts to isolate the reduced $\{\text{CoNO}\}^9$ were made. The $\{\text{CoNO}\}^7/\{\text{CoNO}\}^8$ couple is not observed in **1** and **2** (MeCN, up to a potential of 1.60 V vs. Fc/Fc^+). A reversible $\{\text{CoNO}\}^8/\{\text{CoNO}\}^9$ couple has been assigned in a series of $\text{Co}(\text{N}_2\text{S}_2)$ complexes²⁷ (Table 2.1 compounds **4,5**) that also display $E_{1/2}$ values similar to their Fe analogues. It appears that the ancillary ligands do not affect the redox potential in these Co-NO and Fe-NO units.

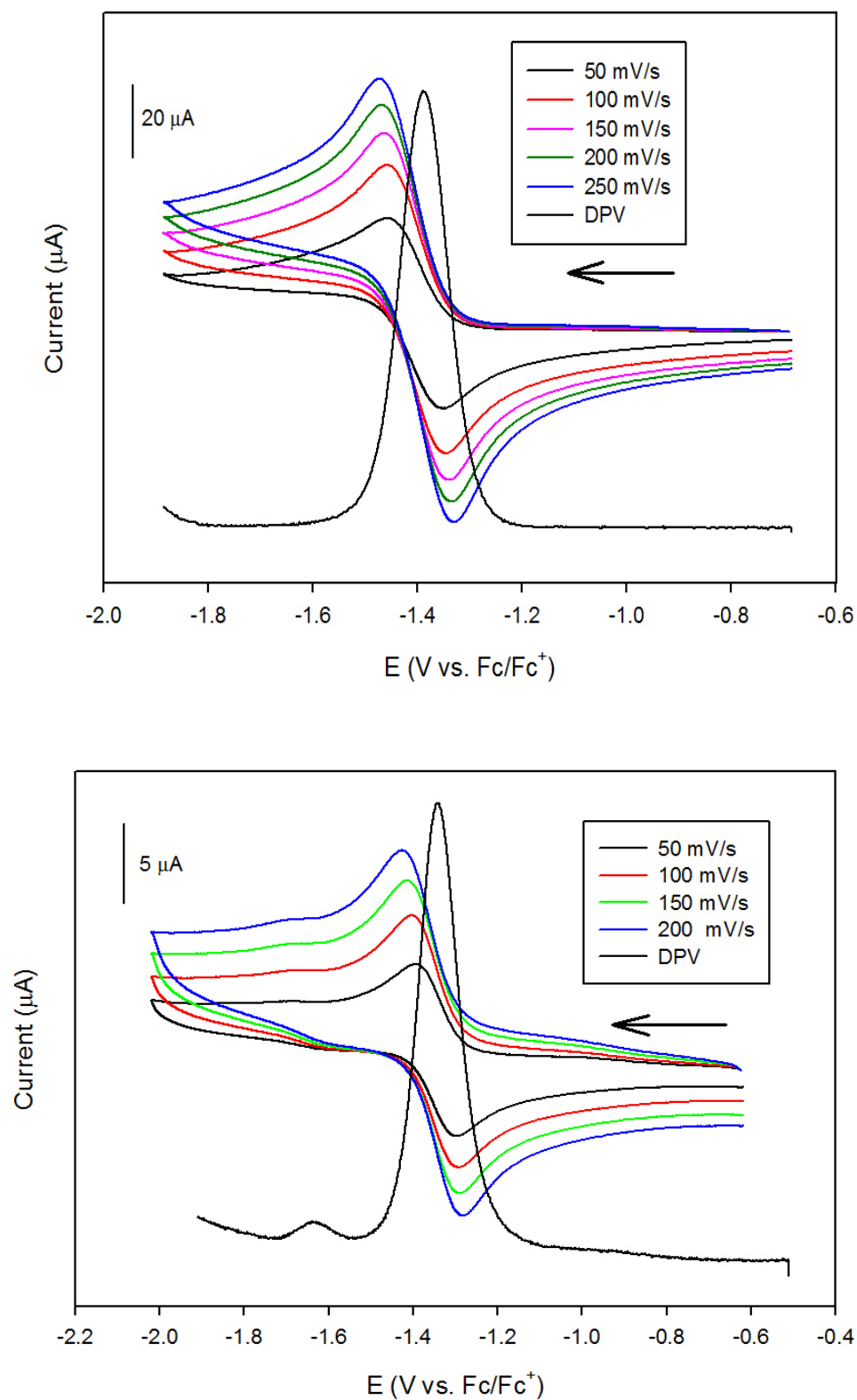


Figure 2.12. CVs and DPV of 2 mM MeCN solutions of **1** (top) and **2** (bottom) at different scan rates as indicated in the inset (0.1 M $n\text{-Bu}_4\text{NPF}_6$ supporting electrolyte, glassy carbon working electrode, Pt-wire counter electrode, RT). Arrow displays direction of scan.

2.2.4 Reactivity:

The principle goal of this research is to understand the structure, bonding, and reactive nature of reduced forms of NO when bound to metal centers and, in this case, Co. The reactivity of the present systems can thus be broken down into (i) reduction of the $\{\text{CoNO}\}^8$ systems **1** and **2** to the corresponding $\{\text{CoNO}\}^9$ derivatives **1^{red}** and **2^{red}**, and (ii) transfer of the bound NO in these $\{\text{CoNO}\}^{8/9}$ systems to potential biological targets like heme proteins.

(i) *Chemical reduction to form $\{\text{CoNO}\}^9$ derivatives **1^{red}** and **2^{red}**.* As mentioned earlier, electrochemical analysis of **1** and **2** show reversible CVs indicating the possibility of obtaining and exploring the properties of the unknown $\{\text{CoNO}\}^9$ species. The reduction of **1** and **2** was achieved by using a strong reducing agent, namely decamethylcobaltocene ($[\text{Co}(\text{Cp}^*)_2]$; $E_{1/2}$: -1.91 V vs Fc/Fc⁺ in MeCN). The reduction reaction was clean resulting in high (~90%) yields of the dark-red $\{\text{CoNO}\}^9$ complexes, $[\text{Co}(\text{Cp}^*)_2][\text{Co}(\text{LN}_4^{\text{Pr}})(\text{NO})]$ (**1^{red}**) and $[\text{Co}(\text{Cp}^*)_2][\text{Co}(\text{LN}_4^{\text{Ph}})(\text{NO})]$ (**2^{red}**). The reduction was confirmed via IR by comparing the shift in ν_{NO} from the corresponding $\{\text{CoNO}\}^8$ complexes: ν_{NO} for **1^{red}** = 1606 cm⁻¹ ($\Delta\nu_{\text{NO}}$ = 39 cm⁻¹), ν_{NO} for **2^{red}** = 1583 cm⁻¹ ($\Delta\nu_{\text{NO}}$ = 73 cm⁻¹) (Figure 2.13). The significant shift is consistent with one-electron reduction in the Co-NO unit as opposed to the ligand, however, the more dramatic shift in **2^{red}** is suggestive of a more NO-centered reduction.

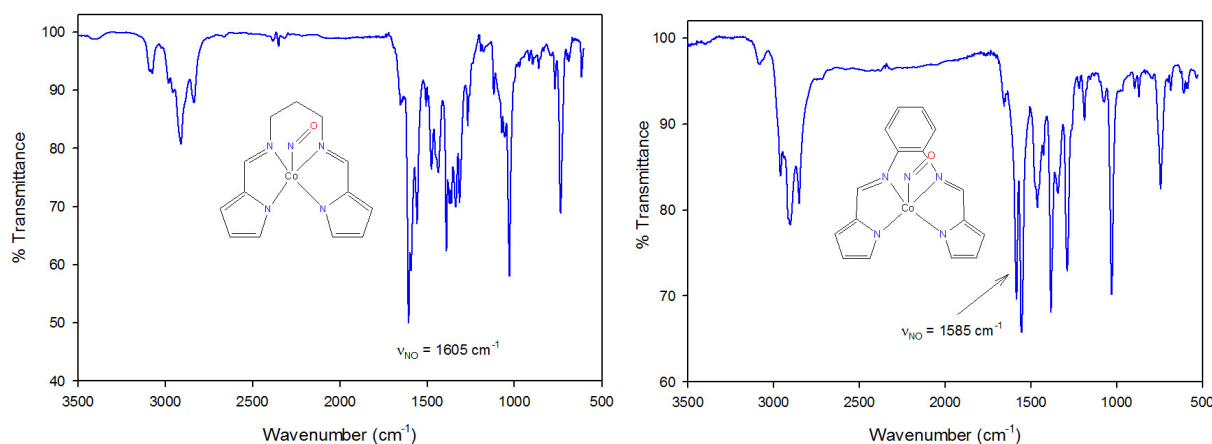


Figure 2.13. FTIR spectra of (**1**^{red}) (left) and (**2**^{red}) (right) in a KBr matrix.

Further evidence for the reduction of **1** and **2** came from EPR studies. Indeed, one expects that, upon reduction, the $S = 0$ nature of the precursor complexes will be lost resulting in an EPR-active $S = \frac{1}{2}$ species. Furthermore, if the reduction is Co-NO centered, then significant hyperfine coupling should be observed between the $I = 7/2$ Co nucleus and the $I = 1$ N nucleus of NO. Based on the $2nI + 1$ rule, 24 hyperfine lines would be expected barring overlap, which is usually not the case. The X-band EPR spectra of **1**^{red} and **2**^{red} in an MeCN/toluene (1:1) glass at 20 K are displayed in Figure 2.14. Both spectra are very similar and display split resonances centered near $g = 2$. Complex **2**^{red} has been fit to afford three separate g -values at 2.270, 2.140, and 2.085 (Figure 2.15). As expected, the hyperfine coupling from Co is larger than those from N; $A(\text{Co}) = 109, 35, 75$ G; $A(\text{N}) = 10, 85, 15$ G. To the best of our knowledge, these spectra are the only evidence for the existence of a $\{\text{CoNO}\}^9$ species. Furthermore, the superhyperfine indicate that the unpaired electron occupies a Co-NO-based MO as opposed to LN_4^{R} ligand-based MOs, which means the reduced nature of the NO can be explored (*vide infra*).

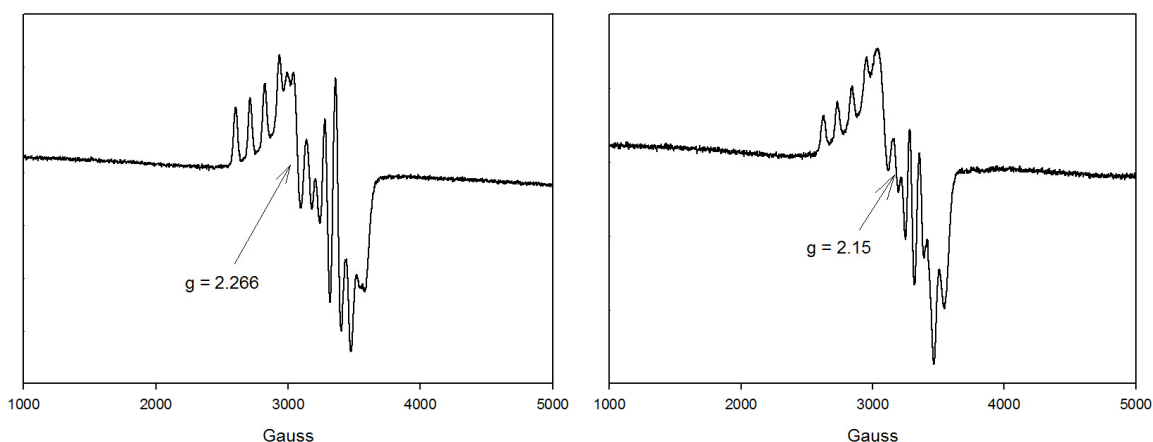


Figure 2.14. X-band EPR spectrum of **1^{red}** (left) and **2^{red}** (right) in MeCN/Toluene (1:1) at 20 K. Spectrometer settings: microwave frequency, 9.60 GHz; microwave power, 0.1 mW; modulation frequency, 100 kHz; modulation amplitude, 6.48 G.

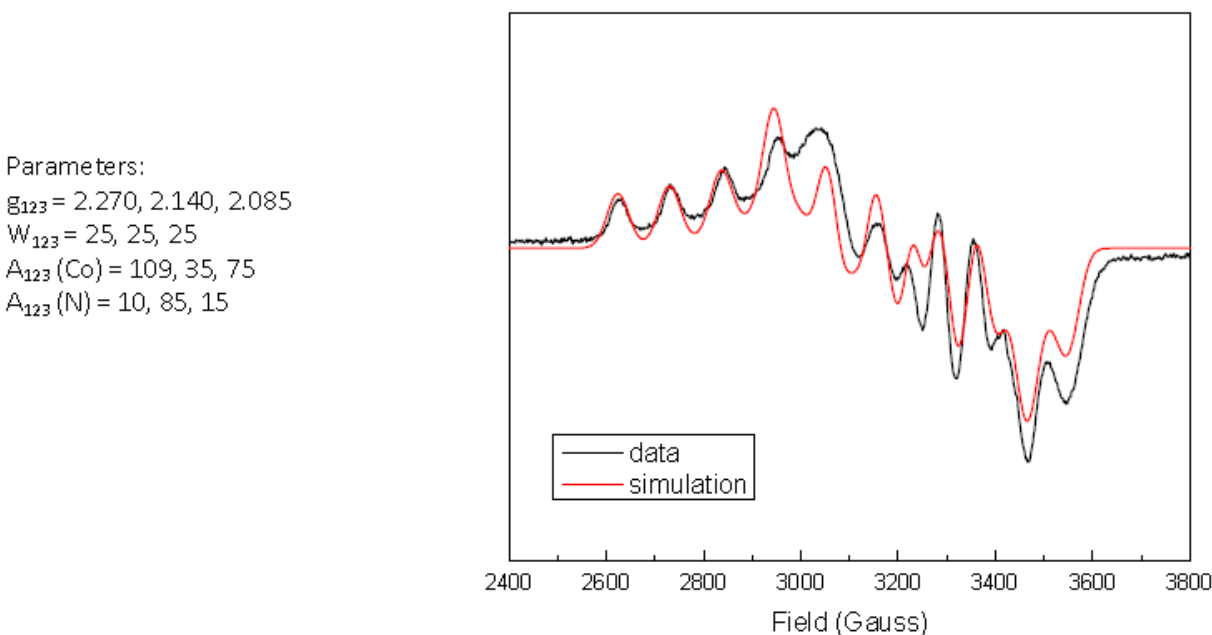
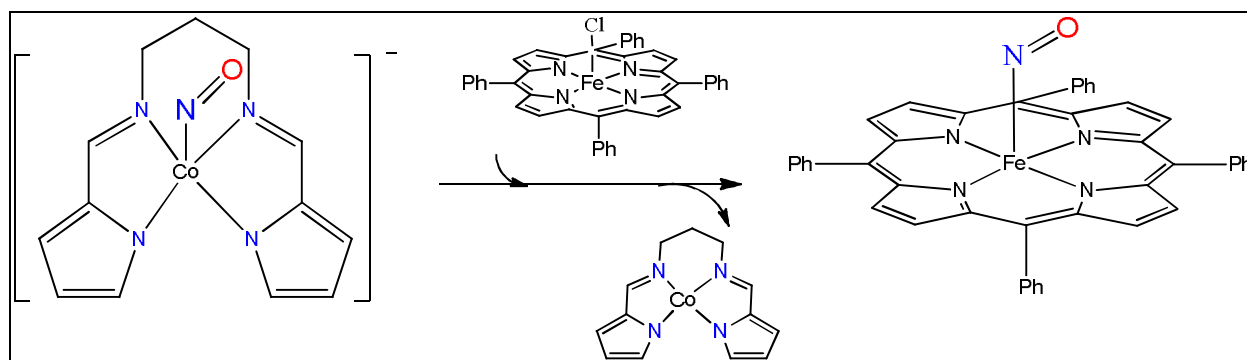


Figure 2.15. Simulation (red trace) of the X-band EPR spectrum of **2^{red}** (black trace). The 12 fitting parameters are noted on the left side.

(ii) *NO-transfer with $\{\text{CoNO}\}^{8/9}$ systems to heme analogues.* The utilization of the Co-NO complexes as NO-delivery agents (specifically NO^-) was explored with Fe(III)-porphyrin complexes with heme analogues such as $[\text{Fe}(\text{TPP})\text{Cl}]$. This heme analogue is known to react with NO^- to form $[\text{Fe}(\text{TPP})(\text{NO})]$ (an $\{\text{FeNO}\}^7$ complex) via a reductive nitrosylation pathway

in organic solvents like THF (Scheme 2.2). Reaction of a 1:1 mixture of **1** with [Fe(TPP)Cl] in THF resulted in no reaction over 1 h at temperatures of 25 and 37 °C. Thus, the {CoNO}⁸ complexes are inert towards reductive nitrosylation under these conditions. When the analogous reaction with a **1**^{red}/[Fe(TPP)Cl] (1:1.2) was performed, the resultant UV-vis spectrum changed instantly (Figure 2.16). The [Fe(TPP)Cl] Soret band at 410 nm initially red-shifts to 425 nm consistent with the formation of [Fe^{II}(TPP)Cl] via one-electron reduction.³¹ Over a period of 60 min, this band shifts progressively to 409 nm, which overlaps with the starting [Fe^{III}(TPP)Cl] complex (Figure 2.16). It is possible that the reductive nitrosylation could occur through a two-step process where reduction of the Fe(III) to Fe(II) occurs first and then neutral NO• is transferred to form the {FeNO}⁷ porphyrin complex. This mechanism appears to occur in the {FeNO}⁸ analogue with LN₄^{pr}.³² Unfortunately, there was no indication that the NO from **1**^{red} is transferred to the [Fe(TPP)Cl]. It thus appears that the {CoNO}⁹ complexes may reduce ferric hemes but not transfer over the NO ligand.



Scheme 2.2. Proposed reaction of [Fe(TPP)Cl] with **1**^{red} in THF.

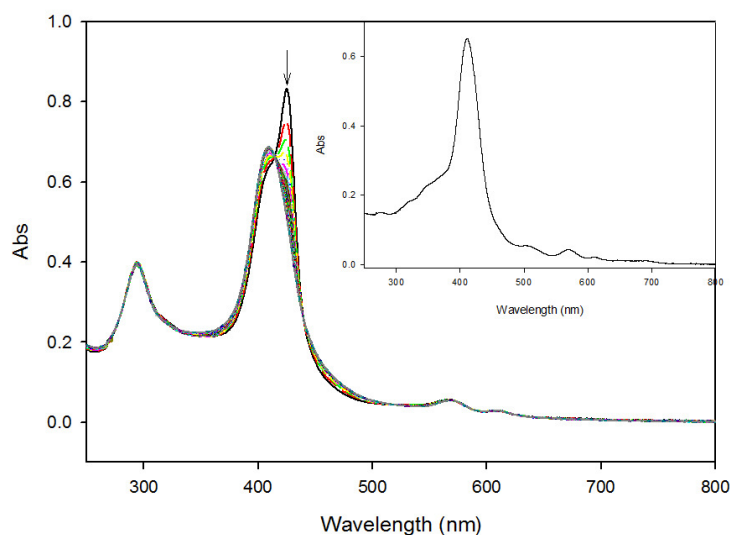


Figure 2.16. UV-vis spectral monitoring of the reaction of a 5 μM THF solution of $[\text{Fe}(\text{TPP})\text{Cl}]$ with $\mathbf{1}^{\text{red}}$ (1:1.2) in THF at 298 K (each trace recorded at 1 min intervals, 60 min total time). Inset: UV-vis of starting $[\text{Fe}^{\text{III}}(\text{TPP})\text{Cl}]$ complex in THF at 298 K, λ_{max} 410 nm.

2.3 Conclusion

In summary, this work describes the synthesis, characterization, and reactivity of $\{\text{CoNO}\}^{8/9}$ nitrosyls containing an N_4 planar di-imine/di-pyrrolide ligand. X-ray structural characterization of the $\{\text{CoNO}\}^8$ complexes **1** and **2** reveal square-pyramidal Co centers containing an axial NO ligand that is severely bent and consistent with a reduced NO ligand. FTIR, ^1H NMR, and electrochemical measurements were also made that aided in the elucidation of the electronic structure of these systems. More specifically, electrochemical studies indicated that these ligand platforms will support reduction at the Co-NO unit to form unprecedented $\{\text{CoNO}\}^9$ type of systems. We have synthesized and characterized the $\{\text{CoNO}\}^9$ systems with FTIR and EPR spectroscopies that confirm the reduction is largely Co-NO-based. We envision that the $\{\text{CoNO}\}^9$ systems like $\mathbf{1}^{\text{red}}$ and $\mathbf{2}^{\text{red}}$ should serve as excellent NO^- donor systems for HNO/ NO^- therapy and are in the process of exploring and understanding its reactivity with heme analogues and heme proteins.

2.4 Experimental Details:

2.4.1. General Information. The materials and physical methods utilized were similar to that reported in Chapter 1.

2.4.2. Synthesis of LN_4^{Pr} . A batch of 1.442 g (19.45 mmol) of 1,3 diaminopropane (dissolved in 2 mL of MeCN) to 3.692 (38.82 mmol) of pyrrole-2-carboxaldehyde dissolved in 6 mL of MeCN. To the resultant reaction solution, freshly charged 4 Å sieves (15% w/v) were added under N_2 atmosphere. No color change was observed. The reaction mixture was heated at 40 °C for 2 h when a white precipitate was observed. The reaction was stirred for another 2 h at RT. The insolubles were filtered and washed with MeCN. The precipitate was then dissolved in CH_2Cl_2 and filtered to separate sieves. The resultant CH_2Cl_2 solution was concentrated by rotovap to afford a white powder (3.209 g, 14.06 mmol, 72%). mp: 118-120 °C. ^1H NMR (400 MHz, CDCl_3 , δ from TMS): 8.02 (s, 1H, $\text{CH}=\text{N}$), 6.84 (s, 1H, Ar-*H*), 6.45 (d, 1H, Ar-*H*), 6.21 (t, 1H, Ar-*H*), 3.59 (t, 2H, $\text{CH}=\text{N}-\text{CH}_2$), 1.95 (p, 1H, $\text{CH}_2-\text{CH}_2-\text{CH}_2$). ^{13}C NMR (100.6 MHz, CDCl_3 , δ from TMS): 152.10 ($\text{CH}=\text{N}$), 130.48 (Ar-*C*), 121.99 (Ar-*C*), 114.22 (Ar-*C*), 109.89 (Ar-*C*), 58.54 ($\text{CH}=\text{N}-\text{CH}_2$), 32.75 ($\text{CH}_2-\text{CH}_2-\text{CH}_2$). FTIR (ATR-diamond, solid), ν_{max} (cm^{-1}): 3111 (w), 3046 (w), 2941 (m), 2847 (m), 2746 (w), 1634 (vs, $\text{C}=\text{N}$), 1440 (w), 1418 (m), 1360 (w), 1340 (w), 1313 (w), 1246 (w), 1136 (w), 1125 (w), 1096 (w), 1062 (m), 1033 (m), 1024 (m), 988 (m), 968 (w), 959 (w), 919 (w), 881 (m), 789 (m), 743 (s), 656 (w), 607 (m). LRMS-ESI (m/z): $[\text{M} + \text{H}]^+$ calcd for $\text{C}_{13}\text{H}_{17}\text{N}_4$, 229.2; found, 229.0.

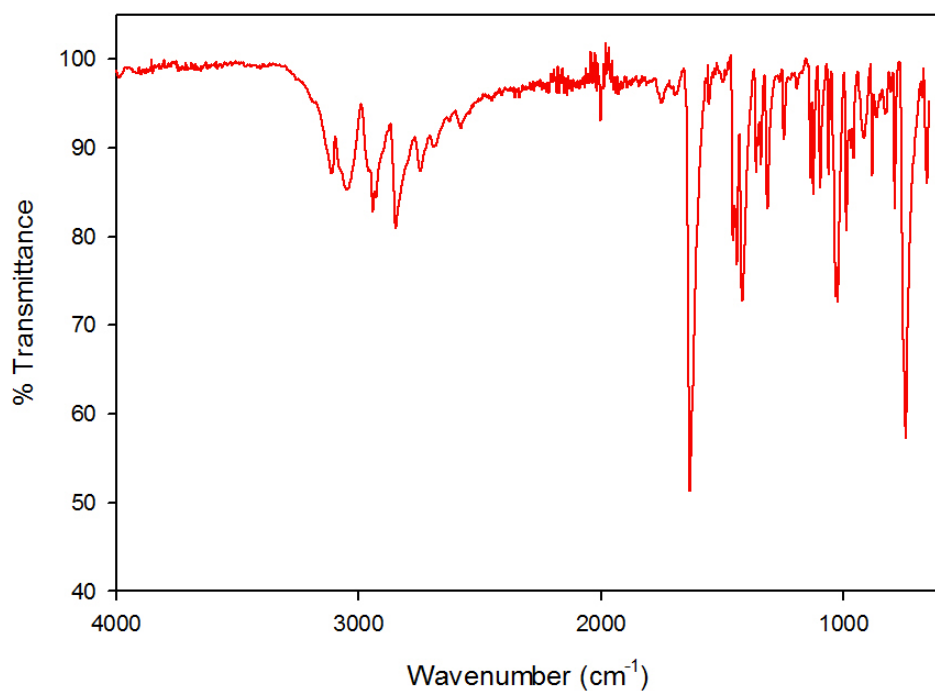


Figure 2.17. FTIR spectrum of LN_4^{Pr} (ATR-diamond, solid).

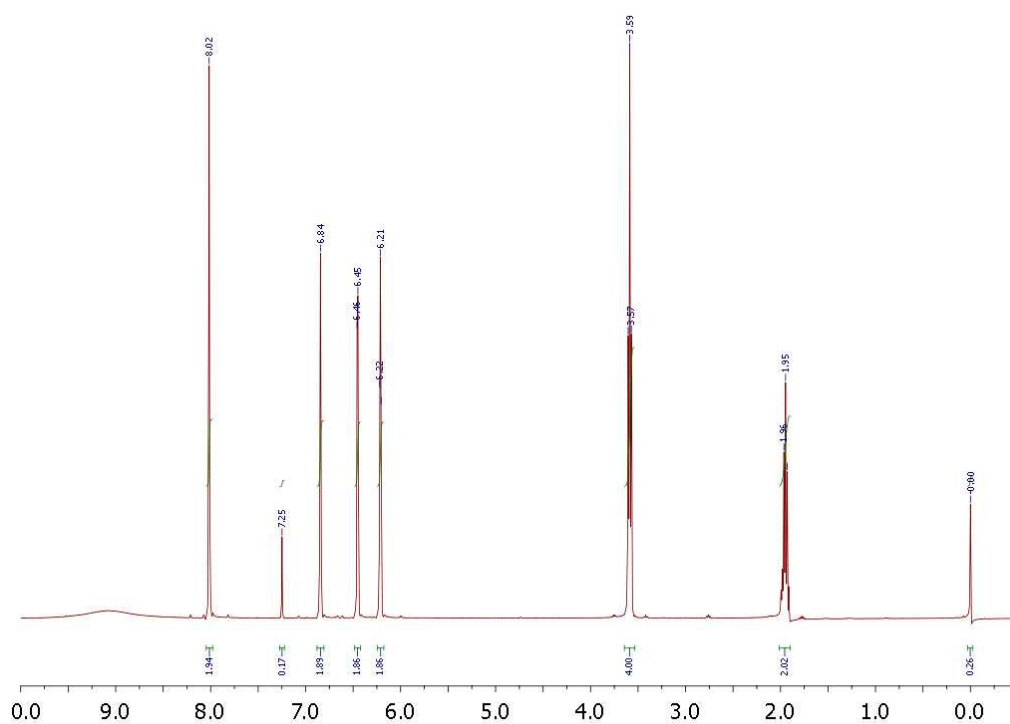


Figure 2.18. ^1H NMR spectrum of LN_4^{Pr} in CDCl_3 (0.05% v/v TMS) at 298 K. The peak at 7.27 is from residual protio solvent.

2.4.3. Synthesis of LN_4^{ph} . The synthesis was performed according to a previously published results.³³ ^1H NMR (400 MHz, CDCl_3 , δ from TMS): 12.33 (s, 2H, NH), 7.68 (s, 2H, $\text{CH}=\text{N}$), 7.25 (t, 2H, Ar-H), 7.07 (q, 2H, Ar-H), 6.40 (d, 2H, Ar-H), 6.23 (s, 2H, Ar-H), 6.01 (t, 2H, Ar-H). ^{13}C NMR (100.6 MHz, CDCl_3 , δ from TMS): 150.6 ($\text{CH}=\text{N}$), 145.7 (Ar-C), 130.8 (Ar-C), 126.6 (Ar-C), 123.8 (Ar-C), 119.0 (Ar-C), 117.2 (Ar-C), 109.6 (Ar-C). FTIR (ATR-diamond, solid), ν_{max} (cm^{-1}): 3115 (w), 2964 (w, br), 1613 (vs, $\text{C}=\text{N}$), 1572 (s), 1440 (w), 1410 (m), 1335 (w), 1309 (w), 1246 (w), 1211 (w), 1133 (w), 1092 (m), 1036 (s), 1024 (s), 964 (w), 876 (m), 839 (m), 783 (w), 738 (s), 657 (w), 606 (m), 579 (w), 549 (m), 490 (w), 482 (w), 472 (w), 403 (w).

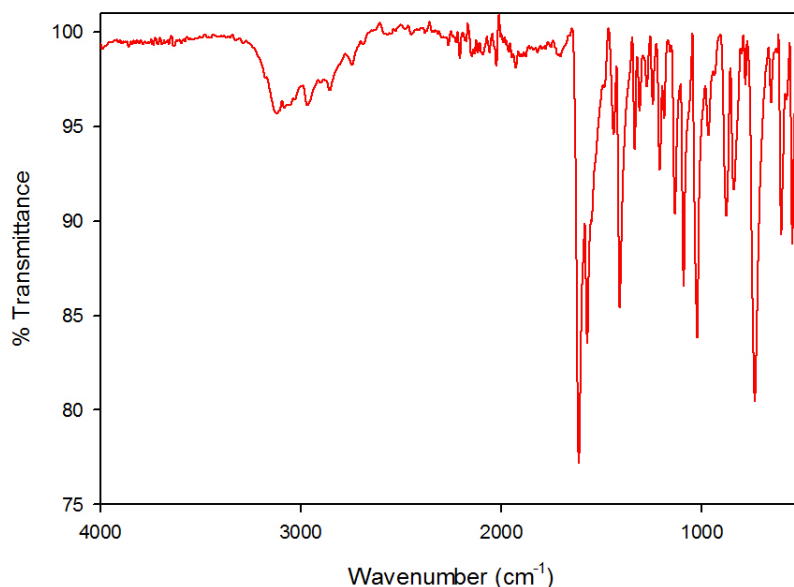


Figure 2.19. FTIR spectrum of LN_4^{ph} (ATR-diamond, solid).

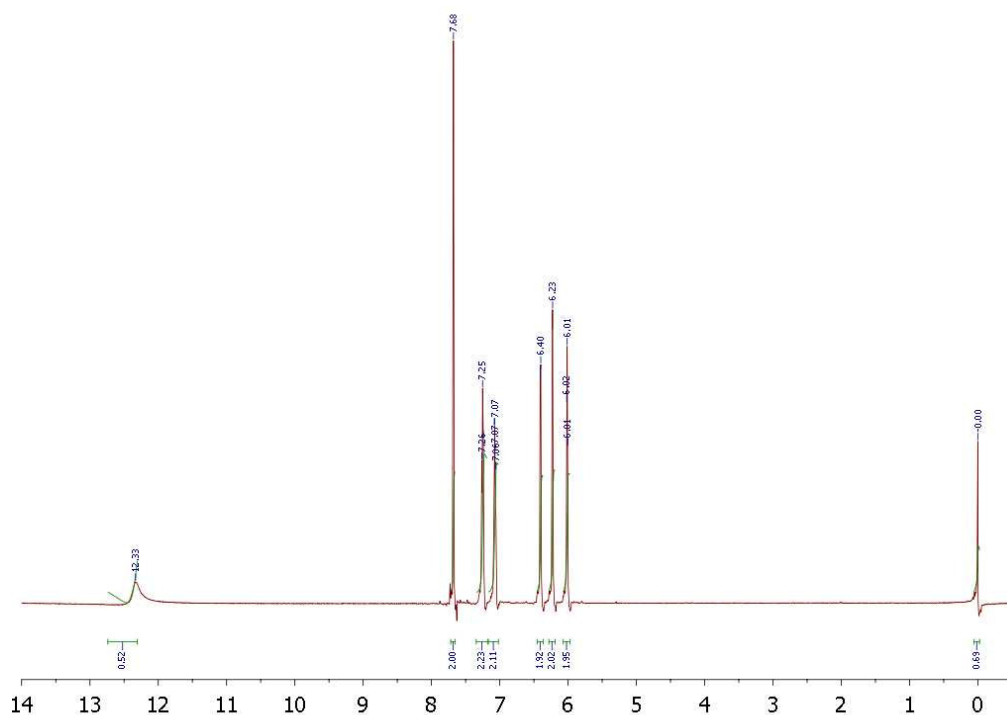


Figure 2.20. ^1H NMR spectrum of LN_4^{Ph} in CDCl_3 (0.05% v/v TMS) at 298 K. The peak at 7.25 is from residual protio solvent.

2.4.4. Synthesis of $[\text{Co}(\text{LN}_4^{\text{Pr}})(\text{NO})]$ (1). To a batch of LN_4 (0.1069 g, 0.4683 mmol) dispersed in 3 mL of dry MeCN was added a 2 mL MeCN slurry of NaH (0.0224 g, 0.9333 mmol), which resulted in $\text{H}_2(\text{g})$ evolution and the light purple solution color of the deprotonated ligand. To ensure complete deprotonation, an occasional vacuum was applied while stirring the solution further for ~15 min. To this solution was then added a 5 mL MeCN solution of $(\text{Et}_4\text{N})_2[\text{CoCl}_4]^{34}$ (0.2119 g, 0.4594 mmol) resulting in formation of a white precipitate (NaCl) and a green-red solution. The reaction mixture was stirred for another 1 h at 40 °C, which resulted in no further change. Finally, the solution was filtered to remove NaCl to obtain a clear green-red filtrate, which was concentrated to ~5 mL. To the filtrate was then purged a stream of purified $\text{NO}(\text{g})$ for 1.5 min at RT under dark conditions resulting in a gradual solution color

change to dark red-brown upon NO(g) introduction. The resulting homogeneous solution was then stirred for 30 min at RT under an atmosphere of NO(g) in the headspace of the flask. After this time, excess NO(g) was removed by pulling vacuum, refilled with N₂, and the solution was brought into the glovebox. Next, the solvent was stripped to dryness and ~10 mL of THF was added resulting in a dark-red solution with some pale precipitate (Et₄NCl). The THF solution was filtered and stripped to dryness to afford 0.1083 g (0.3436 mmol, 75%) of a dark colored microcrystalline product. Red X-ray quality crystals of **1** were grown by slow diffusion of Et₂O into a THF solution of the complex at -20 °C. FTIR (KBr matrix), ν_{max} (cm⁻¹): 3086 (w), 2922 (w), 2901 (w), 2846 (w), 1645 (vs, NO), 1595 (s), 1577 (s), 1439 (m), 1394 (m), 1364 (m), 1333 (m), 1317 (m), 1309 (m), 1273 (w), 1251 (m), 1234 (w), 1192 (w), 1180 (w), 1115 (m), 1099 (w), 1082 (m), 1035 (s), 954 (w), 929 (w), 898 (w), 880 (w), 858 (w), 804 (w), 771 (m), 740 (s), 725 (s), 678 (w), 609 (m), 571 (w), 544 (w), 481 (m), 440 (w), 422 (w). ν_{NO} (solution-state, CaF₂ windows, 0.1 mm spacers, RT): 1665 (MeCN); 1662 (THF); 1666 (CH₂Cl₂). UV-vis (MeCN, 298 K), λ_{max} , nm (ϵ , M⁻¹ cm⁻¹): 298 (12,700); 363 (sh 6,200); 520 (sh, 630). E_{1/2} (vs. Fc/Fc⁺, MeCN, RT): -1.40 V. ¹H NMR (500 MHz, THF-d₈, δ from protio solvent): 7.65 (s, 2H, CH=N), 7.29 (s, 2H, Ar-H), 6.70 (d, 2H, Ar-H), 6.13 (t, 2H, Ar-H), 3.35 (m, 4H, CH=N-CH₂), 1.91 (m, 1H, CH₂-C(H)(H)-CH₂), 1.58 (m, 1H, CH₂-C(H)(H)CH₂). Anal. Calcd for C₁₃H₁₄N₅OC_o: C, 49.53; H, 4.48; N, 22.22. Found: C, 49.73; H, 4.47; N, 21.67.

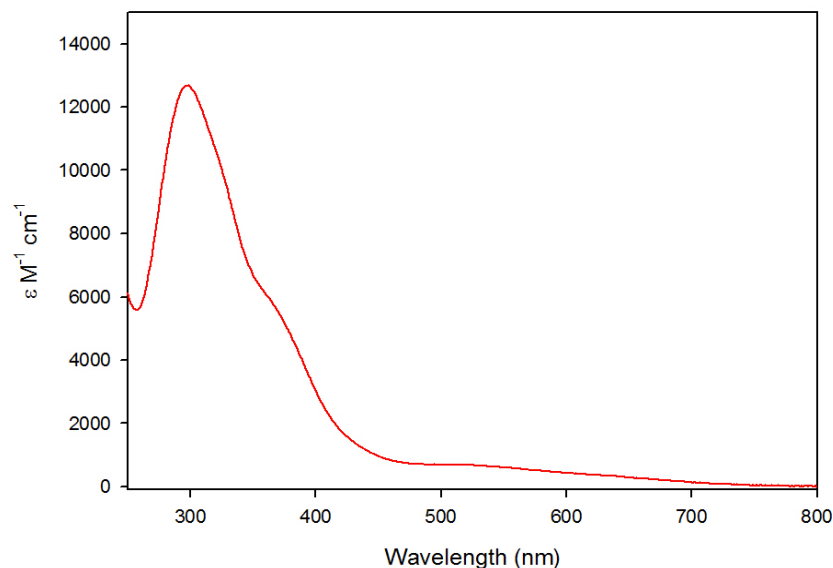


Figure 2.21. UV-vis spectrum of a 66.0 μM solution of **1** in MeCN at 298 K.

2.4.5. Synthesis of $[\text{Co}(\text{LN}_4^{\text{pr}})(^{15}\text{NO})]$ (1- ^{15}NO**).** The isotopically-labeled complex **1- ^{15}NO** was prepared analogously to **1** except for using 0.2028 g (0.4397 mmol) of $(\text{Et}_4\text{N})_2[\text{CoCl}_4]$, 0.1003 g (0.4394 mmol) of LN_4^{pr} , and 0.0214 g (0.8917 mmol) of NaH to generate $(\text{Et}_4\text{N})_2[\text{Co}(\text{LN}_4)\text{Cl}_2]$ *in situ* followed by purging $^{15}\text{NO}(\text{g})$. Yield: 0.070 g (0.221 mmol, 50%). FTIR, ν_{NO} (cm^{-1}): 1617 (KBr matrix); 1636 (MeCN); 1633 (THF); 1639 (CH_2Cl_2). ^{15}N NMR (500 MHz, THF-d_8 , δ from CH_3NO_2): 821.

2.4.6. Synthesis of $[\text{Co}(\text{LN}_4^{\text{ph}})(\text{NO})]$ (2**).** To a batch of LN_4^{ph} (0.2823 g, 1.08 mmol) dispersed in 5 mL of dry MeCN was added a 2 mL MeCN slurry of NaH (0.0592 g, 2.46 mmol), which resulted in $\text{H}_2(\text{g})$ evolution and the solution color of the deprotonated ligand became canary yellow. To ensure complete deprotonation, an occasional vacuum was applied while stirring the solution further for ~15 min. To this solution was then added a 5 mL MeCN solution of $(\text{Et}_4\text{N})_2[\text{CoCl}_4]$ (0.4959 g, 1.07 mmol) resulting in formation of a white precipitate (NaCl) and a dark-red solution. The reaction mixture was stirred for another 12 h at 40 $^\circ\text{C}$, which resulted in

no further change. Finally, the solution was filtered to remove NaCl to obtain a clear red filtrate, which was concentrated to dryness to yield 0.5560 g of red crystalline solid of $(\text{Et}_4\text{N})_2[\text{Co}(\text{LN}_4^{\text{ph}})\text{Cl}_2]$. A portion of this solid (0.2910 g, 0.447 mmol) was dissolved in 5 mL of MeCN and was then purged with a stream of purified NO(g) for 1.5 min at RT under dark conditions resulting in a gradual solution color change to dark red-brown upon NO(g) introduction, which ultimately forms dark red microcrystalline precipitate. The resulting solution was then stirred for 30 min at RT under an atmosphere of NO(g) in the headspace of the flask. After this time, excess NO(g) was removed by pulling vacuum and refilling with N₂ and the solution was brought into the glovebox. The microcrystalline precipitate (0.0280 g) was filtered and dried over vacuum. Next, the filtrate solvent was stripped to dryness and ~10 mL of THF was added resulting in a dark-red solution with some pale precipitate (Et₄NCl). The THF solution was filtered and stripped to dryness to afford 0.0533 g of a dark colored microcrystalline product (Total yield = 0.0813 g, 0.233 mmol, 52%). Red X-ray quality crystals of **2** were grown by slow diffusion of Et₂O into a THF solution of the complex at -20 °C. FTIR (KBr matrix), ν_{max} (cm⁻¹): 1656 (vs, NO), 1582 (w), 1552 (s), 1460 (w), 1445 (w), 1380 (s), 1325 (w), 1295 (s), 1257 (m), 1196 (w), 1034 (s), 985 (w), 895 (m), 741 (s), 677 (w), 603 (m), 428 (w). UV-vis (MeCN, 298 K), λ_{max} , nm (ϵ , M⁻¹ cm⁻¹): 315 (17,500), 361 (21,500), 448 (10,500). E_{1/2} (vs. Fc/Fc⁺, MeCN, RT): -1.34 V. ¹H NMR (500 MHz, THF-d₈, δ from protio solvent): 8.15 (s, 2H, CH=N), 7.60 (q, 2H, Ar-H), 7.52 (s, 2H, Ar-H), 7.10 (q, 2H, Ar-H), 7.00 (d, 2H, Ar-H), 6.33 (d, 2H, Ar-H).

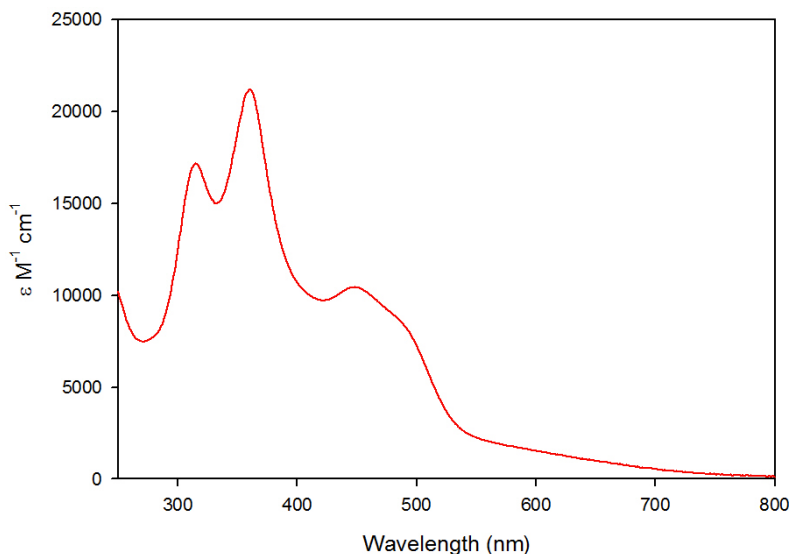


Figure 2.22. UV-vis spectrum of a 42 μM solution of **2** in MeCN at 298 K.

2.4.7. Synthesis of $[\text{Co}(\text{LN}_4^{\text{ph}})(^{15}\text{NO})]$ (2- ^{15}NO**).** The isotopically-labeled complex **2- ^{15}NO** was prepared analogously to **2** except for using 0.2150 g (0.466 mmol) of $(\text{Et}_4\text{N})_2[\text{CoCl}_4]$, 0.1236 g (0.471 mmol) of LN_4^{ph} , and 0.0226 g (0.941 mmol) of NaH to generate $(\text{Et}_4\text{N})_2[\text{Co}(\text{LN}_4)\text{Cl}_2]$ *in situ* followed by purging $^{15}\text{NO}(\text{g})$. Yield: 0.074 g (0.211 mmol, 45%). FTIR, ν_{NO} (cm^{-1}) 1629 (KBr matrix)

2.4.8. Synthesis of $[\text{Co}(\text{Cp}^*)_2][\text{Co}(\text{LN}_4^{\text{pr}})(\text{NO})]$ (1 $^{\text{red}}$**).** To a 4 mL THF solution of $[\text{Co}(\text{LN}_4^{\text{pr}})(\text{NO})]$ (0.0618 g, 0.1960 mmol) was added a 5 mL toluene solution of $[\text{Co}(\text{Cp}^*)_2]$ (0.0645 g, 0.1958 mmol). The resultant solution formed a brown precipitate. The solution was stirred for 30 min at RT and filtered. The precipitate was washed with 2 mL cold toluene followed by 2 mL of cold diethyl ether and dried under vacuum to get 0.1048 g of brown product (0.1625 mmol, 83%). FTIR (KBr matrix), ν_{max} (cm^{-1}): 3073 (w), 2909 (m), 2835 (w), 1606 (s, NO), 1592 (s), 1557 (m), 1506 (w), 1474 (m), 1436 (m), 1389 (s), 1372 (m), 1361 (m), 1336 (m), 1314 (m), 1267 (w), 1118 (w), 1072 (w), 1055 (w), 1028 (s), 861 (w), 768 (w), 735 (m), 689 (w), 616 (w), 530 (w), 445 (w).

2.4.9. Synthesis of [Co(Cp*)₂][Co(LN₄^{ph})(NO)] (2^{red}). To a 2 mL THF solution of [Co(LN₄^{ph})(NO)] (0.0236 g, 0.068 mmol) was added a 2 mL toluene solution of [Co(Cp*)₂] (0.0223 g, 0.068 mmol) at RT. The solution color changed from red to red-brown. The solution was stirred for further 45 min at RT. After that the solvent was evacuated to dryness. The residue was washed with 2 mL toluene and 2 mL pentane and dried under vacuum (0.0429 g, 94 %). FTIR (KBr matrix), ν_{max} (cm⁻¹): 2959 (m), 2902 (m), 2849 (m), 1655 (w), 1583 (s, NO), 1553 (s), 1460 (m), 1382 (s), 1341 (s), 1287 (s), 1186 (w), 1071 (w), 1028 (s), 869 (w), 742 (m), 607 (w), 445 (w).

2.4.10. Reaction of **1 with [Fe(TPP)Cl].** The reaction of **1** with [Fe(TPP)Cl] was monitored by electronic absorption spectroscopy under anaerobic conditions in THF at 298 and 310 K. For both the runs a 10 μ L THF aliquot of **1** (10 mM, 5 mol-equiv) was added via a microsyringe to a quartz UV-vis cell containing [Fe(TPP)Cl] (6.6 μ M, 3.01 mL total volume). The reaction was monitored for 120 min. No change was observed for band at λ_{max} : 410 nm.

2.4.11. Reaction of **1^{red} with [Fe(TPP)Cl].** The reaction of **1**^{red} with [Fe(TPP)Cl] was monitored by electronic absorption spectroscopy under anaerobic conditions in THF at 298. A 6 μ L THF aliquot of **1**^{red} (2 mM, 1.2 mol-equiv) was added via a microsyringe to a quartz UV-vis cell containing [Fe(TPP)Cl] (4.99 μ M, 2 mL total volume). The reaction was monitored for 60 min. An instantaneous change from λ_{max} at 410 nm to 425 nm was observed, after which the band at 425 nm gradually shifts over 60 min to 410 nm.

Table 2.4. X-ray Parameters for **1** and **2**.

Parameters	1	2
Formula	C ₁₃ H ₁₄ CoN ₅ O	C ₁₆ H ₁₂ CoN ₅ O
Formula weight	315.22	349.23
Crystal system	Monoclinic	Triclinic
Space group	<i>P</i> 2 ₁ / <i>n</i>	<i>P</i> $\bar{1}$
Crystal color, habit	red rectangle	red rectangle
<i>a</i> , Å	10.445(5)	8.7601(12)
<i>b</i> , Å	11.723(5)	9.2993(13)
<i>c</i> , Å	11.030(5)	35.915(5)
α , deg	90.00	96.415(2)
β , deg	100.177(5)	95.892(2)
γ , deg	90.00	98.484(2)
<i>V</i> , Å ³	1329.3(10)	2854.4(7)
<i>Z</i>	4	2
ρ_{calcd} , g/cm ⁻³	1.575	1.149
<i>T</i> , K	100(2)	100(2)
abs coeff, μ , mm ⁻¹	1.293	0.627
θ limits, deg	2.48-33.20	2.23-32.03
total no. of data	22837	49802
no. of unique data	4896	19617
no. of parameters	181	802
GOF on <i>F</i> ²	1.166	1.121
<i>R</i> ₁ , ^[a] %	2.43	5.14
<i>wR</i> ₂ , ^[b] %	7.56	12.09
max, min peaks, e/Å ³	0.511, -0.941	1.964, -0.873

$$^a R_1 = \Sigma | |F_o| - |F_c| | / \Sigma |F_o| ; ^b wR_2 = \{ \Sigma [w(F_o^2 - F_c^2)^2] / \Sigma [w(F_o^2)] \}^{1/2}.$$

References

1. Ignarro, L. J.; Buga, G. M.; Wood, K. S.; Byrns, R. E.; Chaudhuri, G. *Proc. Natl. Acad. Sci. USA* **1987**, *84*, 9265.
2. Poulos, T. L. *Curr. Opin. Struct. Biol.* **2006**, *16*, 736.
3. Fukuto, J. M.; Dutton, A. S.; Houk, K. N. *ChemBioChem* **2005**, *6*, 612.
4. Averill, B. A. *Chem. Rev.* **1996**, *96*, 2951.
5. Paolocci, N.; Jackson, M. I.; Lopez, B. E.; Miranda, K.; Tocchetti, C. G.; Wink, D. A.; Hobbs, A. J.; Fukuto, J. M. *Pharmacol. Ther.* **2007**, *113*, 442.
6. Garthwaite, J.; Boulton, C. L. *Annu. Rev. Physiol.* **1995**, *57*, 683.
7. Richter-Addo, G. B.; Legzdins, P. *Metal Nitrosyls*, Oxford University Press: New York, **1992**.
8. Jones, K.; *Comprehensive Inorganic Chemistry*; Pergamon: Oxford, **1973**, Vol.2, Chapter 19.
9. Siegel, M. W.; Celotta, R. J.; Hall J. L.; Levine, J.; Bennett, R. A. *Phys. Rev. A* **1972**, *6*, 607.
10. Teillet-Billy, D.; Fiquet-Fayard, F. *J. Phys.* **1977**, *10B*, L111.
11. Conradie, J.; Quarless, D. A., Jr.; Hsu, H.-F.; Harrop, T. C.; Lippard, S. J.; Koch, S. A.; Ghosh, A. *J. Am. Chem. Soc.* **2007**, *129*, 10446.
12. Enemark, J. H.; Feltham, R. D. *Coord. Chem. Rev.* **1974**, *13*, 339.
13. Feltham, R. D.; Enemark, J. H. *Top. Stereochem.* **1981**, *12*, 155.
14. Scheidt, W. R.; Ellison, M. K., *Acc. Chem. Res.* **1999**, *32*, 350.
15. Dahl, L. F.; de Gil, E. R.; Feltham, R. D. *J. Am. Chem. Soc.* **1969**, *91*, 1653.
16. Farmer, P. J.; Sulc, F. *J. Inorg. Biochem.* **2005**, *99*, 166.

17. Stamler, J. S.; Singel, D. J.; Loscalzo, J. *Science* **1992**, 258, 1898.
18. Hughes, M. N. *Biochim. Biophys. Acta* **1999**, 1411, 263.
19. Turk, T.; Hollocher, T. C. *Biochem. Biophys. Res. Commun.* **1992**, 183, 983.
20. Scheidt, W. R.; Hoard, J. L. *J. Am. Chem. Soc.* **1973**, 95, 8281.
21. Patra, A. K.; Dube, K. S.; Sanders, B. C.; Papaefthymiou, G. C.; Conradie, J.; Ghosh, A.; Harrop, T. C. *J. Am. Chem. Soc.* (to be submitted)
22. McCleverty, J. A. *Chem. Rev.* **2004**, 104, 403.
23. Sharma, V. S.; Pilz, B. R.; Boss, G. R.; Magde, D. *Biochemistry*, **2003**, 42, 8900.
24. Danishpajooh, I. O.; Gudi, T.; Chen, Y.; Kharitonov V. G.; Sharma, V. S.; Boss, G. S., *J. Biol. Chem.* **2001**, 276, 27329.
25. Broderick, K. E.; Alvarez, L.; Balasubramanian, M.; Belke, D. D.; Makino, A; Chan, A.; Woods, V. L.; Dillmann, W. H.; Sharma, V. S.; Pilz, R. B.; Bigby, T. D.; Boss, G. R. *Exp. Biol. Med.* **2007**, 232, 1432.
26. Franz, K. J.; Doerr, L. H.; Spingler, B.; Lippard, S. J. *Inorg. Chem.* **2001**, 40, 3774.
27. Chiang, C.-Y.; Lee, J.; Dalrymple, C.; Sarahan, M. C.; Reibenspies, J. H.; Darensbourg, M. Y. *Inorg. Chem.* **2005**, 44, 9007.
28. Bertini, I.; Gray, H. B.; Stiefel, E. D.; Valentine, J. S., *Biological Inorganic Chemistry Structure and Reactivity*, **2007**, University Science Books, Sausalito, CA.
29. Addison, A. W.; Rao, T. N.; Reedijk, J.; Vanrijn, J.; Verschoor, G. C. *J. Chem. Soc., Dalton Trans.* **1984**, 1349.
30. Richter-Addo, G. B.; Hodge, S. J.; Yi, G. B.; Khan, M. A.; Ma, T. S.; VanCaemelbecke, E.; Guo, N.; Kadish, K. M. *Inorg. Chem.* **1996**, 35, 6530.
31. Zhu, X. Q.; Zhang, J. Y.; Mei, L. R.; Cheng, J. P. *Org. Lett.* **2006**, 8, 3065.

32. Sanders, B. C.; Dube, K. S.; Harrop, T. C. *unpublished results*.
33. Weber, J. H. *Inorg. Chem.* **1967**, 6, 258.
34. Gill, N. S.; Taylor, F. B. *Inorg. Synth.* **1967**, 9, 136.

Appendix

STRUCTURE AND PROPERTIES OF AN EIGHT-COORDINATE MN(II) COMPLEX THAT DEMONSTRATES A HIGH WATER RELAXIVITY¹

¹ Dube, K. S.; Harrop, T. C. *Dalton Trans.* **2011**, DOI: 10.1039/c1dt10579e

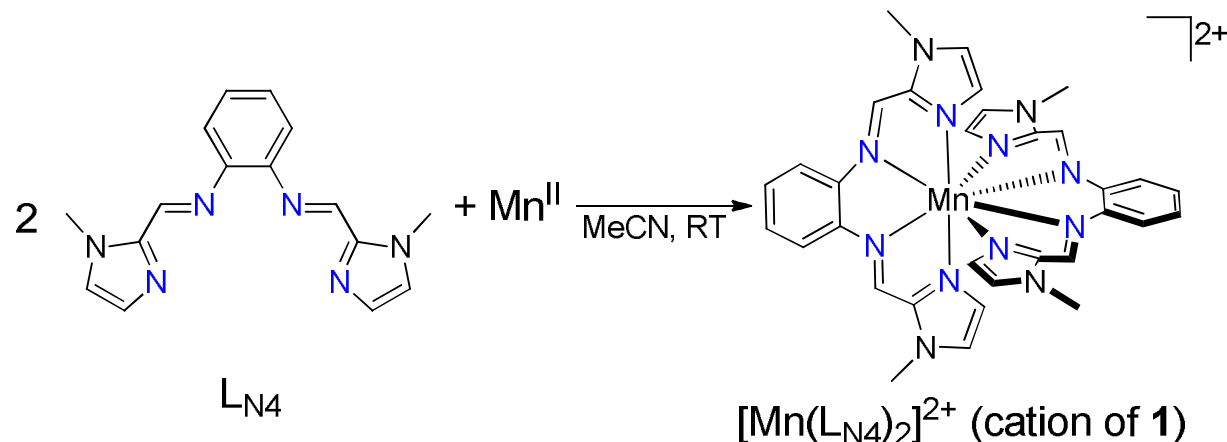
Reprinted here with permission from The Royal Society of Chemistry

An air-stable eight-coordinate (8C) Mn(II)N₈ complex has been synthesized utilizing an N₄ imidazole/imine ligand. The 8C dodecahedral geometry is structurally robust as the Mn complex is stable to air, NO(g), and potential coordinating anions. The structural, spectroscopic and water relaxivity properties of this complex are reported.

Transition-metal complexes with high coordination-numbers (CN > 6) are of interest due to their unique bonding properties, enhanced thermodynamic stability, and potential applications.¹ Specifically, interest in high CN Mn has been amplified due to Mn's central role in biology and catalysis.²⁻⁵ For example, multi-valent Mn participates in biological redox processes such as in photosystem II (PSII) where Mn(III/IV) ions comprise the oxygen evolving complex (OEC) converting water into O₂(g) with the aid of light.⁵ Mn complexes have also been used for biological imaging as magnetic resonance contrast (MRI)⁶ and fluorescence agents⁷ due to their favourable water-exchange rates, magnetic properties (nuclear spin, $I = 5/2$, $S = 5/2$ for high-spin Mn(II)), and low toxicity. For biological catalysis, the accessibility of the many redox couples of Mn and, for MRI, the low-energy barrier to exchange bulk water (expand/decrease the CN) at the Mn center is crucial. Indeed, a few potential MRI agents utilize the lack of ligand-field-stabilization-energy (LFSE) of high-spin (HS) d^5 Mn(II) to form high (e.g. 7-to-8) CN systems.^{3b} High denticity chelates are required to enhance the thermodynamic and kinetic stability of an otherwise labile metal center. Thus, a fundamental understanding and exploration of the chemistry and reactivity of high CN Mn is warranted due to these potential functions.

In light of the applications utilized for Mn, we have targeted the synthesis and characterization of eight-coordinate (8C) systems. This particular CN is rare for Mn(II) yet would presumably impart stability onto the substitutionally-labile Mn(II) center. For example, several high CN Mn-MRI^{3b} and Mn-SOD biomimetics⁸ have been constructed that are 7C with a

relatively smaller number of 8C. Importantly, 8C Mn(II) complexes with multidentate chelates are more desirable because of their enhanced stability in aqueous solution. Of the known 8C Mn(II) complexes, most contain MnO_8 (from weak donor ligands like crown ethers)² and MnO_xN_y (from a combination of salen/Schiff-base type and tight bite-angle NO_3^- ligands)³; relatively few have been reported with an MnN_8 coordination sphere.⁴ Of these reported 8C Mn(II) complexes, few report on their reactivity or potential applications. In this work we have utilized *bis*-coordination of the ligand, $\text{L}_{\text{N}4}$, previously published by our group⁹ that supports and induces specific and predictable 8C geometry around Mn(II) namely, $[\text{Mn}(\text{L}_{\text{N}4})_2](\text{ClO}_4)_2$ (**1**) (Scheme 3.1). The synthesis, structure, and spectroscopic/relaxivity properties of this 8C Mn(II) complex are described in the present communication.



Scheme 3.1. Synthesis of $[\text{Mn}(\text{L}_{\text{N}4})_2](\text{ClO}_4)_2$ (**1**).

Complex **1** was synthesized anaerobically by reaction of an MeCN solution of $\text{L}_{\text{N}4}$ with $[\text{Mn}(\text{H}_2\text{O})_6](\text{ClO}_4)_2$ (2:1 ratio) at room temperature (RT) in 82% yield as a pale-yellow air-stable solid. The synthesis of **1** was clean and no other Mn species were observed in the reaction. In fact, **1** forms regardless of the metal-to-ligand stoichiometry, which is unlike what happens in the coordination chemistry of $\text{L}_{\text{N}4}$ with Fe(II).⁹ The lack of 1:1 Mn: $\text{L}_{\text{N}4}$ complex formation suggests that 8C **1** is the thermodynamically-favored product. Additionally, potential anionic ligands like

NO_2^- , Cl^- or Br^- do not appreciably react with **1** further underscoring the stability of the 8CN. Even excess NO(g) purge displays no reactivity. The coordination mode of $\text{L}_{\text{N}4}$ is due to the tight bite of the di-imine portion ($\text{avg} = 41.31^\circ$) in combination with the ionic radius of 8C Mn(II) = 0.96 Å.¹⁰ In similarly disposed phen-type ligands, it has been proposed that metals with ionic radii close to 1.0 Å will favor long-range bonding with a predicted metal–N distance of ~ 2.5 Å.¹¹ This metric is due to the steric preference of five-member chelate rings for larger metal ions.¹² Additionally, the di-N backbone forms a rigid cleft in these ligands somewhat analogous to highly pre-organized ligands such as macrocycles and EDTA that display a size-based metal-ion selectivity.¹³ Thus, $\text{L}_{\text{N}4}$ should either coordinate as a *bis*-8C species or as a mono-ligand adduct with a highly distorted 4C geometry and additional monodentate ligands to complete the coordination sphere. Indeed, $\text{L}_{\text{N}4}$ wraps around Mn(II) such that the Mn–N_{imine} distances (~2.5 Å) are longer than the Mn–N_{imidazole} distances (~2.3 Å) thus exposing Mn to coordinate another $\text{L}_{\text{N}4}$ unit (*vide infra*). This property, along with the limited motion of the outer imidazoles in $\text{L}_{\text{N}4}$, forces coordination of all N-donors to Mn(II). It is expected that other 8C complexes with $\text{L}_{\text{N}4}$ can be systematically constructed based on this metric criterion alone.

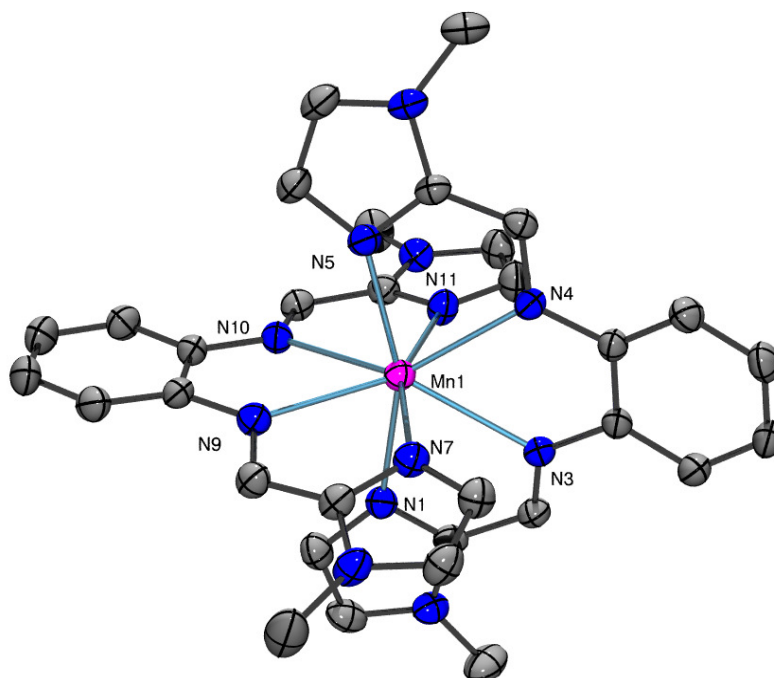


Fig. 3.1. ORTEP view of the cation of **1**. Ellipsoids are shown at 30% probability. H atoms omitted for clarity. Selected bond lengths [Å] and angles [deg]: Mn-N1, 2.319(3); Mn-N3, 2.521(3); Mn-N7, 2.333(3); Mn-N9, 2.482(3); N1-Mn-N3, 67.82(11); N3-Mn-N4, 63.69(10); N1-Mn-N5, 158.14(12); N7-Mn-N9, 68.76(11); N9-Mn-N10, 63.69(10); N7-Mn-N11, 158.08(12).

Single crystals of **1** were obtained aerobically from slow diffusion of Et₂O into an MeCN solution of **1** at −5 °C. The X-ray structure of **1** establishes the MnN₈ coordination sphere in the solid-state (Fig. 3.1) with metric parameters and crystal data described in the supporting information (SI†). Complex **1** is an example of a rare class of structurally-characterized 8C Mn(II) complexes that don't arise from the complexation of weakly-coordinating macrocyclic (i.e. crown ether) or tight bite-angle ligands like NO₃[−].^{2,3} The coordination geometry around the Mn(II) center is best described as a distorted dodecahedron with approximate *D*_{2d} point symmetry consistent with the parameters reported by Lippard^{1c} but unlike those observed in other MnN₈ systems.⁴ Indeed, **1** is the only example of an MnN₈ system with a dodecahedral coordination sphere. The set of two imidazole-N and two imine-N from each L_{N4} form two planar coordination units at Mn nearly perpendicular to each other with an interplanar angle of

87.09°, which collectively produce the 8C polyhedron (Fig. 1 and SI†). The average Mn–N_{imidazole} distances (2.316 Å) are shorter by 0.17 Å than the corresponding Mn–N_{imine} bonds (avg: 2.486 Å) as observed for the 8C Fe(II) complex, [Fe(L_{N4})₂](BF₄)₂.⁹ The Mn–N_{imine} bond lengths are in-line with reported 8C MnN₈ complexes like [Mn(tetrakis-pyrazol-tetraazacyclododecane)]²⁺ (avg. Mn–N: 2.419(8)Å) and [Mn(TPA)₂](ClO₄)₂ (avg. Mn–N: 2.497(4)Å).⁴ However, the Mn–N_{imidazole} bonds are considerably shorter and attest to the strength of this N-donor which presumably protects the Mn(II) center from other ligands. Of the known 8C Mn(II) structures, relatively few can be compared to **1** due to the arrangement and nature of the donating ligands to the central Mn(II) ion. Most reported 8C Mn(II) structures contain a mixture of O-/N-ligands³ or all O-donors.² Complex **1** thus adds to the relatively small list of 8C MnN₈ complexes.⁴

Complex **1** is soluble in polar solvents (MeCN, MeOH, DMF) with partial solubility in non-polar solutions (CH₂Cl₂) and pH 7 H₂O. As expected, the UV-vis is dominated by the ligand due to the lack of spin-allowed transitions for HS Mn(II). These bands are tentatively assigned as π - π^* transitions originating from the conjugated π -frame of L_{N4} and occur at 315 nm (ϵ = 45,000 M⁻¹ cm⁻¹) with a shoulder at 370 nm (ϵ = 21,000 M⁻¹ cm⁻¹) in MeCN at 298 K. The UV-vis of **1** is similar in all solvents (even H₂O) suggesting the 8CN is retained in a variety of dielectrics. Additionally, no oxidative degradation of **1** is observed in air. This observation is quite in contrast to the known oxidative degradation of Mn(II) complexes containing polyaza-type ligands,^{3b} which precludes their use as MRI agents. Cyclic voltammetry (CV) measurements attest to the stability provided to Mn(II) by L_{N4} as no oxidation wave is observed up to +1.00 V (vs. Fc/Fc⁺ in MeCN at RT). An irreversible reduction wave at –1.68 V is also observed. Thus, the N₈ coordination sphere does not appear to support the Mn(III) or Mn(I) states. The HS nature

of **1** in both the solid- and solution-states is evidenced by the value of μ_{eff} at 298 K: 5.76 BM in CD₃CN, 4.81 BM for solid. To describe the nature of this HS Mn(II) 8C complex, the X-band EPR spectrum was recorded at 10 and 70 K in an MeCN:toluene (1:1) glass (SI†). The EPR exhibits broad signals with strong features in the 2000 G region at different temperatures and powers. The broadness of the signals and lack of hyperfine has been observed in other high CN Mn(II) systems and has been attributed to dipole-dipole interactions and strong zero-field splitting (ZFS).¹⁴ To the best of our knowledge, EPR spectra of 8C Mn(II)N₈ are scarce with **1** being only the second such example.

In addition to understanding the structural/spectroscopic properties of these unusual molecular architectures, we envision **1** will be useful for catalytic or medical applications. Indeed, the bio-relevant chemistry of Mn complexes is due to their ability to act as MRI contrast agents⁶ or SOD biomimetics.⁸ In order to gauge the bio-compatibility of **1** for potential applications, we studied its aqueous stability via UV-vis spectroscopy. The UV-vis of **1** was monitored over 2 h at 298 K, at three pH values (pH = 6.2, 7.3, 9.0), with different non-coordinating buffers (MES, PIPES, CHES),¹⁵ and in potentially coordinating phosphate buffer (pH = 7.3).¹⁶ The UV-vis profiles reveal defined changes and near isosbestic behavior in the π - π^* bands of **1** over time (Fig. 3.2) consistent with conversion to a single species. For example (in all buffers), the band at 315 nm blue-shifts to 295 nm exhibiting an isosbestic point at 300 nm with steady decay of the shoulder at 370 nm (see Fig. 3.2 for PIPES). It was initially hypothesized that the spectra reveal ligand-decomplexation and formation of $[\text{Mn}(\text{OH}_2)_x(\text{OH})_y(\text{O})_z]^{n+/n-}$ type of species; however, the results are more indicative of a facile ligand-H₂O exchange process. For example, ESI-MS of the reaction products in PIPES indicated the presence of **1** (m/z = 319.6), mono-aquated **1**•H₂O (m/z = 328.6) and tris-aquated **1**•3H₂O

($m/z = 346.6$) with no trace of free Mn, ligand, or ligand hydrolysis products (Fig. S8, SI†). Additionally, extraction of compounds in the aqueous medium with CH_2Cl_2 revealed the predominant presence of 8C complex **1** by ESI-MS and UV-vis (see Fig. 3.2 and Fig. S9 in SI†). *The fact that **1** is seen in the ESI-MS after extraction signifies that this complex not only survives in water but can also be recovered via a reversible exchange process into an organic medium as an 8C complex without significant breakdown.* These results suggest that **1** affords a lower/similar coordinate $[\text{Mn}(\text{L}_{\text{N}4})_2(\text{OH}_2)_x]^{2+}$ in aqueous solution. No significant degradation or formation of oxo/hydroxo species was observed making it a feasible candidate for MRI (*vide infra*). We propose that this exchange possibly occurs by substitution of H_2O (up to four) for the weaker-bound Mn–N_{imine} ligands and retention of the N_{imidazole} donors while retaining the overall, albeit distorted, $[\text{Mn}(\text{L}_{\text{N}4})_2]^{2+}$ *bis*-coordination according to eq. 1:

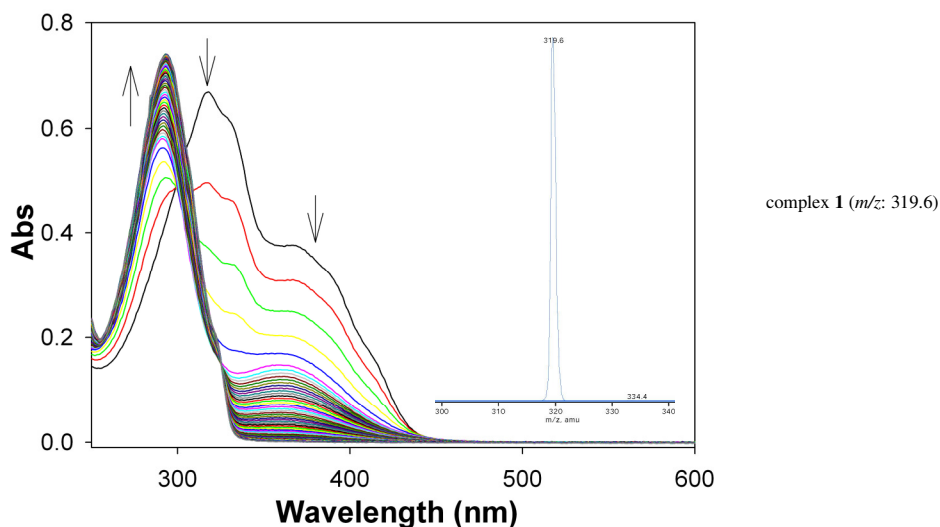


Fig. 3.2. UV-vis spectral monitoring of **1** (0.013 mM) in PIPES buffer (pH 7.3) under aerobic conditions at 298 K, arrows show direction of change (intervals are 2 min, total time: 120 min); inset shows the ESI-MS of the CH_2Cl_2 extract of this aqueous reaction, which match that of **1**.

Our preliminary aqueous studies indicate that **1** does potentially exchange with bulk H_2O

suggesting its possible use as an MRI agent. To investigate the possibility of **1** for MRI, we measured the ^1H relaxivity of **1** in a 5:1 $\text{CD}_3\text{OD}/\text{H}_2\text{O}$ solution at 60 MHz and 298 K. The mean relaxivity (R_1) of three runs was determined to be $4.14 \pm 0.10 \text{ mM}^{-1} \text{ s}^{-1}$. In contrast, the relaxivity of “free” Mn(II) in acidic conditions is $6.67 \text{ mM}^{-1} \text{ s}^{-1}$ (0.1 M HClO_4 , 310 K, 20 MHz).^{3b} The only other 8C Mn(II) with a reported relaxivity is $[\text{Mn}(\text{DOTAM})]^{2+}$ with a low R_1 of $0.96 \text{ mM}^{-1} \text{ s}^{-1}$ (H_2O , 310 K, 20 MHz) consistent with its coordinative saturation.^{3b} While outer-sphere relaxation mechanisms may contribute to the R_1 of **1**, the value is more like 6C Mn(II) and is indicative of a partial dissociative interchange mechanism for water exchange. The potential dissociation of the imine-N donors will result in up to four bound water molecules thus allowing **1** to have an R_1 value higher than predicted for an 8C complex. This mechanism of water exchange is further corroborated by the fact that there is no evidence for complete ligand dissociation from our aqueous solution studies (Fig. 3.2).

In summary, we report the synthesis, structure, and the unique spectroscopic/relaxivity properties of an 8C Mn(II) N_8 complex (**1**). Complex **1** is an example of a structurally-characterized 8C Mn(II) complex that retains its structural integrity even in the presence of $\text{O}_2(\text{g})$, $\text{NO}(\text{g})$ and potentially coordinating anions. In contrast to known 8C Mn(II) complexes, **1** is the first proposed to exchange with bulk H_2O and displays stability in aqueous solution. As a result, **1** exhibits a high relaxivity value ($R_1 = 4.14 \pm 0.10 \text{ mM}^{-1} \text{ s}^{-1}$) under pseudo-physiological conditions unusual for 8C but similar to 6C Mn(II) complexes that make it a promising contrast agent candidate. The detailed water-exchange pathways as well as synthetic modifications on the ligand periphery to enhance the water-solubility of these systems are continuing efforts in our laboratory.

Acknowledgements

T.C.H thanks the Department of Chemistry at the University of Georgia (UGA) for start-up funds and the UGA Research Foundation (UGARF) for a junior faculty grant.

Notes and references

Department of Chemistry, The University of Georgia, 1001 Cedar Street, Athens, GA, 30602, USA. Fax: +1-706-542-9454; Tel: +1-706-542-3486; E-mail: tharrop@uga.edu.

†Electronic Supplementary Information (ESI) available: Synthesis of **1**, key crystallographic data, and relaxivity measurements. For ESI and crystallographic data in CIF format see DOI: 10.1039/c1dt10579e

- 1 (a) N. Audebrand, E. Jeanneau, T. Bataille, S. Raite and D. Louër, *Solid State Sci.*, 2004, **6**, 579; (b) E. Jeanneau, N. Audebrand and D. Louër, *J. Mater. Chem.*, 2002, **12**, 2383; (c) S. J. Lippard, *Prog. Inorg. Chem.*, 1967, **8**, 109.
- 2 8C Mn complexes with Mn-O ligands: (a) H. O. N. Reid, I. A. Kahwa, A. J. P. White and D. J. Williams, *Inorg. Chem.*, 1998, **37**, 3868; (b) P. C. Junk, M. K. Smith and J. W. Steed, *Polyhedron*, 2001, **20**, 2979; (c) B. B. Hughes, R. C. Haltiwanger, C. G. Pierpont, M. Hampton and G. L. Blackmer, *Inorg. Chem.*, 1980, **19**, 1801; (d) Y. Rodríguez-Martín, C. Ruiz-Pérez, J. González-Platas, J. Sanchiz, F. Lloret and M. Julve, *Inorg. Chim. Acta*, 2001, **315**, 120.
- 3 8C Mn complexes with Mn-N/O ligands: (a) M. Louloudi, V. Nastopoulos, S. Gourbatsis, S. P. Perlepes and N. Hadjiliadis, *Inorg. Chem. Commun.*, 1999, **2**, 479; (b) S. Wang and T. D. Westmoreland, *Inorg. Chem.*, 2009, **48**, 719; (c) K. S. Hagen, *Angew. Chem., Int. Ed.*, 1992, **31**, 764.

- 4 8C Mn complexes with Mn-N ligands: (a) M. DiVaira, F. Mani and P. Stoppioni, *J. Chem. Soc., Dalton Trans.*, 1992, 1127; (b) Y. Gultneh, A. Farooq, K. D. Karlin, S. Liu and J. Zubieta, *Inorg. Chim. Acta*, 1993, **211**, 171; (c) X.-H. Bu, W. Chen, L.-J. Mu, Z.-H. Zhang, R.-H. Zhang and T. Clifford, *Polyhedron*, 2000, **19**, 2095; (d) H. Keypour, H. Goudarziafshar, A. K. Brisdon, R. G. Pritchard and M. Rezaeivala, *Inorg. Chim. Acta*, 2008, **361**, 1415. (e) D. Dang, Y. Bai and C. Duan, *J. Chem. Crystallogr.*, 2008, **38**, 557.
- 5 A. Sigel, H. Sigel, *Metal Ions in Biological Systems; Manganese and its Role in Biological Processes* 2000, 1-761.
- 6 (a) X.-A. Zhang, K. S. Lovejoy, A. Jasanoff and S. J. Lippard, *Proc. Natl. Acad. Sci. USA*, 2007, **104**, 10780; (b) R. B. Lauffer, *Chem. Rev.*, 1987, **87**, 901.
- 7 Y. You, E. Tomat, K. Hwang, T. Atanasijevic, W. Nam, A. P. Jasanoff and S. J. Lippard, *Chem. Commun.*, 2010, **46**, 4139.
- 8 D. P. Riley, *Chem. Rev.*, 1999, **99**, 2573.
- 9 A. K. Patra, K. S. Dube, G. C. Papaefthymiou, J. Conradie, A. Ghosh and T. C. Harrop, *Inorg. Chem.*, 2010, **49**, 2032.
- 10 R. D. Shannon, *Acta Crystallogr., Sect. A*, 1976, **32**, 751.
- 11 N. J. Williams, N. E. Dean, D. G. VanDerveer, R. C. Luckay and R. D. Hancock, *Inorg. Chem.*, 2009, **48**, 7853.
- 12 R. D. Hancock, *Acc. Chem. Res.* 1990, **23**, 253.
- 13 D. L. Melton, D. G. VanDerveer and R. D. Hancock, *Inorg. Chem.*, 2006, **45**, 9306.
- 14 W. Park, J. Cho, H. Lee, M. Park, M. S. Lah and D. Lim, *Polyhedron*, 2008, **27**, 2043.
- 15 J. S. Magyar and H. A. Godwin, *Anal. Biochem.*, 2003, **320**, 39.

16 There appears to be little affect on the rate of this transformation with respect to buffer as k_{obs} for pH 7.3 phosphate buffer was $6.54 \pm 0.28 \times 10^{-4} \text{ s}^{-1}$; pH 7.3 PIPES buffer, k_{obs} (fast): $2.06 \pm 0.02 \times 10^{-3} \text{ s}^{-1}$, k_{obs} (slow) = $6.89 \pm 1.03 \times 10^{-5} \text{ s}^{-1}$; pH 9.0 CHES, $k_{\text{obs}} = 2.58 \pm 0.55 \times 10^{-3} \text{ s}^{-1}$; pH 6.2 MES, k_{obs} (fast): $9.06 \pm 1.28 \times 10^{-3} \text{ s}^{-1}$, k_{obs} (slow): $2.91 \pm 0.07 \times 10^{-4} \text{ s}^{-1}$.

Experimental

General Information. All reagents were purchased from commercial suppliers and used as received unless otherwise noted. Acetonitrile (MeCN), methylene chloride (CH_2Cl_2), and diethyl ether (Et_2O) were purified by passing over activated alumina columns in an MBraun MB-SPS solvent purification system. Ethanol (EtOH) was purified by anaerobically distilling over $\text{Mg}(\text{OEt})_2$. Millipore water was obtained from a Barnstead Nanopure Infinity Ultrapure water system (resistivity at 298 K: $18.3 \text{ M}\Omega\cdot\text{cm}$; $0.2 \mu\text{m}$ filter assembly). The ligand, (N^1E, N^2E)- N^1, N^2 -bis((1-methyl-1H-imidazol-2-yl)methylene)benzene-1,2-diamine (L_{N4}), was prepared and checked according to the published procedure.¹ Unless specified, all reactions and spectroscopic studies were performed under an inert atmosphere of $\text{N}_2(\text{g})$ using standard Schlenk-line techniques or in an MBraun Labmaster glovebox under an atmosphere of purified N_2 .

Physical Methods. FTIR spectra were collected with a ThermoNicolet 6700 spectrophotometer running the OMNIC software program. All samples were run as solids either as a KBr pellet or on an ATR (attenuated total reflectance) diamond transmission window. X-band EPR was recorded on a Bruker ESP 300E EPR spectrophotometer controlled by a Bruker microwave bridge. The EPR was equipped with a continuous-flow liquid He cryostat and a temperature controller made by Oxford Instruments. Electronic absorption spectra were recorded at 298 K in the specified solvent on a Cary-50 UV-vis spectrometer with a Quantum Northwest TC 125 temperature controller. Solution pH readings were recorded with an Accumet Model 25 pH/ion meter with a mercury-free glass electrode, which was calibrated using the standard three buffer system (pH = 4, 7, and 10). Cyclic voltammetry (CV) measurements were performed with 2.7 mM analyte on a PAR Model 273A potentiostat using a Ag/Ag^+ reference electrode (0.01 M AgNO_3 in 0.1 M $n\text{BuN}_4\text{PF}_6$ in MeCN; $E_{1/2}$ (ferrocene/ferrocenium) = 0.09 V at RT), Pt-wire

counter electrode, and a Glassy Carbon working electrode (2 mm diameter). NMR spectra were recorded at 298 K on either a 400 MHz Bruker BZH 400/52 NMR spectrometer or on a Varian Unity Inova 500 MHz NMR spectrometer. Magnetic susceptibility measurements were performed in the solid-state using a Johnson-Matthey magnetic susceptibility balance and in the solution-state (CD_3CN) at 298 K using the Evans method on a Varian Unity Inova 500 MHz NMR spectrometer.² ESI-MS data were collected on a Perkin-Elmer Sciex API I Plus quadrupole mass spectrometer. Elemental analysis for C, H, and N was performed by QTI-Intertek using a Perkin-Elmer 2400 CHN analyzer.

[Synthesis of the Compounds]

Synthesis Safety Note: *Although no problems were observed in this work, perchlorate (ClO_4^-) salts of transition metals are potentially explosive and should be handled with care.*

$[\text{Mn}(\text{L}_{\text{N}4})_2](\text{ClO}_4)_2$ (1**).** To a dark orange solution of $\text{L}_{\text{N}4}$ (0.3685 g, 1.261 mmol) in 5 mL of MeCN was added a 5 mL MeCN solution of $[\text{Mn}(\text{H}_2\text{O})_6](\text{ClO}_4)_2$ (0.1601 g, 0.4424 mmol) at room temperature (RT). The resulting yellow colored solution was stirred for 4 h at RT after which the MeCN was reduced to 2 mL by rotary evaporation. Addition of ~5 mL of Et_2O to the above solution resulted in a yellow precipitate. This solid was filtered on a medium porosity sintered glass frit and washed with ~2 mL of Et_2O . Yellow crystals of complex **1** were formed by slow diffusion of Et_2O into a solution of **1** in MeCN at -5°C , 0.3033 g (0.3617 mmol, 82%). FTIR (ATR-diamond, solid-state) ν_{max} (cm^{-1}): 3118 (w), 1615 (m), 1581 (w), 1530 (w), 1484 (s), 1440 (s), 1414 (m), 1371 (w), 1325 (m), 1286 (m), 1227 (w), 1160 (w), 1074 (vs, ClO_4), 952 (s), 939 (s), 886 (s), 757 (s), 708 (w), 667 (m), 620 (s), 596 (m), 560 (w), 543 (w). UV-vis (MeCN, 298 K), λ_{max} , nm (ϵ , $\text{M}^{-1} \text{cm}^{-1}$): 315 (45,000), 368 (21,000). μ_{eff} : 4.81 BM (solid-state), 5.76 BM (solution-state in CD_3CN). LRMS-ESI (m/z): $[\text{M} - 2 \text{ClO}_4]^{2+}$ calcd for $\text{C}_{32}\text{H}_{32}\text{N}_{12}\text{Mn}$, 319.6;

found, 319.6. E_{red} (irreversible Mn^{III} , MeCN, RT, versus Fc/Fc^+): -1.68 V. Anal. Calcd for $\text{C}_{32}\text{H}_{32}\text{N}_{12}\text{Cl}_2\text{O}_8\text{Mn}\cdot\text{CH}_3\text{CN}$: C, 46.43; H, 4.01; N, 20.70. Found: C, 46.27; H, 3.68; N, 20.62.

Stability of $[\text{Mn}(\text{L}_{\text{N}4})_2](\text{ClO}_4)_2$ (1) in aqueous media. To test the stability of complex **1** in aqueous solution, we monitored the change in its UV-vis spectrum upon dissolution in different buffered solutions at 298 K under aerobic conditions. The complex was made as a stock solution in MeCN and an aliquot of this (50 μL) stock was added to a UV-vis cell containing 3 mL of the appropriate buffer. After addition, the UV-vis spectrum was recorded for 2 h at 1 min intervals (see Figs. 3.3-3.6). For all buffers tested, the intensity of $\lambda_{\text{max}} \sim 315$ nm gradually decreased with the appearance of an isosbestic point at ~ 300 nm and a new blue-shifted peak at ~ 290 nm. The lower intensity peak at 370 nm also decreased. After this initial decrease, the λ_{max} 290 nm increased slightly and appears to maximize with complete decrease of the λ_{max} 370 nm band. For CHES and phosphate buffer, the data were fit using the monophasic pseudo-first order rate equation: $y = A_0 + (A_\infty - A_0) * (1 - \exp(-kt))$, where A_∞ and A_0 are absorbance at time $t = \infty$ (i.e. when reaction is complete) and at $t = 0$ s, respectively, and y = absorbance at the specified wavelength. For MES and PIPES buffer, the data were fit using a two phase model: $y = A_0 + (A_\infty - A_0) * a(1 - \exp(-k_{\text{obs-fast}}t)) + b(1 - \exp(-k_{\text{obs-slow}}t))$ where $a = (A_\infty - A_0) * (\% \text{fast}) * 0.1$ and $b = (A_\infty - A_0) * (\% \text{slow}) * 0.1$. The average rate constants (k_{obs}) with their standard deviations were calculated from triplicate runs under identical experimental conditions.

The result of the aqueous reaction was verified by liquid-liquid extraction of the aqueous mixture with CH_2Cl_2 and characterization of the organic soluble fraction (sample procedure): After 2 h reaction in aqueous buffer (same time as the UV-vis studies), the yellow aqueous solution was transferred to a separatory funnel where it was extracted with 3×5 mL of CH_2Cl_2 . The yellow organic layer was then dried over anhydrous MgSO_4 , filtered, and roto-vapped to

afford a yellow residue. This material was subjected to LR-ESI-MS and UV-vis analysis, which revealed the presence of complex **1** (Fig. 3.11).

Stability of **1 in phosphate buffer (pH = 7.27).** A 5 mM stock solution of phosphate buffer (pH 7.27) was freshly prepared in millipore water and a 0.775 mM stock of complex **1** was prepared in MeCN. A 50 μ L aliquot of the complex **1** stock was then added to 3 mL of the phosphate buffer solution in a quartz UV-vis cuvette and the UV-vis was monitored for 2 h at 1 min intervals (see Fig. 3.3); $k_{\text{obs}} = 6.53 \pm 0.28 \times 10^{-4} \text{ s}^{-1}$ at 294 nm.

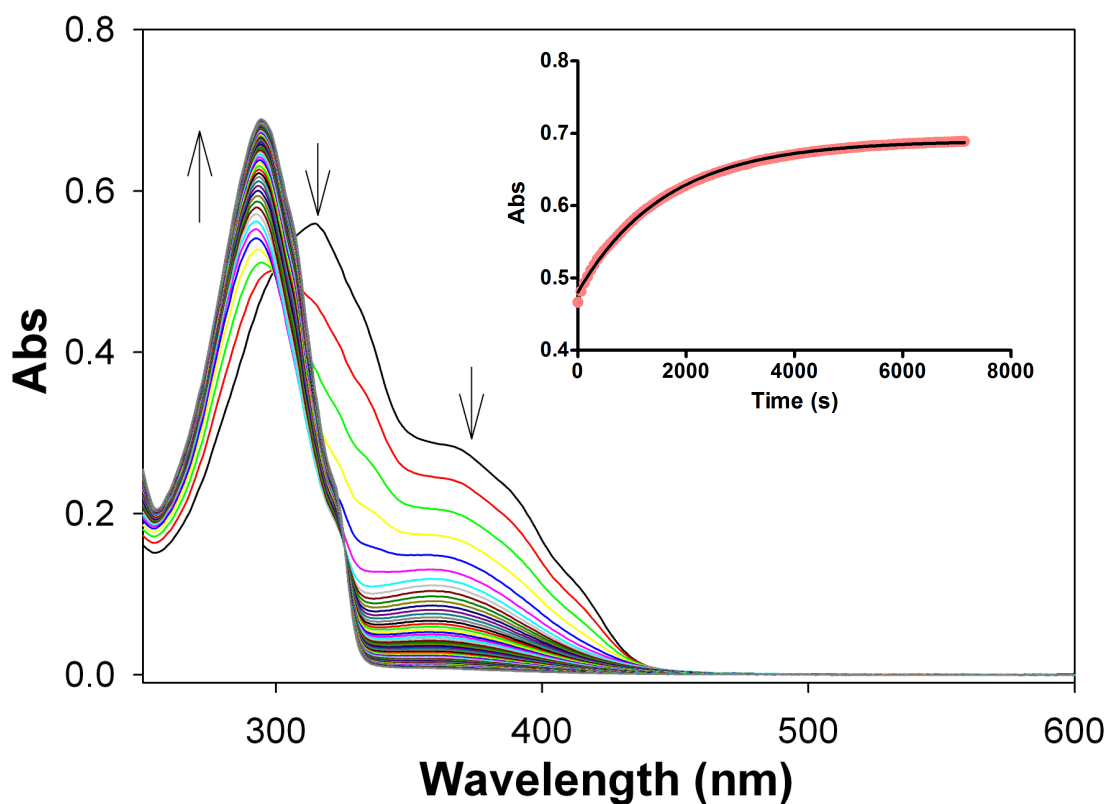


Fig. 3.3. UV-vis spectral monitoring of complex **1** (0.013 mM) in phosphate buffer (pH = 7.27) at 298 K with arrows showing direction of change (data collected at 1 min intervals but only every 2 min plot is displayed for clarity in the UV-vis, total time = 120 min); inset shows A_{294} vs. time plot that the kinetic parameters were derived from (data in red, fit = black line).

Stability of 1 in PIPES buffer (pH = 7.31). A 50 mM stock solution of PIPES buffer (pH = 7.31) was freshly prepared in millipore water and a stock of 0.800 mM complex **1** was prepared in MeCN. A 50 μ L aliquot of the complex **1** stock was then added to 3 mL of PIPES buffer in a quartz UV-vis cuvette and the UV-vis was monitored for 2 h at 1 min intervals (see Fig. 3.4); k_{obs} (fast) = $2.06 \pm 0.02 \times 10^{-3} \text{ s}^{-1}$, k_{obs} (slow) = $6.89 \pm 1.03 \times 10^{-5} \text{ s}^{-1}$ at 294 nm.

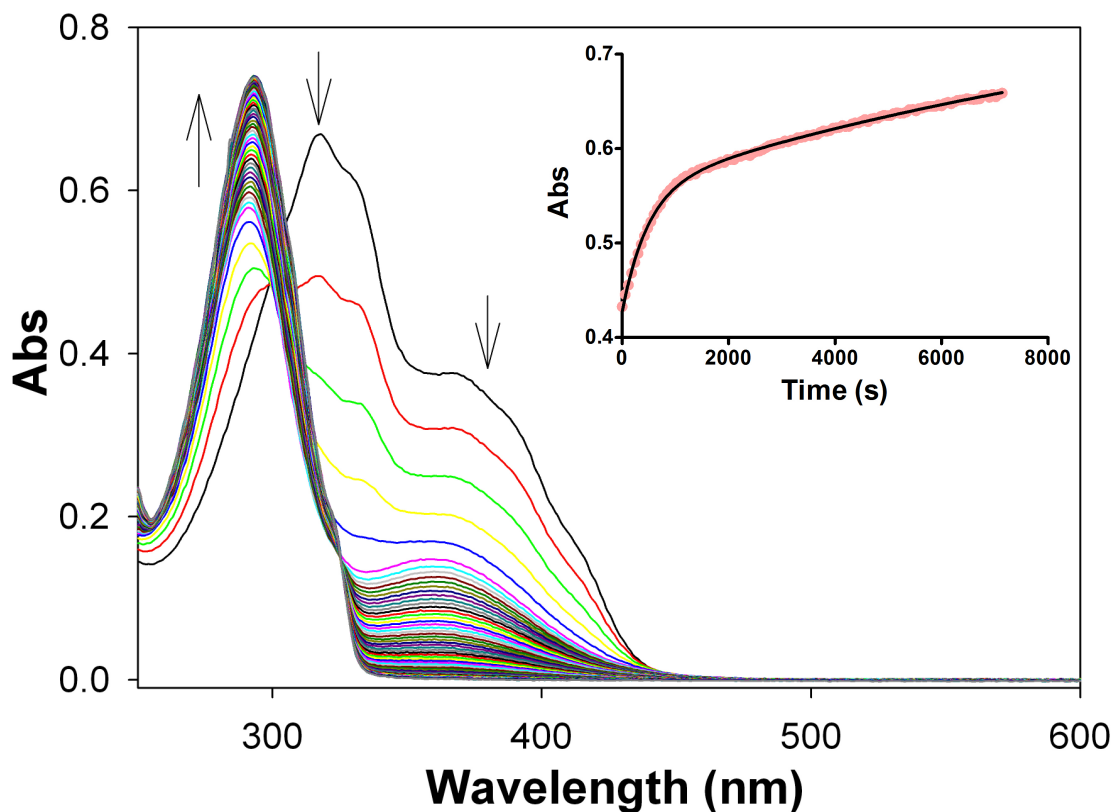


Fig. 3.4. UV-vis spectral monitoring of complex **1** (0.013 mM) in PIPES buffer (pH = 7.31) at 298 K with arrows showing direction of change (data collected at 1 min intervals but only every 2 min plot is displayed for clarity in the UV-vis, total time = 120 min); inset shows A_{294} vs. time plot that the kinetic parameters were derived from (data in red, fit = black line).

Stability of 1 in CHES buffer (pH = 9.04). A 50 mM stock solution of CHES buffer (pH = 9.04) was freshly prepared in millipore water and a stock of 0.800 mM complex **1** was prepared in MeCN. A 50 μ L aliquot of the complex **1** stock was then added to 3 mL of CHES buffer in a quartz UV-vis cuvette and the UV-vis was monitored for 2 h at 1 min intervals (see Fig. 3.5); $k_{\text{obs}} = 2.58 \pm 0.55 \times 10^{-3} \text{ s}^{-1}$ at 291 nm.

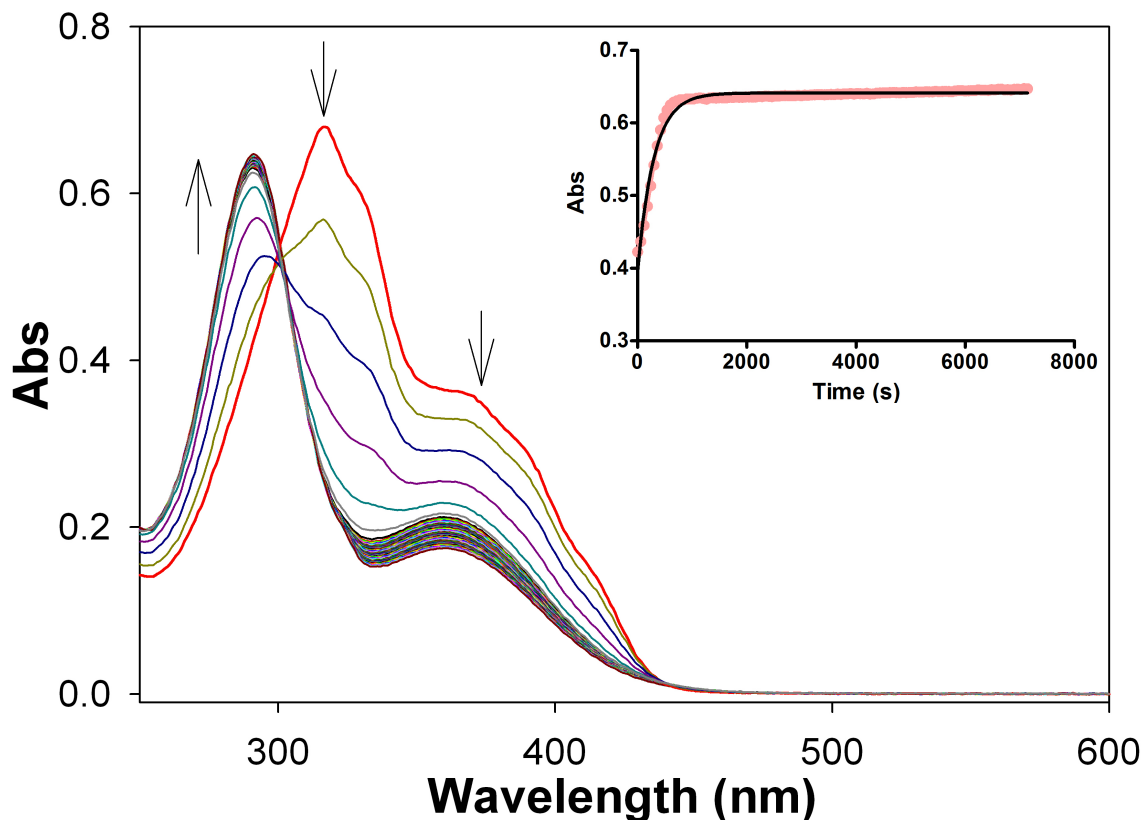


Fig 3.5. UV-vis spectral monitoring of complex **1** (0.013 mM) in CHES buffer (pH = 9.04) at 298 K with arrows showing direction of change (data collected at 1 min intervals but only every 2 min plot is displayed for clarity in the UV-vis, total time = 120 min); inset shows A_{291} vs. time plot that the kinetic parameters were derived from (data in red, fit = black line).

Stability of 1 in MES buffer (pH = 6.24). A 50 mM stock solution of MES buffer (pH = 6.24) was freshly prepared in millipore water and a stock of 0.800 mM complex **1** was prepared in MeCN. A 50 μ L aliquot of the complex **1** stock was then added to 3 mL of MES buffer in a quartz UV-vis cuvette and the UV-vis was monitored for 2 h at 1 min intervals (see Fig. 3.6); k_{obs} (fast): $9.06 \pm 1.28 \times 10^{-3} \text{ s}^{-1}$, k_{obs} (slow): $2.91 \pm 0.07 \times 10^{-4} \text{ s}^{-1}$ at 291 nm.

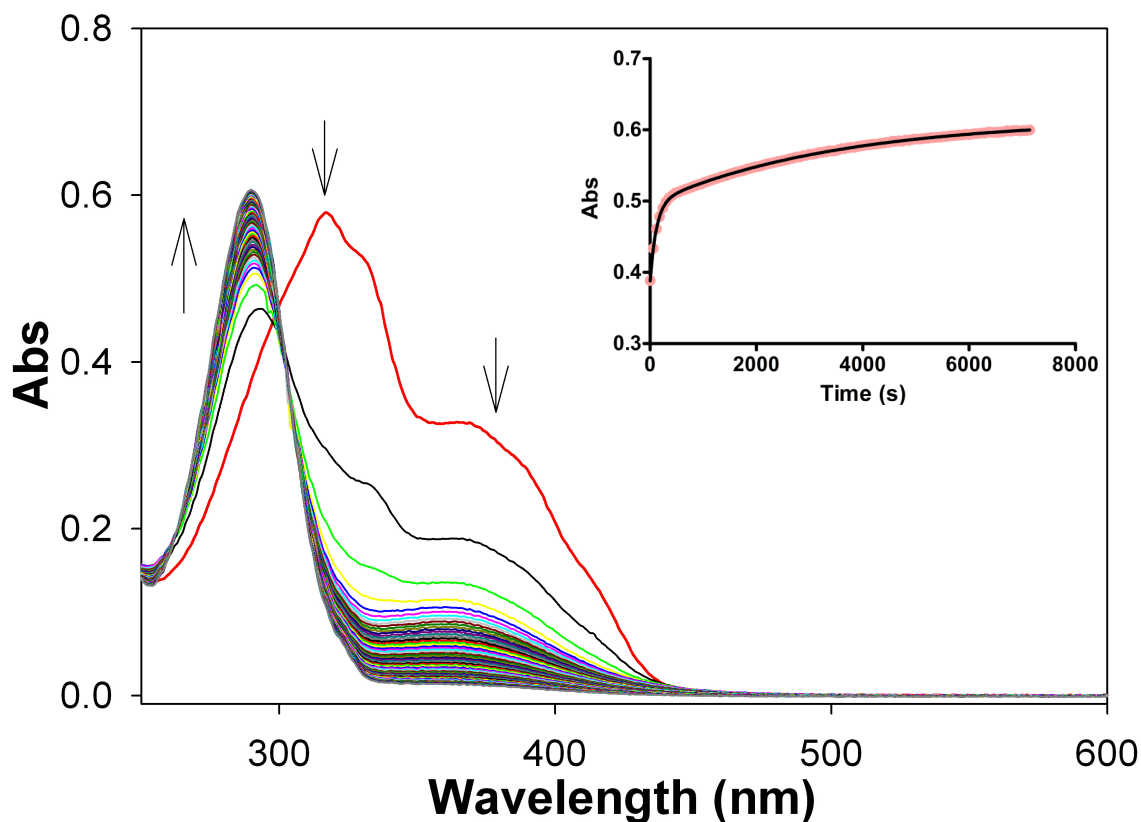


Fig. 3.6. UV-vis spectral monitoring of complex **1** (0.013 mM) in MES buffer (pH = 6.24) at 298 K with arrows showing direction of change (data collected at 1 min intervals but only every 2 min plot is displayed for clarity in the UV-vis, total time = 120 min); inset shows A_{291} vs. time plot that the kinetic parameters were derived from (data in red, fit = black line).

[Reactivity of Complex 1]

Reactivity of 1 with nitric oxide (NO). To an anaerobic MeCN solution (5 mL) of **1** (0.8478 g, 1.011 mmol) was purged NO(g) for 1 min and the solution was allowed to stir under an NO atmosphere. No visible color change was observed in the reaction flask over the next 30-45 min. The MeCN solvent was then removed by vacuum distillation and the yellow residue was stirred in Et₂O for 1 h. The yellow solid thus obtained was filtered, dried, and characterized. Spectroscopic measurements (LR-ESI-MS and FTIR) were identical to complex **1** indicating no reaction with NO(g).

Reactivity of 1 with sodium nitrite (NaNO₂). To a 1 mL MeCN solution containing **1** (0.0053, 0.0063 mmol) was added 0.0154 g (0.2232 mmol = 35 mol-equiv) of NaNO₂. The reaction slurry was stirred for 30 min at RT with no observable visible changes. After stirring the reaction mixture was filtered to remove unreacted NaNO₂ and the filtrate was subject to ESI-MS and UV-vis studies which revealed only complex **1**.

Reactivity of 1 with sodium chloride (NaCl). A similar procedure was used except reagents were 0.0059 g (0.0070 mmol) of **1** and 0.0154 g (0.2635 mmol = 38 mol-equiv) of NaCl. The reaction slurry was stirred for 30 min at RT with no observable visible changes. Reaction workup revealed only complex **1**.

Reactivity of 1 with tetraethylammonium chloride (Et₄NCl). To a 2 mL MeCN solution of **1** (0.011 mM) was added a 15 μ L aliquot of a 14.5 mM MeCN solution of Et₄NCl (final concentration = 0.107 mM). The reaction was monitored at 1 h intervals for 10 h by UV-vis. Small changes do occur in the UV-vis, however, the ESI-MS of this reaction mixture revealed only **1** with no other products consistent with probable counter-anion exchange from [Mn(L_{N4})₂](ClO₄)₂ to [Mn(L_{N4})₂]Cl₂.

Reactivity of **1 with tetramethylammonium bromide (Me₄NBr).** A similar procedure was used except solutions were 0.011 mM of **1** in MeCN and a 15 μ L aliquot of a 13.0 mM MeCN solution of Me₄NBr (final concentration = 0.095 mM). Similar small changes in the UV-vis were obtained with ESI-MS showing only **1** consistent with probable counter-anion exchange from [Mn(L_{N4})₂](ClO₄)₂ to [Mn(L_{N4})₂]Br₂.

X-ray crystallographic data collection, structure solution, and refinement. Pale-yellow colored crystals of [Mn(L_{N4})₂](ClO₄)₂•MeCN (**1**•MeCN) were grown under aerobic conditions by slow diffusion of Et₂O into solutions of **1** in MeCN at -5°C. A suitable crystal was mounted and sealed inside a glass capillary. All geometric and intensity data were measured at 293 K on a Bruker SMART APEX II CCD X-ray diffractometer system equipped with graphite monochromatic Mo K α radiation (λ = 0.71073 Å) with increasing ω (width 0.5° per frame) at a scan speed of 10 s/frame controlled by the SMART-APEX II software package.³ The intensity data were corrected for Lorentz-polarization effects and for absorption⁴ and integrated with the SAINT software package. Empirical absorption corrections were applied to structures using the SADABS program.⁵ The structures were solved by direct methods with refinement by full-matrix least-squares based on F² using the SHELXTL-97 software⁶ incorporated in the SHELXTL 6.1 software package.⁷ The hydrogen atoms were fixed in their calculated positions and refined using a riding model. All non-hydrogen atoms were refined anisotropically. Selected crystal data for complex **1** is summarized in Table 3.1. Selected bond distances and angles for **1** are given in Table 3.2. Perspective views of the complexes were obtained using ORTEP.⁸

Table 3.1. Summary of crystal data and intensity collection and structure refinement parameters for [Mn(L_{N4})₂](ClO₄)₂•MeCN (**1**•MeCN).

Parameters	1 •MeCN
Formula	C ₃₄ H ₃₅ N ₁₃ O ₈ Cl ₂ Mn
Formula weight	879.59
Crystal system	Monoclinic
Space group	<i>P</i> 2 ₁ / <i>c</i>
Crystal color, habit	Yellow, rectangle
<i>a</i> , Å	10.3455(6)
<i>b</i> , Å	21.1221(12)
<i>c</i> , Å	18.0690(10)
α , deg	90.00
β , deg	92.6490(10)
γ , deg	90.00
<i>V</i> , Å ³	3944.2(4)
<i>Z</i>	4
ρ_{calcd} , g/cm ⁻³	1.481
<i>T</i> , K	293(2)
abs coeff, μ , mm ⁻¹	0.538
θ limits, deg	2.19-28.26
total no. of data	53897
no. of unique data	9736
no. of parameters	523
GOF on <i>F</i> ²	1.003
<i>R</i> ₁ , ^[a] %	6.47
<i>wR</i> ₂ , ^[b] %	16.70
max, min peaks, e/Å ³	0.721,-0.501

Table 3.2. Selected bond distances (Å) and bond angles (deg) for [Mn(L_{N4})₂](ClO₄)₂•MeCN (1•MeCN).

Mn(1)-N(1)	2.319(3)	N(3)-Mn(1)-N(9)	135.33(11)
Mn(1)-N(3)	2.521(3)	N(3)-Mn(1)-N(10)	134.00(11)
Mn(1)-N(4)	2.443(3)	N(3)-Mn(1)-N(11)	79.89(11)
Mn(1)-N(5)	2.300(3)	N(4)-Mn(1)-N(5)	69.99(11)
Mn(1)-N(7)	2.333(3)	N(4)-Mn(1)-N(7)	82.91(12)
Mn(1)-N(9)	2.482(3)	N(4)-Mn(1)-N(9)	137.42(11)
Mn(1)-N(10)	2.496(3)	N(4)-Mn(1)-N(10)	137.88(11)
Mn(1)-N(11)	2.310(3)	N(4)-Mn(1)-N(11)	81.21(11)
N(1)-Mn(1)-N(3)	67.82(11)	N(5)-Mn(1)-N(7)	100.70(12)
N(1)-Mn(1)-N(4)	131.50(11)	N(5)-Mn(1)-N(9)	84.38(12)
N(1)-Mn(1)-N(5)	158.14(12)	N(5)-Mn(1)-N(10)	79.64(12)
N(1)-Mn(1)-N(7)	87.72(12)	N(5)-Mn(1)-N(11)	87.94(12)
N(1)-Mn(1)-N(9)	79.92(11)	N(7)-Mn(1)-N(9)	68.76(11)
N(1)-Mn(1)-N(10)	79.80(11)	N(7)-Mn(1)-N(10)	132.21(11)
N(1)-Mn(1)-N(11)	91.56(12)	N(7)-Mn(1)-N(11)	158.08(12)
N(3)-Mn(1)-N(4)	63.69(10)	N(9)-Mn(1)-N(10)	63.69(10)
N(3)-Mn(1)-N(5)	133.32(11)	N(9)-Mn(1)-N(11)	132.62(11)
N(3)-Mn(1)-N(7)	79.57(11)	N(10)-Mn(1)-N(11)	68.93(11)

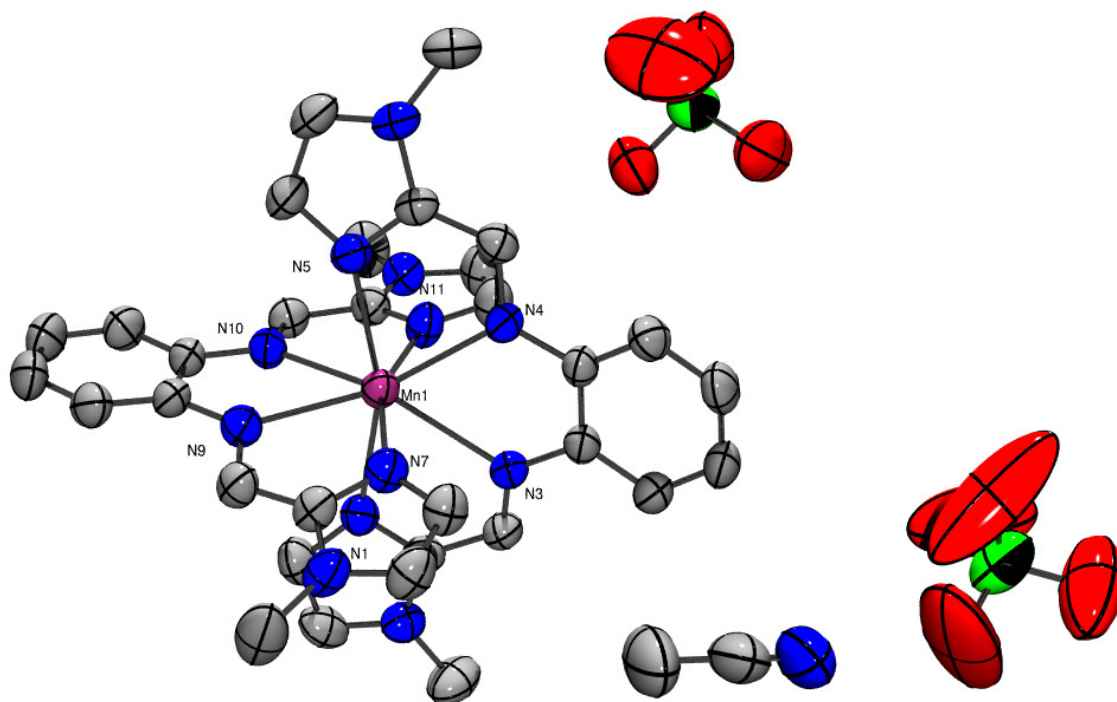


Fig. 3.7. ORTEP diagram of $[\text{Mn}(\text{L}_{\text{N}4})_2](\text{ClO}_4)_2 \cdot \text{MeCN}$ (**1**·MeCN) at 50% thermal probability. H atoms have been omitted for clarity. Sphere color code: grey: C; red: O; blue: N; green: Cl; magenta: Mn.

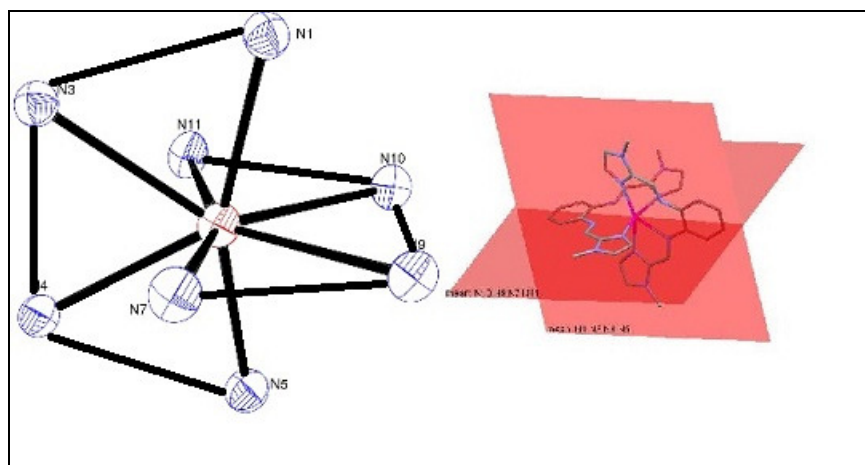


Fig. 3.8 (Left) A simplified view showing the coordination trapezoids (as defined by Lippard)⁹ of the coordination sphere around Mn(II) in **1**; (Right) The two intersecting planes of the $\text{L}_{\text{N}4}$ ligand in **1**; angle made by the two planes is 87.09° .

Relaxivity Measurements: The relaxivity measurements were carried out on a 60 MHz Varian EM360L-NMR spectrometer in a 5:1 $\text{CD}_3\text{OD}/\text{H}_2\text{O}$ solvent mixture at 298 K using the standard

saturation recovery pulse sequence (90° - τ - 90°) where τ is the variable delay time. Each set of readings was taken 1 min after addition of complex **1** to the NMR tube. The data points were based on a predefined array of variable time delay intervals. The data was fit to 'T1 Inversion Recovery fitting three parameters' (T13IR).¹⁰ The equation for the fit is:

$$y = A * \{1 - [1 + W * (1 - \exp(-K/T))] * \exp(-x/T)\} \quad (\text{Eq.1})$$

where

T = T_1 relaxation time

A = H_2O peak integral at time $x \gg T$

K = total time between scans in the 180- τ -90 sequence (equal to the acquisition time plus the relaxation delay time)

x = relaxation delay time t in the 180- τ -90 pulse sequence

W = $-(\text{integral at time } x = 0/A)$; (W = percent inversion)

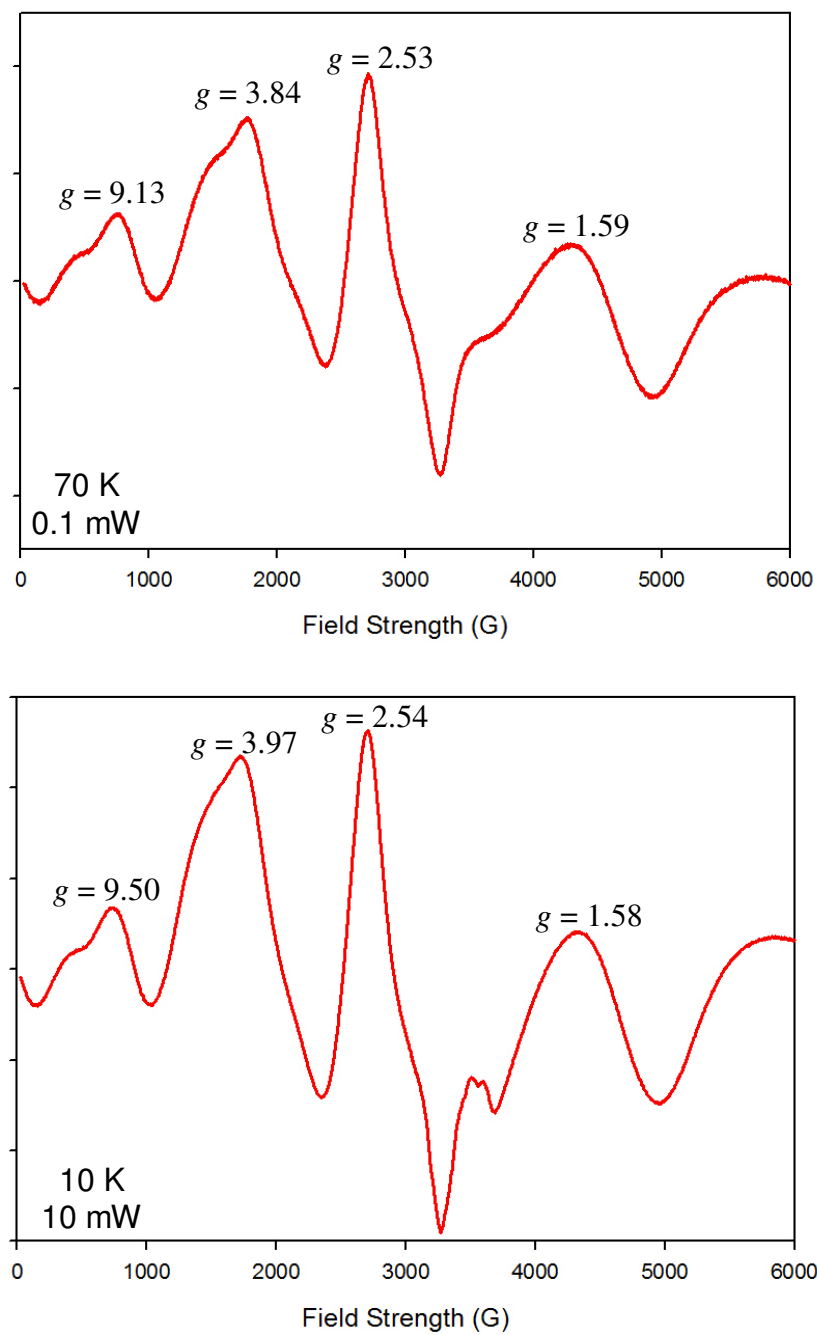


Fig. 3.9. X-band EPR spectrum of $[\text{Mn}(\text{L}_{\text{N}4})_2](\text{ClO}_4)_2$ (**1**) in a 1:1 MeCN:toluene glass at 70 K and 0.1 mW microwave power (top) and 10 K and 10 mW power (bottom). Microwave frequency = 9.6 GHz; modulation amplitude = 6.48 G. Selected g -values are displayed.

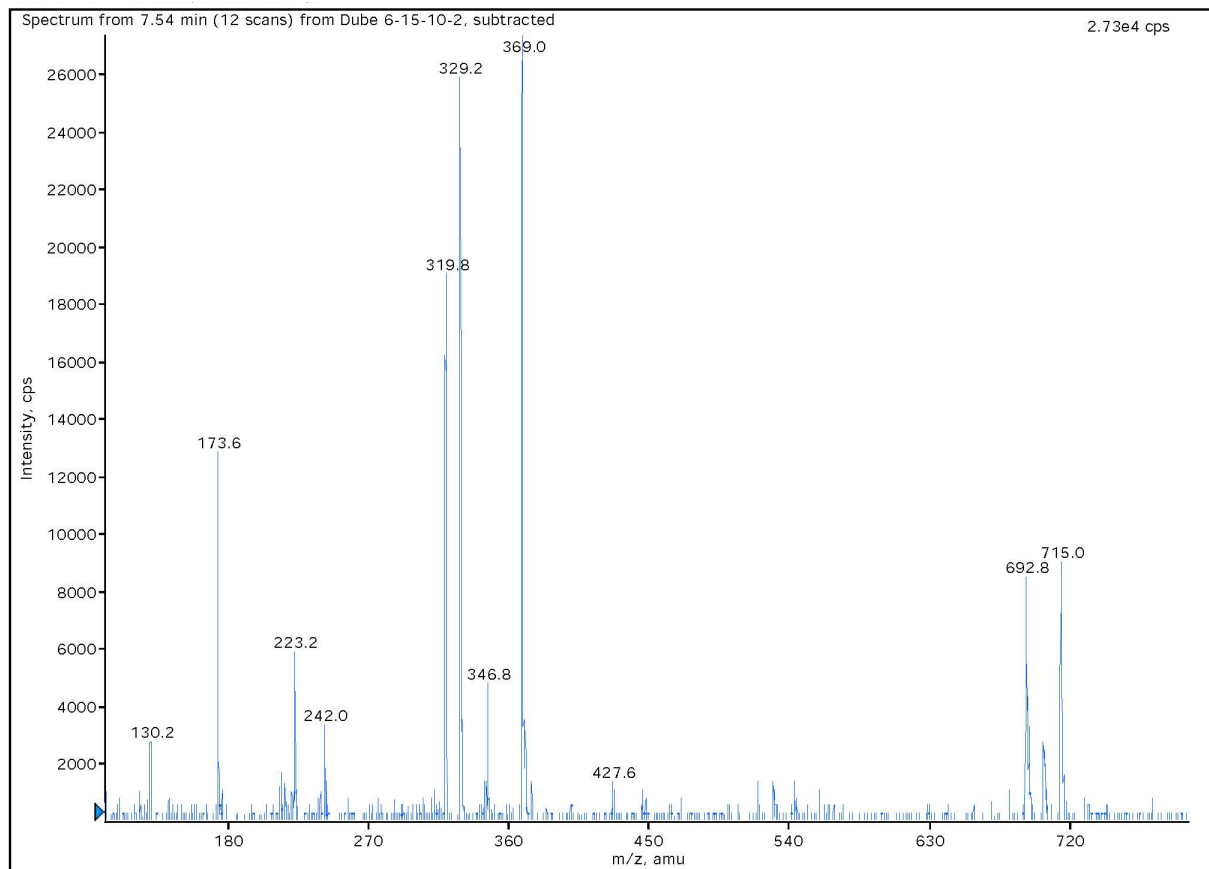


Fig. 3.10. Low-resolution ESI-MS of a 0.133 mM solution of $[\text{Mn}(\text{L}_{\text{N}4})_2](\text{ClO}_4)_2$ (**1**) in positive ion mode in pH 7.28 PIPES buffer after 2 h (solution from UV-vis studies). The m/z peak at 319.8 is consistent with $[\text{Mn}(\text{L}_{\text{N}4})_2]^{2+}$ (dication of **1**; calc m/z = 319.6); m/z peaks at 346.8 and 329.2 are consistent with aquated versions of **1**, namely $\{[\text{Mn}(\text{L}_{\text{N}4})_2] \cdot 3\text{H}_2\text{O}\}^{2+}$ (dication of **1**• $3\text{H}_2\text{O}$; calc. m/z = 346.6) and $\{[\text{Mn}(\text{L}_{\text{N}4})_2] \cdot \text{H}_2\text{O}\}^{2+}$ (dication of **1**• H_2O ; calc. m/z = 328.6). The peak with m/z of 173.6 is consistent with the dication of $[\text{Mn}(\text{L}_{\text{N}4})]^{2+}$ (calc m/z = 173.6) via fragmentation of the parent ion **1**. There is no evidence for dissociated ligand (m/z = 293.2 for $\text{L}_{\text{N}4} + \text{H}$) or other ligand fragments in this spectrum. Other peaks have not been assigned, but can be attributed to the complexity of the reaction medium, which is buffered water.

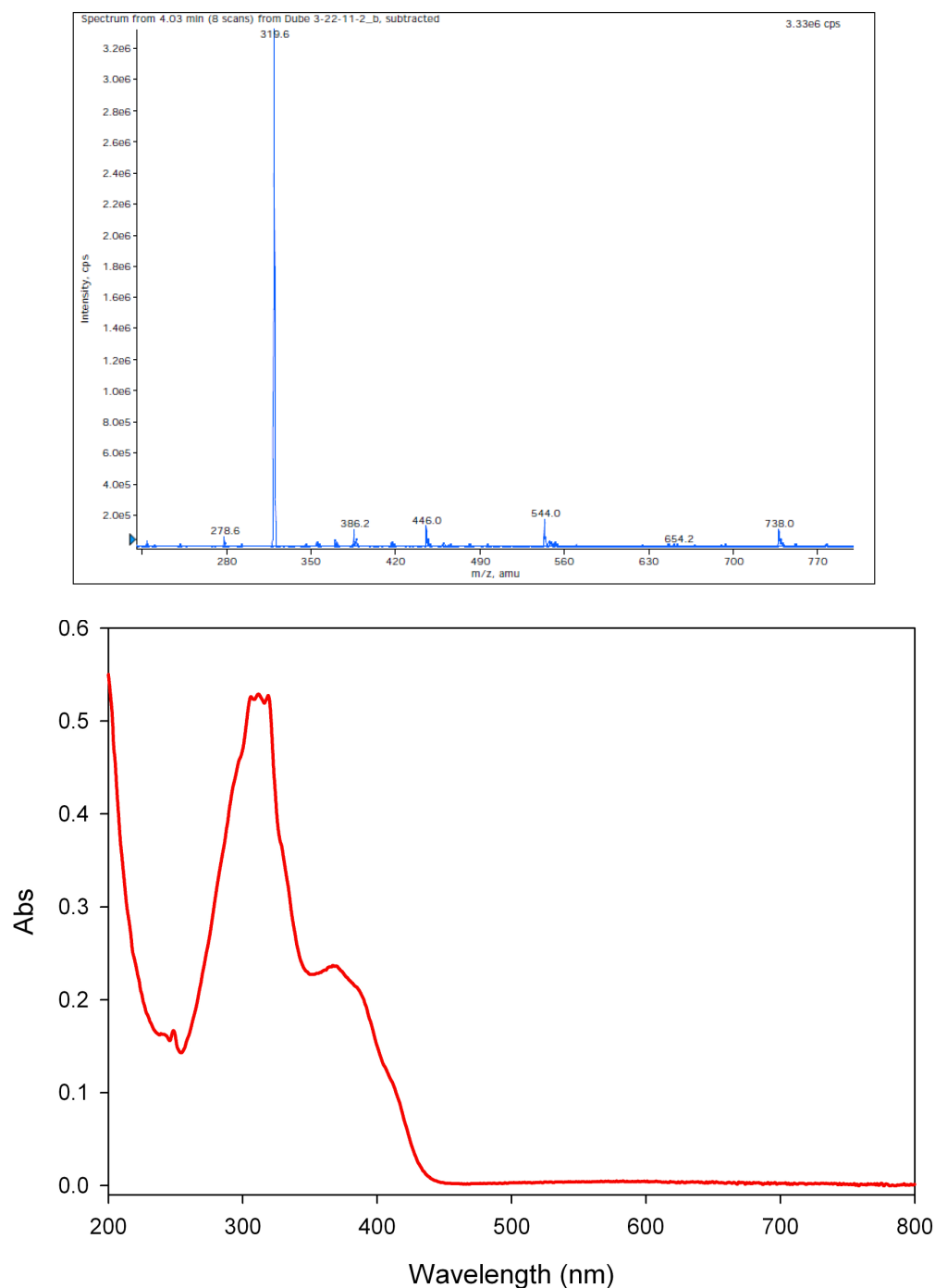


Fig. 3.11. (Top) Low-resolution ESI-MS(+) of the CH_2Cl_2 extract (see experimental for workup details) from a 0.133 mM solution of $[\text{Mn}(\text{L}_{\text{N}4})_2](\text{ClO}_4)_2$ (**1**) in pH 7.28 PIPES buffer after 2 h. The m/z peak at 319.6 is consistent with $[\text{Mn}(\text{L}_{\text{N}4})_2]^{2+}$ (dication of **1**; calc m/z = 319.6). (Bottom) qualitative UV-vis spectrum of the CH_2Cl_2 extract in MeCN at 298 K, which resembles the UV-vis of **1**.

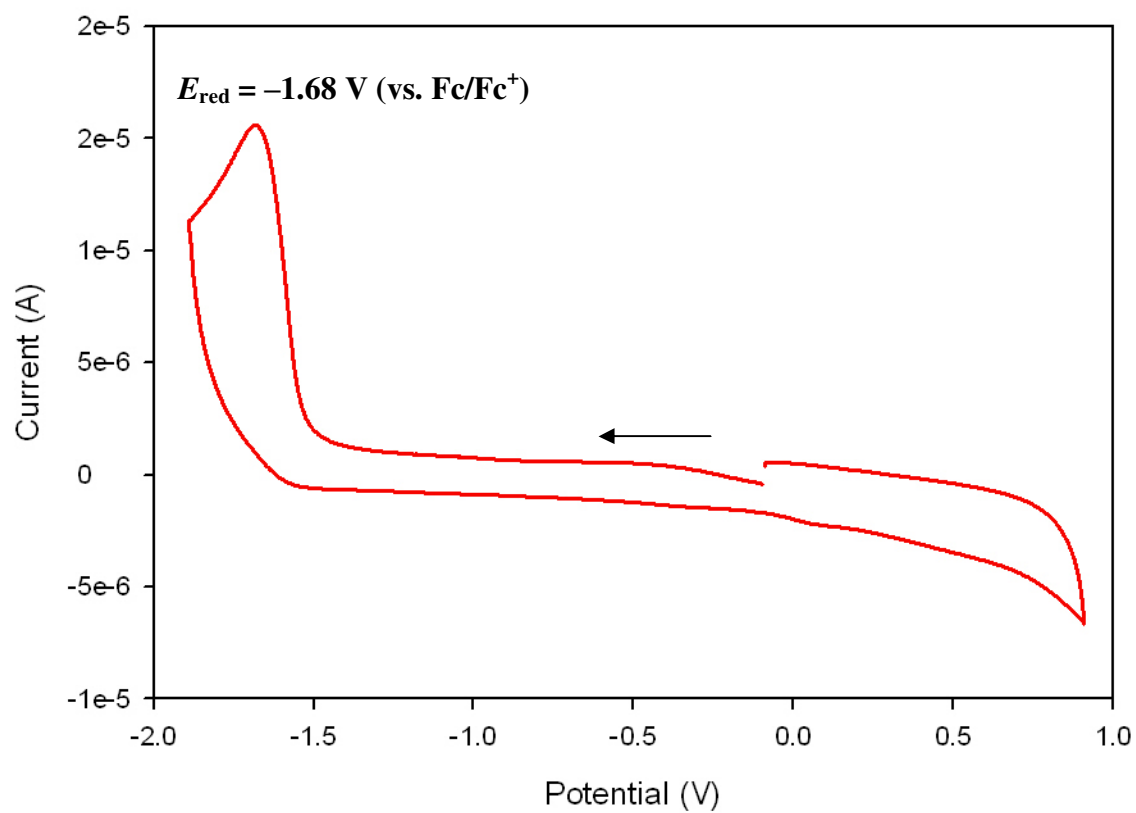


Fig. 3.12. Cyclic voltammogram of a 2.70 mM MeCN solution of $[\text{Mn}(\text{L}_{\text{N}4})_2](\text{ClO}_4)_2$ (**1**) (0.1 M $n\text{Bu}_4\text{NPF}_6$ supporting electrolyte, glassy carbon working electrode, Pt-wire counter electrode, RT, potential reported versus the ferrocene/ferrocenium couple). Arrow displays direction of scan.

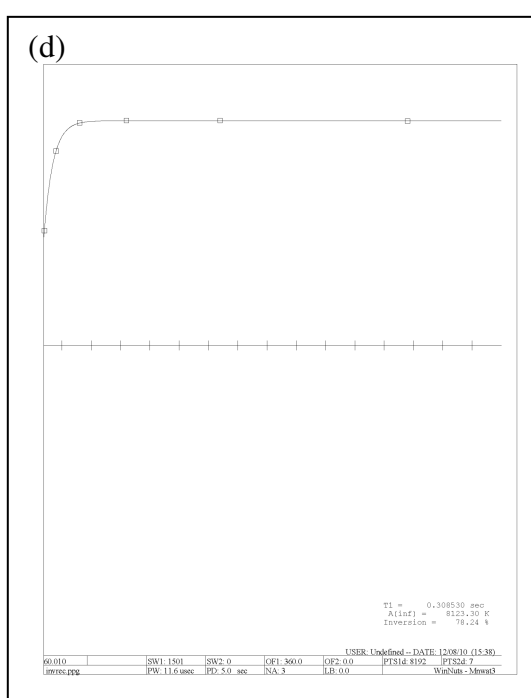
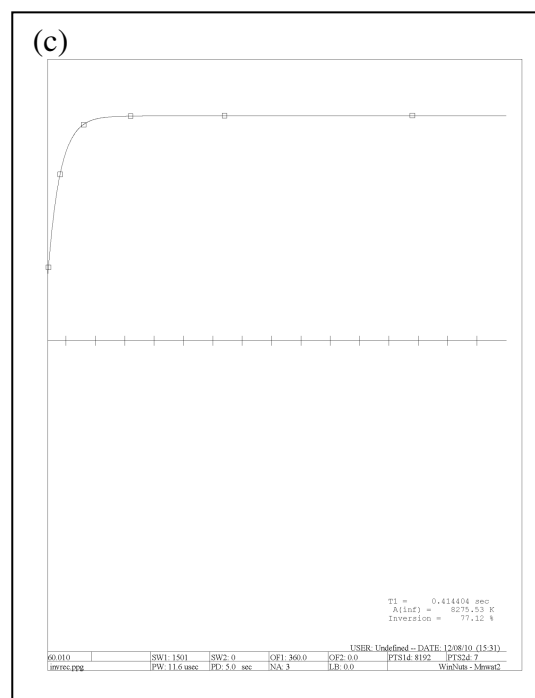
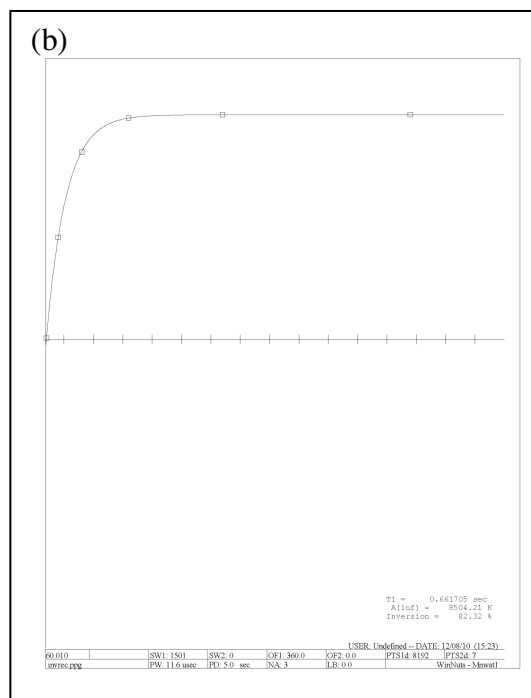
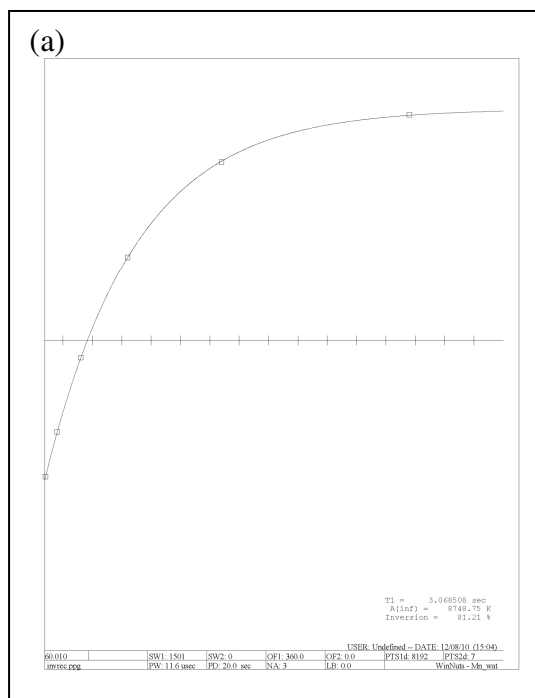


Fig. 3.13.(a-f). Representative plots for calculation of T1 relaxivity measurements for one sample run. The plots are ^1H signal integral of water versus time (s) fit according to Eq 1.

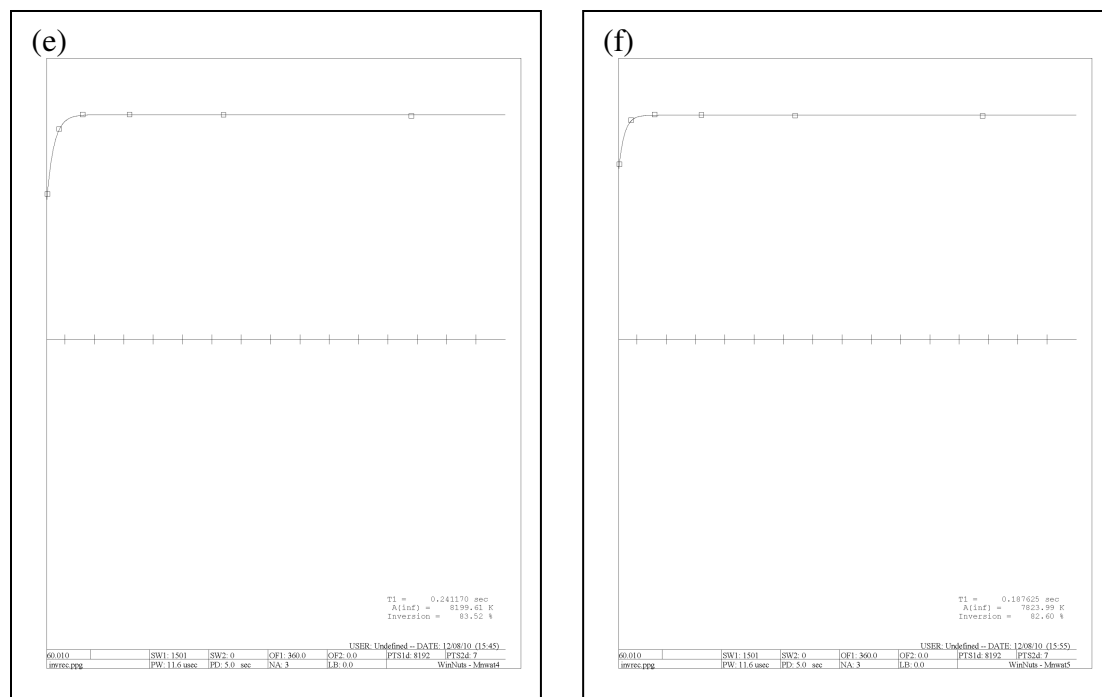


Fig. 3.13 (continued). Representative plots for calculation of T_1 relaxivity measurements for one sample run. The plots are ^1H signal integral of water versus time (s) fit according to Eq 1.

		$R = 3.9419$	
Plot	Conc. (mM)	$1/T_1$ (s^{-1})	T_1
(a)	0.0000	0.3259	3.0685
(b)	0.2607	1.5113	0.6617
(c)	0.5129	2.4131	0.4144
(d)	0.7572	3.2415	0.3085
(e)	0.9938	4.1465	0.2412
(f)	1.2231	5.3305	0.1876

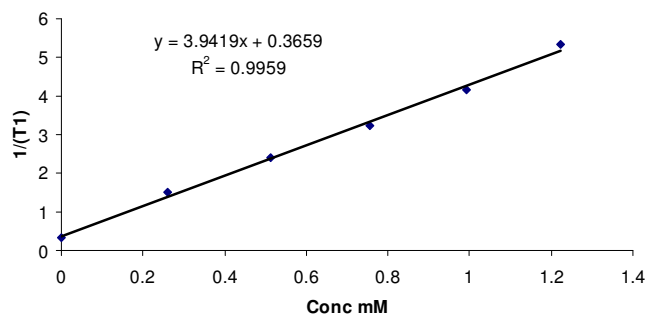


Fig. 3.14. Data and workup of one representative experiment to obtain the relaxivity (R_1) value for complex **1** ($\text{CD}_3\text{OD}/\text{H}_2\text{O}$ (5:1), 60 MHz, 298 K).

References

1. Patra, A. K.; Dube, K. S.; Papaefthymiou, G. C.; Conradie, J.; Ghosh, A.; Harrop, T. C. *Inorg. Chem.* **2010**, *49*, 2032.
2. Evans, D. F. *J. Chem. Soc.* **1959**, 2003. (b) Sur, S. K. *J. Magn. Resn.* **1989**, *82*, 169.
3. *SMART v5.626: Software for the CCD Detector System*; Bruker AXS: Madison, WI, 2000.
4. Walker, N.; Stuart, D. *Acta Crystallogr.* **1983**, *A39*, 158.
5. Sheldrick, G. M. SADABS, Area Detector Absorption Correction, University of Göttingen, Göttingen, Germany, **2001**.
6. Sheldrick, G. M. SHELX-97, Program for Refinement of Crystal Structures, University of Göttingen, Göttingen, Germany, **1997**.
7. Sheldrick, G. M. SHELXTL 6.1, Crystallographic Computing System, Siemens Analytical X-Ray Instruments, Madison, WI, **2000**.
8. Johnson, C. K. ORTEP-III, Report ORNL - 5138; Oak Ridge National Laboratory: Oak Ridge, TN, **1976**.
9. Lippard, S. J. *Prog. Inorg. Chem.* **1967**, *8*, 109.
10. (a) Levy, G. C.; Peat, I. R. *J. Magn. Reson.* **1975**, *18*, 500. (b) <http://www.acornnmr.com/NutsHelp/Relax.html>